# Remerciements

Je tiens avant tout à remercier le Professeur Jean-Paul Pirard de la confiance qu'il m'a témoignée, dès la fin de mes études d'ingénieur civil physicien en m'invitant à rejoindre l'équipe du Laboratoire de Génie Chimique. Je lui suis reconnaissant pour ses encouragements et pour son soutien. Qu'il ne doute pas non plus de ma reconnaissance pour nos nombreuses heures de discussion qui m'ont chaque fois permis de mieux préciser ma pensée, notamment lors de la rédaction de cette thèse.

Cette thèse ne serait pas ce qu'elle est sans le Docteur Silvia Blacher. En plus de ses innombrables conseils, c'est par son intermédiaire que j'ai pu rencontrer des spécialistes de techniques expérimentales en dehors du domaine traditionnel d'expertise du laboratoire de Génie Chimique, telles que la diffusion des rayons X aux petits angles (SAXS), les mesures de flexion à trois points pour la caractérisation des gels, et la tomographie électronique. Par ailleurs, sans nos incessantes discussions et sa grande disponibilité à m'aider à retravailler mes textes, je doute que le contenu de cette thèse ait jamais été fidèle à ma pensée. Qu'elle trouve ici l'expression de ma sincère reconnaissance.

Je remercie le Professeur Harry Reynaers et les Docteurs Bart Goderis et Monika Basiura de la Katholieke Universiteit Leuven pour m'avoir initié à la diffusion des rayons X aux petits angles, et pour m'avoir accueilli à de nombreuses reprises dans leur laboratoire. Que le Professeur Reynaers trouve également ici l'expression de ma profonde reconnaissance pour le soutien qu'il a apporté à plusieurs reprises à ma candidature auprès de différents organismes de financement de la recherche. Je suis aussi particulièrement reconnaissant au Docteur Goderis pour son aide indispensable lors de séances de mesures à l'European Synchrotron Radiation Facility à Grenoble (ESRF), pour les nombreux échanges que nous avons eus à propos des phénomènes de séparation de phase dans les systèmes polymériques, et pour le soin qu'il a pris à relire mes premiers écrits sur ce sujet. Certains passages de

cette thèse portent assurément sa marque, et je suis flatté qu'il ait accepté de faire partie du jury chargé d'examiner l'intégralité de ce travail.

J'adresse aussi mes plus vifs remerciements au Professeur George Scherer, de Princeton University, pour m'avoir accueilli pendant trois mois dans son laboratoire afin d'y effectuer des mesures de flexion sur les gels qui font l'objet de cette thèse. Je lui sais particulièrement gré d'avoir relu une partie du manuscrit, et de l'honneur qu'il me fait en acceptant d'examiner ce travail.

Je tiens à remercier le Professeur Krijn de Jong et le Docteur Ulrike Ziese, de Utrecht University, pour avoir observé certains de mes échantillons en tomographie électronique. Je les remercie également de m'avoir aidé à rédiger les parties du texte ayant rapport à cette technique expérimentale.

Je remercie aussi le Docteur Arnaud Rigacci, de l'École des Mines de Paris, pour avoir effectué le séchage supercritique de certains échantillons analysés dans ce travail.

À de nombreuses reprises, j'ai eu l'occasion de discuter avec le Professeur André Lecloux de l'Université de Liège, et avec le Docteur Jean-paul Schoebrechts du Laboratoire Central Solvay. Leurs conseils et leurs encouragements m'ont toujours été profitables, qu'ils en soient ici remerciés. Par ailleurs, je suis honoré que le Professeur Lecloux ait accepté de faire partie du jury chargé d'examiner cette thèse.

Les Professeurs Rudy Cloots, Michel Crine, Bernard Leyh et Guy L'Homme de l'Université de Liège, ainsi que le Docteur Mauritz Kelchtermans du Centre de Recherche d'Exxon-Mobil Chemical Europe me font l'honneur d'accepter d'examiner ce travail. Qu'ils trouvent ici l'expression de ma reconnaissance. Je suis en outre reconnaissant au Professeur L'Homme pour son soutien à ma candidature à une bourse d'Aspirant du Fonds National de la Recherche Scientifique.

Je remercie le Professeur Jean Phalippou de l'Université de Montpellier 2, et les Professeurs Jean-Pierre Gaspard et Pierre Marchot de l'Université de Liège, pour avoir appuyé ma candidature auprès de différentes institutions, et m'avoir donc permis de trouver un financement pour mener à bien ce travail.

Je tiens également à remercier Monsieur Francis Noville pour m'avoir initié au maniement de nombreux appareils de mesure, notamment les appareils d'adsorption d'azote et de porosimétrie au mercure. Je lui suis redevable, ainsi que tout le personnel du Laboratoire de Génie Chimique, du bon fonctionnement et de l'amélioration constante des appareils.

Je suis également reconnaissant aux Docteurs Wim Bras, Igor Dolbnya et Florian Meneau du Dutch-Flemish Beam Line (DUBBLE) à l'ESRF pour leur support technique lors des mesures de SAXS résolues en temps. Par la même occasion, je remercie les Docteurs Christelle Alié, Nathalie Job, Benoit Heinrichs, et René Pirard, de l'Université de Liège, ainsi que le Docteur Raluca Gearba, de l'Université Libre de Bruxelles, pour leur aide lors de séances de mesures intensives à l'ESRF.

Je remercie également Madame Martine Dejeneffe pour m'avoir initié à la microscopie électronique, et Madame Nicole Decloux pour le soin qu'elle a pris de l'imprégnation de mes échantillons.

Il m'est agréable de remercier quelques uns des membres et anciens membres du Département de Chimie Appliquée que je n'aurais pas encore cités, pour l'ambiance chaleureuse dans laquelle j'ai pu réaliser ce travail. Que Christophe Bossuot, Alain Brasseur, Maria-Rosa Bucci, Jean-Paul Dechamps, Sigrid Douven, Fabrice Ferauche, Fabian Gagliardo, Patrick Kreit, Stéphanie Lambert, Angélique Léonard, Sophie Pirard, François Pondant, Natalia Tcherkassova, Dominique Toye, Kim Yen Tran et Laurent Zorzi trouvent ici l'expression du plaisir que j'ai eu à les fréquenter ces dernières années.

Je tiens aussi à remercier le Fonds National de la Recherche Scientifique (FNRS) pour la bourse d'Aspirant dont il m'a fait bénéficier. Je remercie le FNRS, le Patrimoine de L'Université de Liège, ainsi que la Fondation Camille Héla de l'Université de Liège pour avoir contribué au financement de certains voyages que j'ai effectués. Je suis tout particulièrement reconnaissant au Fonds voor Wetenskappelijk Onderzoek Vlaanderen de m'avoir accordé le prix ExxonMobil Chemical Benelux 2004 qui a permis mon séjour à Princeton pendant l'été 2006.

Je remercie enfin René Gommes, mon père, du temps qu'il a consacré à la relecture du manuscrit, ainsi que pour l'intérêt qu'il a toujours manifesté à l'égard de mon travail.

# Abstract

The present work analyses the physicochemical phenomena responsible for the microstructure of Pd/$SiO_2$ xerogel catalysts and of metal-free hybrid $SiO_2$ xerogels synthesized by sol-gel process. The samples are synthesized by co-polymerizing tetraethoxysilane (TEOS) with 3-aminopropyltriethoxysilane or 3-(2-aminoethylamino)propyltrimethoxysilane in ethanol, the latter co-reactant possibly forming a complex with palladium. The analysis is conducted by following *in situ* the formation of the gels' nanostructure by Small-Angle X-ray Scattering (SAXS), by characterizing the microstructure of the final gels by beam-bending, and by analyzing the microstructure of the xerogels after desiccation, most notably by electron tomography.

The *in situ* SAXS analysis shows that the nanometer structure of the gels forms *via* a reaction-induced phase separation.

The microstructure of the hybrid xerogels is hierarchical, as assessed by electron microscopy, nitrogen adsorption and SAXS. Its structure is that of a microcellular foam at large scale, with pores a few hundred nanometers across, supported by elongated filaments, a few ten nanometers wide, each filament being made up by smaller structures, a few nanometers wide. The characteristics of the various structural levels depend on the nature and concentration of the co-reactant used. In the case of xerogel catalysts, electron tomography shows that Pd nanoparticles are regularly dispersed inside the silica, with distances between them comparable to the thickness of the skeleton.

On the basis of the time-resolved SAXS and of the characterization of the xerogels, it is argued that a double phase separation process is responsible for the structuring of the gels, with a primary phase separation leading to the microcellular foam morphology, and a secondary phase separation being responsible for the substructure of the filaments.

The large scale structure of the gels themselves, before desiccation, is analyzed by beam bending. This enables one to estimate the mechanical properties of the gels as well as the size of their largest pores. The microstructure of aerogels obtained by supercritical drying of the samples is also investigated. The comparison of the characterization data show that the nature and concentration of the co-reactant controls the amount of shrinkage that the gels undergo during desiccation, at the macroscopic scale as well as at the scale of the filaments.

# Contents

**1 The sol-gel process and the cogelation method 1**

1.1 Introduction . . . . . . . . . . 1

1.2 The sol-gel process . . . . . . . . . . 3

1.2.1 Gels and gelation . . . . . . . . . . 3

1.2.2 Drying of the gels . . . . . . . . . . 5

1.3 The cogelation method . . . . . . . . . . 7

1.3.1 Cogelled xerogel catalysts . . . . . . . . . . 7

1.3.2 Cogelled metal free xerogels . . . . . . . . . . 11

1.3.3 Farrago of observations about cogelled samples . . . . . . . . . . 13

1.4 Conclusion . . . . . . . . . . 14

**2 Electron tomography analysis of cogelled Pd/SiO$_2$ xerogel catalysts 16**

2.1 Introduction . . . . . . . . . . 16

2.2 Experimental Section . . . . . . . . . . 17

2.2.1 Preparation of the xerogel catalysts . . . . . . . . . . 17

2.2.2 Electron microscopy . . . . . . . . . . 18

2.2.3 Image Segmentation . . . . . . . . . . 20

2.3 Results . . . . . . . . . . 26

2.3.1 Qualitative results . . . . . . . . . . 26

2.3.2 Size distributions . . . . . . . . . . 29

2.3.3 Spatial distribution of the Pd particles . . . . . . . . . . 30

2.4 Discussion . . . . . . . . . . 34

2.5 Conclusion . . . . . . . . . . 36

3 *In situ* **SAXS analysis of the formation of cogelled Pd/SiO$_2$ gels** **37**
3.1 Introduction . . . . . . . . . . 37
3.2 Experimental section . . . . . . . . . . 38
  3.2.1 Synthesis of the samples and microscopy . . . . . . . . . . 38
  3.2.2 SAXS measurements . . . . . . . . . . 39
3.3 Results . . . . . . . . . . 40
  3.3.1 Time-resolved SAXS measurements of the gelling solutions . . . . . 40
  3.3.2 Photoreduction of Pd by X-rays . . . . . . . . . . 44
  3.3.3 SAXS comparison of Pd/SiO$_2$ gels and xerogels . . . . . . . . . . 44
3.4 Discussion . . . . . . . . . . 46
  3.4.1 General interpretation of the SAXS data . . . . . . . . . . 46
  3.4.2 Possibility of several mechanisms . . . . . . . . . . 49
  3.4.3 Phase separation model . . . . . . . . . . 51
3.5 Wet and dry samples . . . . . . . . . . 55
3.6 Conclusion . . . . . . . . . . 56

4 **Role of the co-reactant during the formation of cogelled silica gels, assessed by** *in situ* **SAXS** **57**
4.1 Introduction . . . . . . . . . . 57
4.2 Experimental section . . . . . . . . . . 58
  4.2.1 Synthesis of the samples . . . . . . . . . . 58
  4.2.2 Small Angle X-ray Scattering . . . . . . . . . . 60
4.3 Results . . . . . . . . . . 60
  4.3.1 Acid/Base gels . . . . . . . . . . 60
  4.3.2 EDAS and AES gels . . . . . . . . . . 65
4.4 Discussion . . . . . . . . . . 70
  4.4.1 Pure silica Acid/Base samples . . . . . . . . . . 70
  4.4.2 EDAS and AES samples . . . . . . . . . . 71
  4.4.3 Impact of microsyneresis on the total scattered intensity . . . . . . 73
  4.4.4 AES and EDAS gels . . . . . . . . . . 77
4.5 Conclusion . . . . . . . . . . 78

5 The structure of AES and EDAS xerogels in the light of phase separation 80

5.1 Introduction . . . . . . . . . . . . . . . . . . . . . . . . . . . . . . . . . . . 80
5.2 Experimental section . . . . . . . . . . . . . . . . . . . . . . . . . . . . . . 81
5.2.1 Synthesis of the samples . . . . . . . . . . . . . . . . . . . . . . . . 81
5.2.2 Physical characterization of the samples . . . . . . . . . . . . . . . 81
5.2.3 Microscopy and image analysis . . . . . . . . . . . . . . . . . . . . 83
5.3 Results . . . . . . . . . . . . . . . . . . . . . . . . . . . . . . . . . . . . . . 83
5.3.1 TEM and image analysis . . . . . . . . . . . . . . . . . . . . . . . . 83
5.3.2 Pycnometry and nitrogen adsorption . . . . . . . . . . . . . . . . . 86
5.3.3 Small Angle X-ray Scattering . . . . . . . . . . . . . . . . . . . . . 90
5.4 Discussion . . . . . . . . . . . . . . . . . . . . . . . . . . . . . . . . . . . . 92
5.4.1 Local and global evidence for the hierarchical structure of the xerogels 92
5.4.2 Remnants of the phase separation in the xerogels . . . . . . . . . . 94
5.5 Wet and dry samples . . . . . . . . . . . . . . . . . . . . . . . . . . . . . . 98
5.6 Conclusion . . . . . . . . . . . . . . . . . . . . . . . . . . . . . . . . . . . . 100

6 Porosity of the gels, aerogels and xerogels, by beam-bending and textural characterisations 101
6.1 Introduction . . . . . . . . . . . . . . . . . . . . . . . . . . . . . . . . . . . 101
6.2 Materials and method . . . . . . . . . . . . . . . . . . . . . . . . . . . . . 102
6.2.1 Synthesis and moulding of the gels . . . . . . . . . . . . . . . . . . 102
6.2.2 Bending measurements . . . . . . . . . . . . . . . . . . . . . . . . . 102
6.2.3 Drying of the gels and characterization of the xerogels and aerogels 103
6.3 Results . . . . . . . . . . . . . . . . . . . . . . . . . . . . . . . . . . . . . . 104
6.3.1 Beam bending results . . . . . . . . . . . . . . . . . . . . . . . . . . 104
6.3.2 Textural characterization of the aerogels . . . . . . . . . . . . . . . 112
6.4 Discussion . . . . . . . . . . . . . . . . . . . . . . . . . . . . . . . . . . . . 121
6.4.1 General observations about the mechanical properties of the gels . . 121
6.4.2 Macroscopic shrinkage during the drying of the gels . . . . . . . . . 122
6.4.3 Effect of drying on the gels' nanostructure . . . . . . . . . . . . . . 126
6.5 Conclusion . . . . . . . . . . . . . . . . . . . . . . . . . . . . . . . . . . . . 127

**7 General findings of the thesis** **129**

7.1 Introduction . . . . . . . . . . . . . . . . . . . . . . . . . . . . . . . 129

7.2 Microstructure of the gels . . . . . . . . . . . . . . . . . . . . . . . . 131

7.3 Mechanism of gel formation . . . . . . . . . . . . . . . . . . . . . . . 135

7.4 Samples with metal . . . . . . . . . . . . . . . . . . . . . . . . . . . . 137

7.5 Conclusion . . . . . . . . . . . . . . . . . . . . . . . . . . . . . . . . 138

**A Opening Granulometry** **139**

**B Fitting procedure of the beam bending relaxation data** **143**

**Bibliography** **161**

# Chapter 1

# The sol-gel process and the cogelation method

## 1.1 Introduction

The sol-gel process is a versatile way to synthesize porous and generally nanostructured materials [Brinker & Scherer 1990] that find a broad range of applications in various domains [Klein 1988]. They include precursors for the low temperature synthesis of glasses, adsorbent materials for chromatography columns, thermally insulating transparent materials, and many other applications related to their high porosity [Hrubesh 1998; Schmidt & Schwertfeger 1998; Siouffi 2003], and most notably catalysis [Gonzalez *et al.* 1997; Lecloux & Pirard 1998; Toebes *et al.* 2001].

The sol-gel process consists in the polymerization of precursor molecules in a solvent until the system gelifies; the liquid phase of the gel is then evacuated and, depending on the drying conditions, a porous solid can eventually be obtained [Brinker & Scherer 1990, chap. 8]. As initially suggested by Iler [Iler 1979] for the polymerization of silicic acid, the condensation of the precursors can lead to the formation of dense colloidal particles, that afterwards aggregate until their clusters fill the space, at which moment a gel is obtained. The synthesis variables that determine the texture of the gels are generally those affecting the balance between hydrolysis and condensation of the precursors, such as pH, water content, dilution, and so on. The drying of the gels in conditions that tend to preserve its solid structure generally leads to highly porous materials having a complex hierarchical microstructure.

Various aggregation models have been proposed that account for the influence of the synthesis conditions on the structure of the gels. For instance, the concept of reaction or diffusion limited aggregations can explain the effect of the synthesis conditions, such as pH and water concentration, on the structure of silica gels [Beelen *et al.* 1994; Himmel *et al.* 1995], which growth processes are also confirmed at the molecular scale by NMR [Brinker & Scherer 1990; Devreux *et al.* 1990]. In order to match the models' predictions with experimental data, many modifications were made to the original pure aggregation models [Kolb *et al.* 1983; Meakin 1983]. For instance, a pure aggregation model predicts infinite gel times [Hasmy & Jullien 1995]; allowance of a local reorganization of the aggregates during their formation leads to finite gel times [Jullien & Hasmy 2005; Ma *et al.* 2002a]. Some mechanical properties of the samples can be accounted for by the reorganization of the aggregates [Ma *et al.* 2002b], as well as by purely geometrical models that are not derived from any aggregation process, such as random Gaussian fields [Berk 1987; Roberts & Garboczi 2000]. The latter model can also be used to analyze the low angle scattering patterns of silica gels [Quintanilla *et al.* 2003].

A recent trend in sol-gel science is the use of hybrid organic-inorganic precursors to synthesize materials with novel properties [Avnir *et al.* 1998]. The present thesis deals with the structure of hybrid silica xerogels and xerogel catalysts. The materials are synthesized by co-polymerizing tetraethoxysilane with organically modified trialkoxisilane molecules, the latter possibly forming a complex with an active metal cation [Alié *et al.* 1999; Heinrichs *et al.* 1997b; Lambert *et al.* 2004d]. This particular synthesis is referred to as the co-gelation; it leads to materials with interesting properties in terms of metal dispersion in the catalyst, and also in their ability to preserve a large porosity during desiccation.

The present introductory chapter presents the sol-gel process in general, and the cogelation method in particular. Some experimental results obtained with cogelled samples are briefly summarized. The outline of the thesis is integrated in the conclusion of the present chapter.

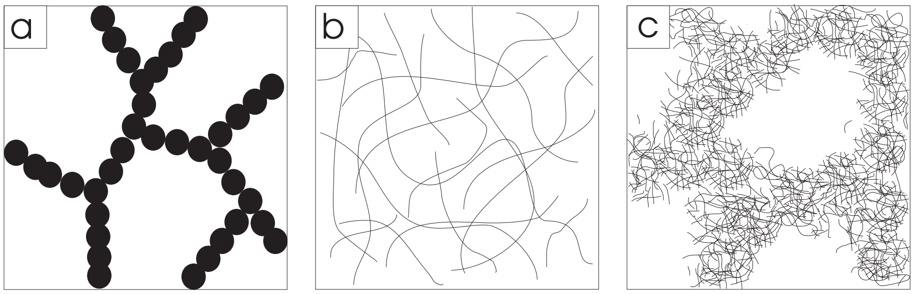

Figure 1.1: Three different types of gels: (a) colloidal or particulate gel, (b) polymeric gel, and (c) phase separated polymeric gel.

## 1.2 The sol-gel process

### 1.2.1 Gels and gelation

The first step of the sol-gel process is the polymerization of precursor molecules in a solvent until a gel is obtained. Quite generally, a gel is a system composed mainly of liquid, that behaves macroscopically like a solid [Flory 1971]. The gels are classified into *chemical* and *physical* gels [Flory 1971]. In the former, the network that is responsible for the solid-like macroscopic behaviour of the gels is made of strong covalent links. In the latter, the weaker Van der Waals physical intermolecular forces contribute to the stiffness of the gels. A macroscopic characteristic of physical gels is the fact that gelation is reversible, and that the gels become fluid again when they are heated above the gel temperature. Most gels encountered in inorganic sol-gel process are chemical [Brinker & Scherer 1990].

As the very name of the sol-gel process suggests, the mechanism that is most often invoked for explaining the formation of the gel is *via* an intermediate sol phase, *i.e.* a colloidal suspension of solid particles. The particles aggregate, and a gel is obtained when their clusters fill the space and begin to inter-penetrate [Dietler *et al.* 1986]. This specific type of gel is referred to as *particulate* or *colloidal* [Brinker & Scherer 1985; 1990]. The use of time-resolved scattering techniques confirmed the aggregation mechanism of gelation for a large variety of systems, such as $SiO_2$ [Blanco *et al.* 1992; Dietler *et al.* 1986; Schaefer & Keefer 1984; Vollet *et al.* 2001], $TiO_2$ [Kallala *et al.* 1993; Lebon *et al.* 1992] and $ZrO_2$ [Chaumont *et al.* 1992; Lecomte *et al.* 2000]. Figure 1.1a illustrates the typical microstructure of a particulate gel.

Not all gels, however, are particulate, and not even biphasic. The structure of many gels encountered in every day life, such as jelly, gelatine, hair gel and so forth, is monophasic. The polymer and the solvent are intimately mixed, at the molecular scale, as illustrated in Figure 1.1b [Osada & Gong 1998; Tanaka 1981]. These gels are referred to as *polymeric* [Brinker & Scherer 1985]. Small angle X-ray scattering and rheological measurements show the existence of polymeric silica gels. These gels are usually obtained from the polymerization of silicon alkoxides in acidic conditions [Brinker & Scherer 1985; 1990; Schaefer & Keefer 1984].

Gels can also evolve from a monophasic polymeric structure to a biphasic structure *via* a phase separation process, during which the polymer and the solvent segregate into two distinct phases: polymer-rich and solvent-rich [Tanaka 1981; Tanaka *et al.* 1979]. This phenomenon is frequently encountered with organic gels, where it is often associated with turbidity because the size of the phase separated domains can be comparable with the wavelength of visible light [Tanaka 1981]. Phase separation can be driven by various external parameters such as pH and temperature; it can also occur as a consequence of the very chemical reactions leading to the formation of the gel. This has been reported notably for resorcinol/formaldehyde organic gels [Pekala & Schaefer 1993; Schaefer *et al.* 1995], for some hybrid ormosil-like materials [Ulibarri *et al.* 1992], for silica materials synthesized with organic co-reactants [Kaji *et al.* 1995; Nakanishi 1997; Schaefer *et al.* 2004], and also for some pure silica materials [Nakanishi 1997]. In a review of $^{29}$Si NMR studies on the polymerization of silicon alkoxides, Sefcik & McCormick [1997] consider phase separation such an important phenomenon that they discuss it on the same footing as hydrolysis and condensation.

Reaction-induced phase separation can occur whenever the chemical reaction brings the molecules into a state where they are no longer miscible with the solvent. During a polymerization reaction, this can result from the lowering of the entropy of mixing that accompanies the growth of the molecular weight [deGennes 1979b; Flory 1971; Olabisi *et al.* 1979]. In the frame of the Flory-Huggins theory of polymer solutions, the critical temperature $T_c$ at which a phase separation begins is given by [Billmeyer 1984]

$$\frac{1}{T_c} = \frac{1}{\Theta}\left(1 + \frac{C}{M^{1/2}}\right) \tag{1.1}$$

where $C$ is a constant, $M$ is the molecular weight, and the Flory temperature $\Theta$ is the limit of the critical temperature for infinite molecular weights. During a polymerization reaction, if the molecular weight increases to such an extent that $T_c$ exceeds the processing temperature, a phase separation is triggered. Similar effects occur when increasing the branching of polymeric species [Clarke *et al.* 1995]. During the polycondensation of silicon alkoxides, enthalpic contributions may also play an important role in triggering the phase separation, as the condensation removes highly polar OH groups from the condensing molecules [Kaji *et al.* 1994; Nakanishi 1997]. During a reaction-induced phase separation of a gelling solution, there is no relation between gelation and phase separation: the gel point can occur before or after the phase separation.

Phase separation can lead to a wide variety of morphologies. For instance, it has been proposed that the Stöber process for the synthesis of silica colloids [Stöber *et al.* 1962] is governed by a phase separation. Under the synthesis conditions of the Stöber process, the rate of hydrolysis is so high that the solution supersaturates in silicic acid [Lee *et al.* 1997]. The growth of the colloids is then initiated by classical nucleation. In certain conditions, the nucleated colloids may aggregate to form a gel [Martin & Odinek 1990]. Therefore, the classification of the gels on the basis of their structure is not necessarily relevant for the physico-chemical processes that govern their formation.

### 1.2.2 Drying of the gels

The second step of the sol-gel process is the drying of the gel. In the context of the synthesis of porous materials, the specific method of drying is chosen to preserve the structure of the gels' skeleton.

The materials obtained by the evaporative drying of a gel are called xerogels, which means literally 'dry gels'. During an evaporative drying (Figure 1.2), menisci appear at the external surface of the gel, and put its skeleton under pressure. The capillary pressure depends on the radius of curvature $r$ of the menisci, according to Laplace law

$$P_c = \frac{2\gamma\cos(\theta)}{r} \tag{1.2}$$

where $\gamma$ is the surface tension of the liquid, $\theta$ is its contact angle with the solid phase of the gel. When drying proceeds, the curvature of the menisci increases, by which the

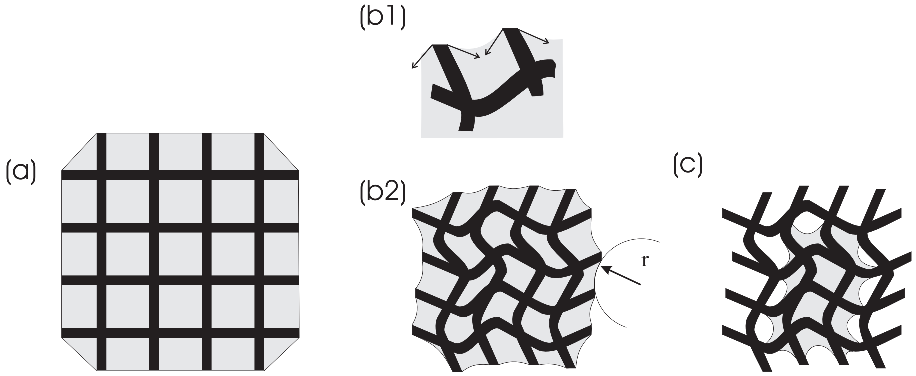

Figure 1.2: Evaporative drying of a gel. When a gel (a) is dried, menisci appear at its external surface (b1) that put its skeleton in compression, the skeleton progressively shrinks (b2) and stiffens accordingly; when the critical point of drying (CPD) is reached, the skeleton stops shrinking and the drying front penetrates into the material (adapted from Brinker & Scherer [1990, Chap. 8]).

gel shrinks. This leads to an increase of the mechanical stiffness of the skeleton as its constituting elements become jammed together. The critical point of drying is reached when the skeleton stops shrinking, and when the drying front penetrates deep into the material. At that point, the radius of curvature of the menisci is comparable with the size of the largest pores that percolate through the macroscopic sample. As the drying front penetrates into the material, the compressive stress exerted on the gels skeleton lowers and the macroscopic shrinkage stops. The total amount of shrinkage during evaporative drying therefore results from the balance between the stiffness of the gel's skeleton and the pore-size-dependent capillary pressure. For instance, the evaporation of ethanol with $\gamma \simeq 20$ mJ/m$^2$ [Dean 1992] and $\theta = 0$, through pores with $r = 20$ nm, leads to a capillary pressure $P_c \simeq 20$ MPa (Equation 1.2), corresponding to 200 times the atmospheric pressure.

In order to minimize the compaction of the skeleton that accompanies the desiccation of the gels, a method initially proposed by Kistler is the supercritical extraction of the solvent [Brinker & Scherer 1990]. This consists in putting the gel in conditions of pressure and of temperature where its solvent is in supercritical state. Above the critical point, there is no difference between the vapor and the liquid state, and the solvent can be removed from the pores without creating any meniscus. The porous solids thus obtained are called aerogels. This route is sketched in Figure 1.3. In practice, supercritical extraction of

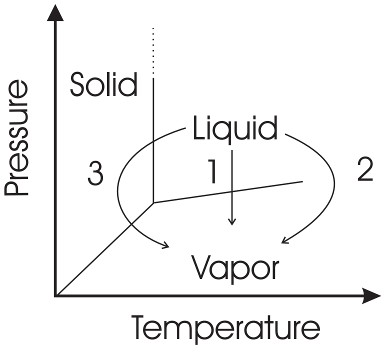

Figure 1.3: Schematic phase diagram of the liquid filling the pores of a gel. Various possible ways of drying are: (1) evaporative drying (the liquid-vapor line is crossed); (2) supercritical drying (the liquid-vapor line is bypassed); (3) freeze drying (the solvent is first frozen and then sublimated). The latter two techniques aim at avoiding the appearance of menisci that would reduce the gels' porosity.

a solvent is often facilitated by its preliminary exchange by another solvent with a low critical point. For instance $CO_2$ supercritical drying typically consists in washing the gel with supercritical $CO_2$ followed by a depressurization.

A third way of extracting the solvent is freeze drying, by which the solvent is frozen and then sublimated. This also avoids the appearance of menisci that would compress the gels's structure, but the skeleton is generally damaged by the growth of the solvent's crystals during its freezing. The porous solids obtained are called cryogels.

## 1.3 The cogelation method

### 1.3.1 Cogelled xerogel catalysts

The cogelation method enables synthesizing metallic catalysts supported on silica xerogels, following a method developed by Heinrichs *et al.* [1997b] and initially explored by the group of Schubert [Breitscheidel *et al.* 1991; Mörke *et al.* 1994]. According to this technique, a tetraalkoxysilane of general formula $Si(OR)_4$ is copolymerized with an organically substituted trialkoxysilane of the type $(R'O)_3Si$-X-A. In these formulae, R and R' are alkyl groups. A is a functional organic group able to form a chelate with a cation of metal, linked to the hydrolysable silyl group $(R'O)_3Si$ *via* an inert and hydrolytically stable spacer X. A list of the organically modified trialkoxysilane molecules tested in the Department of

Chemical Engineering of the Université de Liège are reported in Table 1.1.

The chemical reactions involved in the gel formation are hydrolysis and condensation. The hydrolysis of the tetraalkoxysilane can be written as

$$\mathrm{Si(OR)_4 + nH_2O \rightarrow Si(OR)_{4-n}(OH)_n + nROH} \tag{1.3}$$

where $n$ can take any value from 1 to 4. Similarly, the hydrolysis of the modified trialkoxysilane and of its complex with a metal ion, obeys

$$\mathrm{Si(OR')_3 - XA + nH_2O \rightarrow Si(OR')_{3-n}(OH)_n - XA + nR'OH} \tag{1.4}$$

where $n$ can take any value from 1 to 3. Two partially hydrolyzed molecules can link together by any of the following condensation reactions

$$\begin{aligned} \cdots\mathrm{SiOH + HOSi}\cdots &\rightarrow \cdots\mathrm{SiOSi}\cdots + \mathrm{H_2O} \\ \cdots\mathrm{SiOY + HOSi}\cdots &\rightarrow \cdots\mathrm{SiOSi}\cdots + \mathrm{YOH} \end{aligned} \tag{1.5}$$

where, in the second reaction, Y can be either R or R' according to whether the condensation concerns a tetraalkoxysilane-derived or a trialkoxysilane-derived molecule.

The general method was used to synthesize Pd/$SiO_2$, Ag/$SiO_2$, Cu/$SiO_2$ monometallic catalysts [Heinrichs *et al.* 1997b; Lambert *et al.* 2004a;c;d; Sacco *et al.* 2005], and Pd-Ag/$SiO_2$, Pd-Cu/$SiO_2$ bimetallic catalysts [Heinrichs *et al.* 1997a; Lambert *et al.* 2005]. For low metal loadings, about 1 wt.% metal, the overall structure of these materials, after evaporative drying, calcination and reduction, is that of metallic crystallites finely dispersed inside a low density xerogel structure (see Figure 1.4). As assessed by CO or $O_2$ chemisorption, the typical size of the metallic particles is 3 nm, which agrees also well with the width of X-ray diffraction peaks and with direct microscopic observation [Lambert *et al.* 2004d]. Interestingly, it seems from Transmission Electron Microscopy (TEM) that the metallic crystallites are buried inside the silica skeleton [Heinrichs *et al.* 1997a;b; Lambert *et al.* 2004a;c;d; 2005; Sacco *et al.* 2005], which seems also to be compatible with some preliminary X-ray Photo-electron Spectroscopy (XPS) analyses [Heinrichs *et al.* 2002]. Notwithstanding their localization inside the silica, the crystallites are accessible, as demonstrated by chemisorption and by the high catalytic activity. For higher metal

Table 1.1: Some organically modified trialkoxisilane molecules used in the cogelation method, their symbol and references.

| Symbol | Formula | References |
|---|---|---|
| PMS | 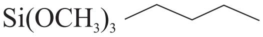 | Alié *et al.* [2001] |
| AMS | 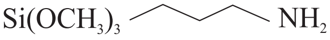 | Alié *et al.* [2001] |
| EDAS | 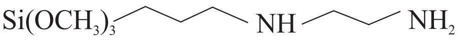 | Alié *et al.* [1999]; Heinrichs *et al.* [1997b]; Lambert *et al.* [2004d] |
| Si-Acac | 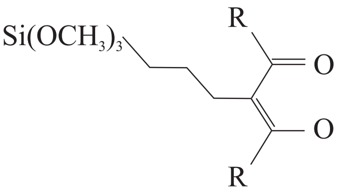 | Lambert *et al.* [2004c] |
| Si-PzPy | 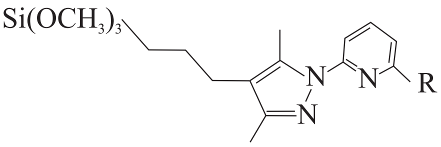 | Sacco *et al.* [2004; 2005] |
| AES | 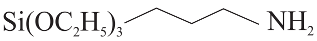 | Alié *et al.* [2001]; Heinrichs *et al.* [1997a] |
| EDAES | 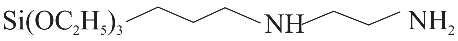 | Alié *et al.* [2001]; Lambert *et al.* [2004a] |

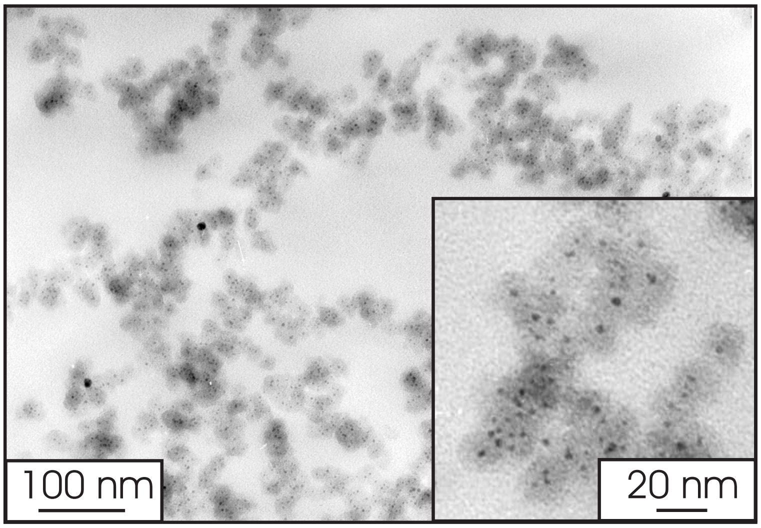

Figure 1.4: Transmission Electron Micrograph of a Pd-Ag/$SiO_2$ xerogel catalyst synthesized by co-polymerizing EDAS-Pd and AES-Ag complexes with TEOS (courtesy of B. Heinrichs).

loadings, a significant amount of metal is also present outside of the silica skeleton, under the form of large crystallites with a width of a few ten nanometers [Lambert *et al.* 2004d].

The fact that the metallic particles in the final materials are located inside the silica skeleton offer these materials interesting catalytic properties. Because the metal particles are immobilized inside the support they are sinterproof. The catalysts can withstand high temperatures without undergoing any significant deactivation [Heinrichs *et al.* 2003]. As the reactants have to find their way through the microporosity of the silica to reach the active metal particles, the materials also offer the prospect of shape selectivity.

To explain the systematic positioning of the metallic nanoparticles inside the silica skeleton in cogelled catalysts obtained by copolymerizing EDAS with TEOS, Heinrichs *et al.* [1997b] proposed a nucleation model summarized in Figure 1.5. The underlying idea of the model is that EDAS is more reactive towards hydrolysis than TEOS, owing to the presence of methoxy groups instead of ethoxy. It is therefore likely that EDAS condenses first, leading to nuclei around which TEOS can later condense. The aggregation of the EDAS-TEOS particles would afterwards lead to the gelation of the sol, according to the principles governing the formation of colloidal gels [Brinker & Scherer 1990; Iler 1979]. Assuming that the number of EDAS molecules per nucleus is independent of the

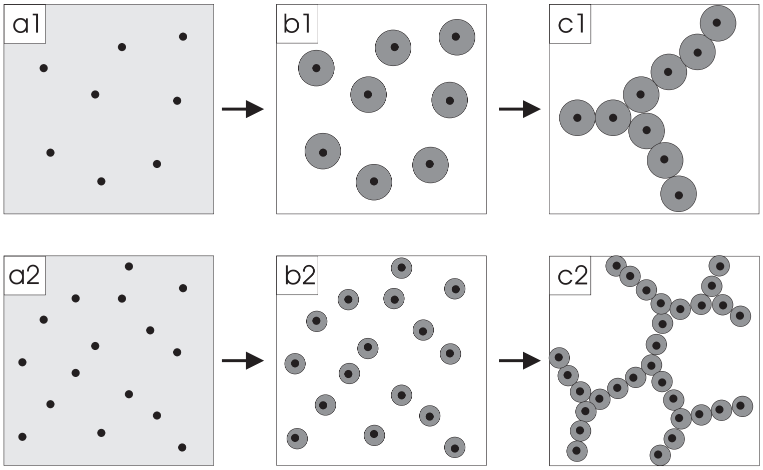

Figure 1.5: Nucleation-Growth-Aggregation mechanism proposed for the formation of cogelled samples, to account for the position of the metal inside of the silica and for the effect of increasing the amount of coreactant on the size of the structures [Alié *et al.* 1999; Heinrichs *et al.* 1997b]. The coreactant polymerizes first, leading to nuclei (a1) around which the main precursor condenses (b1). The system gelifies when the particles aggregate (c1). Increasing the amount of coreactant leads to more numerous nuclei (a2); for a given amount of main precursor, the particles are necessarily smaller (b2), and so are their aggregates (c2).

concentration of EDAS and TEOS, the nucleation mechanism should lead to the following relation between the diameter $d$ of the final particles and the EDAS/TEOS molecular ratio

$$d^3 = C\left(1 + \frac{[TEOS]}{[EDAS]}\right) \tag{1.6}$$

where $C$ is a constant. When silica particles are looked for and measured in TEM micrographs such as those of Figure 1.4, a reasonable agreement is found with Equation 1.6, for a wide variety of co-reactants having a higher reactivity than the main precursor. Surprisingly, this relation is also found to apply for catalysts synthesized from EDAES and TEOS, while no nucleation effect would be expected from the presence of ethoxy groups on both molecules [Lambert *et al.* 2004a].

### 1.3.2 Cogelled metal free xerogels

If a nucleation mechanism controls the formation of the cogelled materials, their structure should depend only on the difference in reactivity of the main silica precursor and of the co-reactant. To check this, Alié *et al.* tested a large variety of couples of main silica

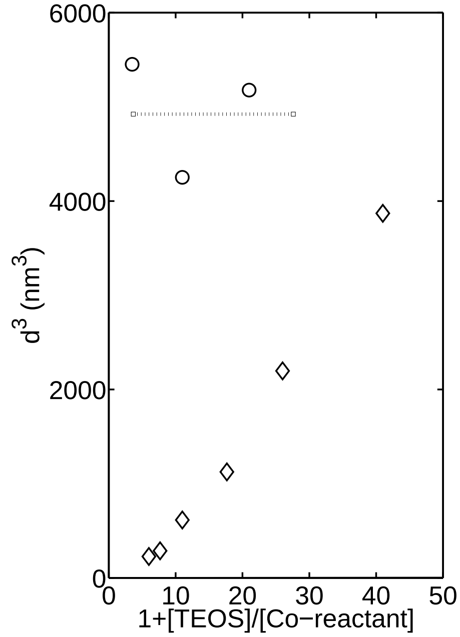

Figure 1.6: Relation between particle diameter $d$ and relative concentration of co-reactant and TEOS: (◊) EDAS-TEOS xerogels and (∘) AES-TEOS xerogels (see Table 1.1). The data are taken from Alié [2002].

precursors and of co-reactants [Alié *et al.* 1999; 2001]. The general finding is that whenever the co-reactant has a larger reactivity towards hydrolysis than the main silica precursor, increasing the amount of co-reactant shifts the microstructure of the final xerogels towards smaller sizes, in agreement with Equation 1.6. This is exemplified in Figure 1.6 in the case of EDAS-TEOS cogelled xerogels. On the contrary, when the co-reactant has the same reactivity as the main silica precursor, such as AES cogelled with TEOS, or EDAS cogelled with tetramethoxysilane (TMOS), the concentration of co-reactant has no effect on the size of the microstructure (Figure 1.6).

The role of the organic moiety of the co-reactant is less clear. The gel times of samples obtained by copolymerizing EDAS or AMS with TEOS are significantly shorter than those observed when co-polymerizing PMS with TEOS. It therefore seems that the amine of EDAS and AMS could contribute to catalyze the gel-forming reactions [Alié *et al.* 2001].

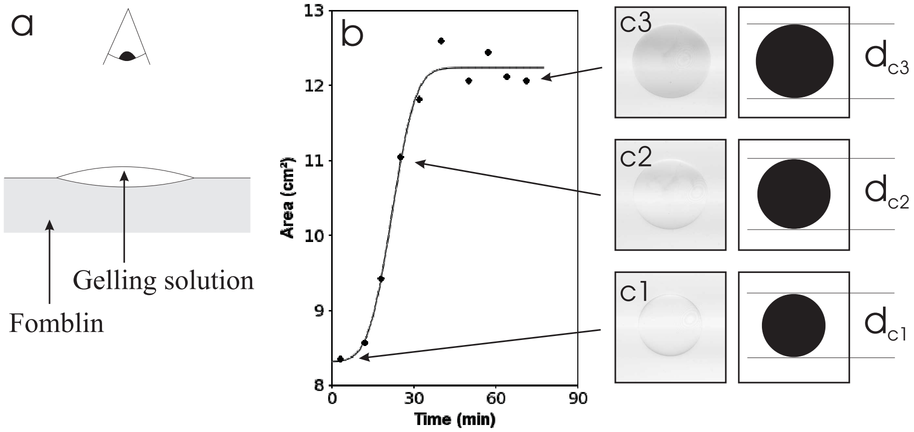

Figure 1.7: Example of a lens of reacting EDAS-TEOS solution spreading over a Fomblin bath, as a function of time: (a) a drop of the gelling solution floats over Fomblin® and it is observed from above, (b) and (c) the area of the lens increases with reaction time. Note that $d_{c1} < d_{c2} < d_{c3}$.

### 1.3.3 Farrago of observations about cogelled samples

The cogelled samples synthesized with a large variety of co-reactants share some common textural characteristics. For instance, they all are low density xerogels, with densities that can be as low as 0.3 g/cm$^3$ even after evaporative drying [Alié *et al.* 1999; 2001]. So low values can generally be obtained only through a supercritical drying [Brinker & Scherer 1990]. Similarly, very large pores are observed in cogelled xerogels, with sizes of more than 100 nm, while the pore sizes of pure silica gels is generally a few ten nanometers, *e.g.* [Scherer 1995]. Therefore, the co-reactant presumably plays an important role, that is not necessarily related to its reactivity towards hydrolysis and condensation.

Some observations on cogelled samples hint at physical rather than chemical effects. In the particular case of the co-polymerization of EDAS and TEOS, the surface tension of the solution decreases with reaction time. This is illustrated in Figure 1.7. A drop of a few ml of the gelling solution is deposited on the surface of a non miscible and denser liquid (Fomblin®, a perfluorinated polyether lubricant). The drop immediately takes the form of a flat circular lens (Figure 1.7c1), with an area that progressively increases with reaction time. As the hydrodynamic relaxation times are much shorter than the observed kinetics [Fermigier 1999], the spreading points at a lowering of the surface tension of the gelling solution.

Another general observation with co-gelled samples is that some gels can be destabilized by heating them rapidly after the gel point, by dipping the synthesis flask into a thermostatic bath a few ten degrees warmer than room temperature. This results in a liquid that can be either stable or that can gelify again. The fact that an increase in temperature can bring the gel to a liquid state is reminiscent of physical gels, in which weak intermolecular forces contribute to the gelation.

## 1.4 Conclusion

Cogelation is an efficient method to synthesize heterogeneous catalysts supported on silica, with interesting properties in terms of activity and of selectivity. The two main characteristics of these catalysts are (i) that they can withstand evaporative drying and maintain a high aerogel-like porosity and (ii) that the metallic particles of the active metal seem to be buried inside the microporous silica skeleton, which could be the reason why they are sinter-proof.

A nucleation-growth-aggregation model has been proposed (Figure 1.5) by various reaserchers [Alié *et al.* 1999; Heinrichs *et al.* 1997b; Lambert *et al.* 2004d] to account for the textural differences of the xerogels synthesized with various co-reactants. The model is, however, mainly supported by the textural characterization of the final dry and calcined materials, and it fails to explain the common features of all cogelled samples that make them different from pure silica xerogels. Therefore, the physicochemical mechanisms that govern the formation of cogelled catalysts and of co-gelled metal-free xerogels are to a large extent unknown.

The positioning of the metal particles inside the silica skeleton in cogelled catalysts is only supported by TEM observations. Chapter 2 re-examines the localization of palladium particles in cogelled catalysts using electron tomography. This technique provides 3D images of the catalysts at the nanometer scale. The tomograms are analyzed quantitatively using digital 3D image analysis.

In Chapter 3, the formation of the nanostructure of the Pd/$SiO_2$ gels analyzed in Chapter 2 is followed *in situ* using time-resolved Small Angle X-ray Scattering (SAXS). The same experimental technique is used in Chapter 4 to analyze the formation of the nanometer structure of EDAS-TEOS and AES-TEOS cogelled samples, without any metal.

In chapter 5, the microstructure of EDAS-TEOS and AES-TEOS xerogels is analyzed by combining different experimental techniques as electron microscopy coupled with digital image analysis, SAXS, pycnometry and nitrogen adsorption-desorption measurements. The textural characterization data are critically analyzed in the light of the physicochemical mechanism unraveled by *in situ* SAXS in Chapter 4.

Chapter 6 deals with the effect of drying on the microstructure of EDAS-TEOS and AES-TEOS gels. The gels are characterized through beam bending measurements. The corresponding aerogels are characterized by SAXS, nitrogen adsorption and mercury porosimetry. The textural characteristics of the gels, aerogels and xerogels are compared.

Chapter 7 summarises the main findings of the thesis.

# Chapter 2

# Electron tomography analysis of cogelled Pd/SiO$_2$ xerogel catalysts

## 2.1 Introduction

In this chapter the localization of the metallic particles within the silica support in Pd/SiO$_2$ cogelled catalysts is investigated. The interest of this study is twofold. On one hand it may help understand the catalytic properties of the investigated materials, such as the absence of physical limitations [Heinrichs *et al.* 2001] or the very slow deactivation [Heinrichs *et al.* 2003]. On the other hand, the localization of the metal in the final material may give some clue about the physicochemical mechanism that govern the formation of the material's nanostructure. In particular, as discussed in Chapter 1, it has been suspected for long that the metallic particles could be buried in the middle of silica skeleton, which gave birth to the idea of a nucleation-growth-aggregation mechanism (see Figure 1.5 on page 11).

The experimental data available so far, on the basis of which the nucleation model was proposed, are mainly based on transmission electron microscopy (TEM). As this technique only gives access to the projection of the investigated objects, it is difficult to reach final conclusions about the localization of the metallic particles. The present study is based on electron tomography (3DTEM), which enables 3D images of the microstructures to be obtained at the nanometer scale, a technique that is receiving a growing interest in both materials science [Janssen *et al.* 2003; Koster *et al.* 2000; Weyland & Midgley 2004; Ziese *et al.* 2004] and in biology [Frank 1992].

The present chapter aims at answering the following questions: *Does 3DTEM confirm* *that the metallic particles are located inside the silica? What else can be learned on the spatial distribution of the metallic particles from 3DTEM?*

Two Pd/$SiO_2$ samples with different metal loadings, synthesized by the cogelation method described in the introduction, are analyzed by 3DTEM. The two samples were chosen because they are representative of catalysts with well dispersed and badly dispersed metal, respectively. In order to fully exploit the unique structural information obtained through 3DTEM, the tomograms are analyzed using digital image analysis techniques, with methods derived from spatial statistics. The morphological data extracted from the 3D images are also analyzed in the light of previously published textural information obtained on the catalysts.

## 2.2 Experimental Section

### 2.2.1 Preparation of the xerogel catalysts

The general method for preparing the Pd/$SiO_2$ xerogel catalysts analyzed in this paper has been described elsewhere [Lambert *et al.* 2004d]. Palladium acetylacetonate powder (Pd(acac)$_2$) and 3-(2- aminoethyl)aminopropyltrimethoxysilane (EDAS, in Table 1.1 on page 9) are mixed together in ethanol. The slurry is then stirred at room temperature for about half an hour, until a clear yellow solution is obtained, which is characteristic of a palladium complex. After addition of tetraethoxysilane (TEOS), a solution of aqueous 0.18 M $NH_3$ in ethanol is added to the mix. The vessel is then closed and the solution is left to age for 7 days at 60°C. The samples are then dried in an oven where, over a period of a week, the temperature is raised from 60°C to 150°C and the pressure is lowered to 1200 Pa. The dry samples are calcined under an air flow, with a progressive increase of temperature from room to 400°C with a heating rate of 120°C/h, and maintained at this temperature for 12 h. Reduction of the samples is performed under a $H_2$ flow, the samples are heated to 350°C at a rate of 350°C/h and maintained 3 h at that temperature.

Two samples are analyzed in the present study, the synthesis conditions of which are reported in Table 2.1. The same hydrolysis ratio, $H_2O/(TEOS + 3/4\ EDAS) = 5$, dilution ratio Ethanol/(TEOS+EDAS) = 10, and complexation ratio EDAS/Pd(acac)$_2$ = 2 are used for the two samples, only the amount of Pd salt is modified. In order to ease the

Table 2.1: Synthesis of the Pd/$SiO_2$ xerogel catalysts.

| | $Pd(acac)_2$ (g) | EDAS ($cm^3$) | TEOS ($cm^3$) | $NH_3$ 0.18 M ($cm^3$) | $C_2H_5OH$ ($cm^3$) |
|---|---|---|---|---|---|
| Pd1.1 | 0.097 | 0.14 | 12.3 | 5.0 | 32.6 |
| Pd3.1 | 0.206 | 0.30 | 12.1 | 5.0 | 32.6 |
| Pd4.5[a] | 0.433 | 0.62 | 11.8 | 5.0 | 32.6 |

[a] this sample is not discussed in the present chapter.

comparison with previous work conducted on the samples [Lambert *et al.* 2004d], they are called Pd1.1 and Pd3.1, which names are derived from their actual metal loading (1.1 and 3.1 wt.% respectively). The values are slightly higher than the theoretical loading that could be estimated from Table 2.1, owing probably to a loss of un-polymerized TEOS or EDAS during the drying [Lambert *et al.* 2004d].

### 2.2.2 Electron microscopy

For preparing the microscopy grids, the samples are first ground in a mortar into very fine powder. A small amount of powder is then dispersed in ethanol for a few minutes in a sonication bath. The dispersion is finally left to rest for another few minutes, a drop of the supernatant is put on the microscopy grid and the solvent is evaporated.

The TEM observation was performed on a Tenai20FEG microscope (FEI co.) operated at 200 kV. Projection images under sample rotation angles from -70° to +70° (1° increment) are automatically acquired with Inspect3D (FEI) on a slow scan CCD camera (Gatan). At a magnification of 25000 × the nominal pixel size in the CCD images was 0.7 nm.

Figure 2.1 represents three TEM micrographs of a fragment of Pd1.1 catalyst viewed under three different angles corresponding to *ca* -20°, 0° and +20°. On the images, the translucent grey object is the silica skeleton and the black dots are the palladium nanoparticles, which are mostly visible in the insets. From a single of these micrographs, the exact positioning of the Pd particles would be impossible to assess, because only a projection of the structure is accessible. However by comparing the three micrographs, corresponding to projections along three different directions, it can be inferred that the visible Pd particles are located inside the silica, not on its surface.

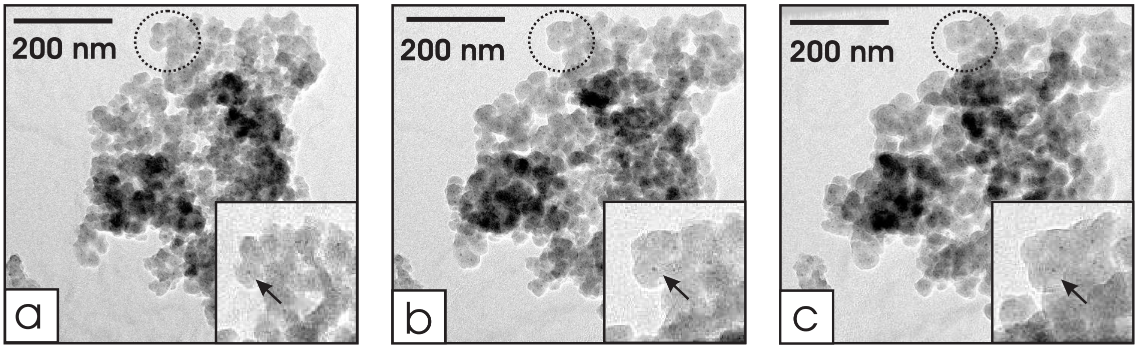

Figure 2.1: Examples of projections of a fragment of sample Pd1.1 along three different angles corresponding *ca* to (a) -20°,(b) 0° and (c) +20°. The insets are magnified views of the circled zones, in which it appears that the particles are located inside the silica.

Actually, the information contained in the 2D projections of a given object along an infinity of different directions is equivalent to that contained in the original 3D object. In this study, the 3D structure was gained by weighted backprojection, after alignment of the projections with respect to a common origin by fiducial markers by the IMOD software [Mastronarde 1997]. The observed low contrast between silica and carbon foil can possibly be assigned to sample contamination (carbon buildup) during acquisition. Due to the limited angular range in the projections (missing wedge of information in Fourier space), image features (*e.g.* the metal particles) appear elongated in the z direction of the reconstructions. Moreover, certain particles also appear bent due to imperfect alignment of the projection images.

The main purpose of the present study is not the characterization the Pd particles themselves -a problem that has been satisfactorily addressed by chemisorption and X-ray diffraction [Heinrichs *et al.* 2002; Lambert *et al.* 2004d]- but their localization with respect to the silica skeleton, for which problem 3DTEM is the ideal experimental technique. On the low resolution tomograms used in the present study the localization of the Pd particles is unambiguous. As the size of the Pd nanoparticles is only slightly larger than a few voxels their shape is poorly represented. The advantage of using low resolution images is the large number of metal particles that can be analyzed at once. Typically, a single analyzed 3D image contains about 1000 particles, which can easily be handled with digital image analysis, and enables statistically significant conclusions to be drawn.

### 2.2.3 Image Segmentation

The structure of the Pd/$SiO_2$ xerogel catalysts is triphasic as it contains (i) the silica skeleton, (ii) the pore space, and (iii) the palladium nanoparticles. However, the raw data obtained from electron tomography provides only grey level images corresponding to the electron optical density of the various points of the structure. The purpose of segmentation is to take advantage of the different grey levels associated with the phases to discriminate to which phase each voxel of the 3D image belongs. The segmentation is a necessary preliminary step to extract quantitative morphological information from the 3D tomograms. The image analysis presented in this paper was performed using the Matlab® software together with its Image Processing toolbox and the SDC® morphology toolbox.

Although the images of the samples obtained by electron tomography are 3D by nature, processing them using general 3D tools would present some difficulties. Typically, the analyzed 3D images are a stack of *ca* 400 images of 400 × 400 pixels; when treated in double precision, such a structure requires approximately 512 Mbytes. Processing such an image as a single object would be very time consuming. Moreover, this would also make difficult to assess the accuracy the image analysis, because it is difficult to visualize 3D triphasic systems at each step of the processing. Therefore, the segmentation of the images is performed sequentially on groups of neighboring slices, as described hereafter.

The first step of the segmentation is the discrimination between silica skeleton and pore space, which is illustrated in Figure 2.2. Figure 2.2a is a typical 2D image of the interior of a fragment of the Pd/$SiO_2$ xerogel catalyst, corresponding to a slice taken out of the 3D image. Before describing the image processing, it is useful to recall that the visual appearance of an image is not necessarily representative of its actual content, especially for poorly contrasted images such as in Figure 2.2a. The reason is that the eye does not perceive with an equal acuity all grey levels. A so-called histogram equalization [Russ 2002] is therefore applied to the original image to enhance the contrast, and to help the reader judge the value of the image processing (Figure 2.2b). The processing is as follows. (i) A low pass filter is first applied to the original slice (Figure 2.2a) in order to denoise it and to smooth the palladium particles out. For that purpose, the four adjacent slices surrounding that of Figure 2.2a are averaged pixel by pixel. The resulting image is then passed through

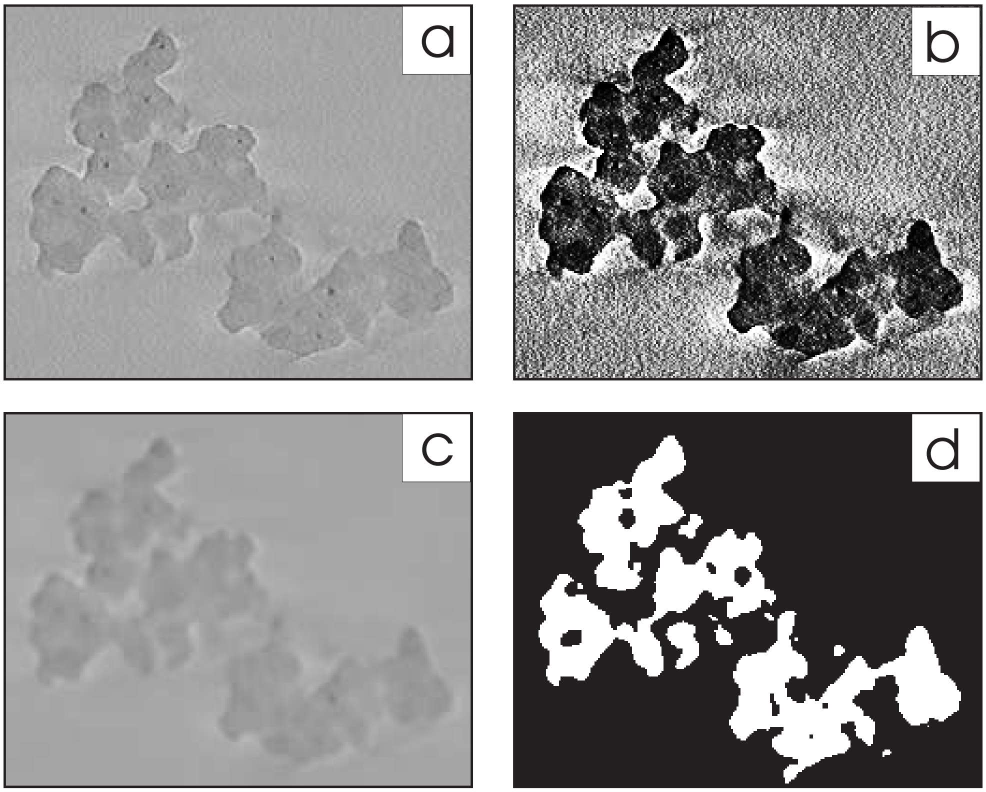

Figure 2.2: Segmentation of the silica skeleton: (a) original 2D slice taken out of the 3D tomogram, (b) same image after histogram equalization showing the connectivity of the silica, (c) low-pass filtered image and (d) final binary image after thresholding and closing.

a 5×5 pixels averaging filter (Figure 2.2b). (ii) The filtered image is subsequently binarized by assigning the value 1 to all pixels with an intensity below a given threshold and 0 to the others. Practically, the optimum threshold is calculated from the histogram of grey levels of the image, using Ostu's method [Otsu 1979]. A single threshold is calculated from a representative 2D slice taken in the middle of the 3D image and the same value is used for all the other slices. (iii) After the thresholding step, some small black holes are still present in the image; they are removed by applying a closing filter [Russ 2002; Soille 1999]. The final binary image of the silica skeleton is that of Figure 2.2d. The shape of the binary object is globally accurate, as can be seen by comparing Figures 2.2b and 2.2d. It should also be stressed that the binary 2D image in Figure 2.2d should not be considered individually, as it belongs to a 3D structure obtained by stacking similar images. For instance, the parts of Figure 2.2d that first seem to be disconnected from one another, actually belong to a single connected 3D binary object.

The segmentation of the palladium particles requires a more involved processing because of the low resolution of the images. The particles are only a few pixels wide and elaborate methods are needed to discriminate them from the noise. The used method is presented in Figure 2.3. It takes advantage of both non local properties of the images, based on the comparison of each pixel with its neighborhood, and of local properties based on the intensity of any given pixel. The two complementary approaches correspond to the left and right branches of Figure 2.3. As a very first step, the images are denoised by averaging three adjacent slices (Figure 2.3a). In order to highlight the local minima (non local property) of the resulting image, a so called top-hat filter is applied (Figure 2.3b) [Soille 1999]. The top-hat image $I_{\mathrm{th}}$ contains bright spots that are generally not isolated, and applying a threshold to it would generally not result in isolated compact objects. Therefore, the erosion gradient $I_{\mathrm{eg}}$ of the original image is also computed (Figure 2.3c) [Soille 1999]. By this operation, a bright boundary is created around each local minimum of the original image. Creating a new image with pixels that have the value 1 wherever $I_{\mathrm{th}}$ is larger than $I_{\mathrm{eg}}$, results in a binary image in which all the local minima are clearly disconnected (Figure 2.3d). Obviously, only a small fraction of the minima visible in Figure 2.3d corresponds to Pd particles. In order to eliminate the minima located in the pore space, the minima image is intersected with the binary image of the silica skeleton previously computed as

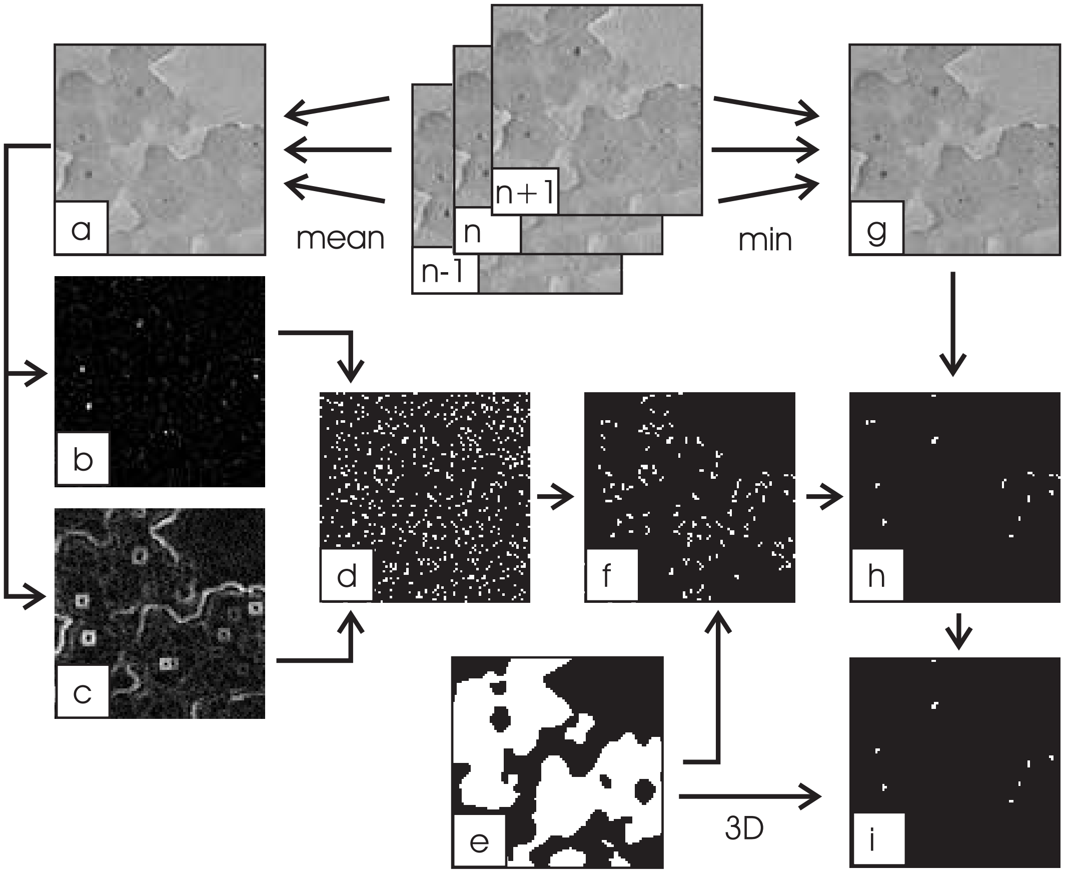

Figure 2.3: Segmentation of the Pd particles in the n$^{\mathrm{th}}$ slice. The image (a) is denoised by averaging three consecutive slices n-1 to n+1. A top-hat filter (b) and an erosion gradient (c) are applied to the image to highlight its local minima. A binary image of the minima (d) is obtained by assigning the value 1 to all pixels where the top-hat is larger than the erosion gradient. This image is then intersected with the binary silica skeleton (e) and all objects smaller than 1 pixel and larger than 25 pixels are removed (f). The contrast of the particles in the grey level image is increased by considering the minimum value of slices n-1 to n+1 (g). Only the objects of image (f) with an intensity in image (g) lower than a given threshold are retained (h). Finally, all 3D objects in image (h) touching the surface of the silica in image (e) are removed (i).

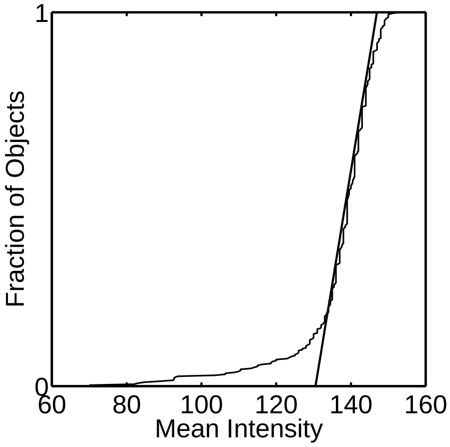

Figure 2.4: Example of cumulative distribution of the objects in Figure 2.3f as a function of their intensity in Figure 2.3g. The intersection of the line with the horizontal axis is the threshold used to discriminate between Pd particles and spurious local minima.

described in Figure 2.2 (Figure 2.3e). Furthermore, the disconnected objects containing only 1 pixel or more than 25 pixels are also removed. The use of these two size criteria is motivated by the observation that the largest visible Pd particles seldom exceed 5 pixels in size, and that 1 pixel is the resolution limit of the image. The resulting image is in Figure 2.3f. The selection of the Pd particles among all the objects of Figure 2.3f is based on the local intensity of the original image, which has not been exploited yet at this stage. As the palladium particles are the darkest objects in the images, their contrast can be enhanced by considering the minimal value of the intensity over the same initial three slices (Figure 2.3g). For each object present in Figure 2.3f, the intensity of the corresponding pixels in image 2.3g is averaged. Figure 4 plots a typical example of cumulative distribution of the number of objects in image 2.3f as a function of their mean intensity in image 2.3g. This distribution clearly evidences two kinds of objects. The most numerous are the bright objects, characterized by a mean intensity about 140, coexisting with a smaller population of darker objects. The intensity threshold that enables discriminating between the two populations is obtained by performing a linear regression on the high intensity part of the distribution and by intersecting the line with the intensity axis. In the particular case of Figure 2.4, the obtained threshold is close to 130. By keeping only the objects of Figure 2.3f with a mean intensity lower than this threshold, one obtains Figure 2.3h. In this

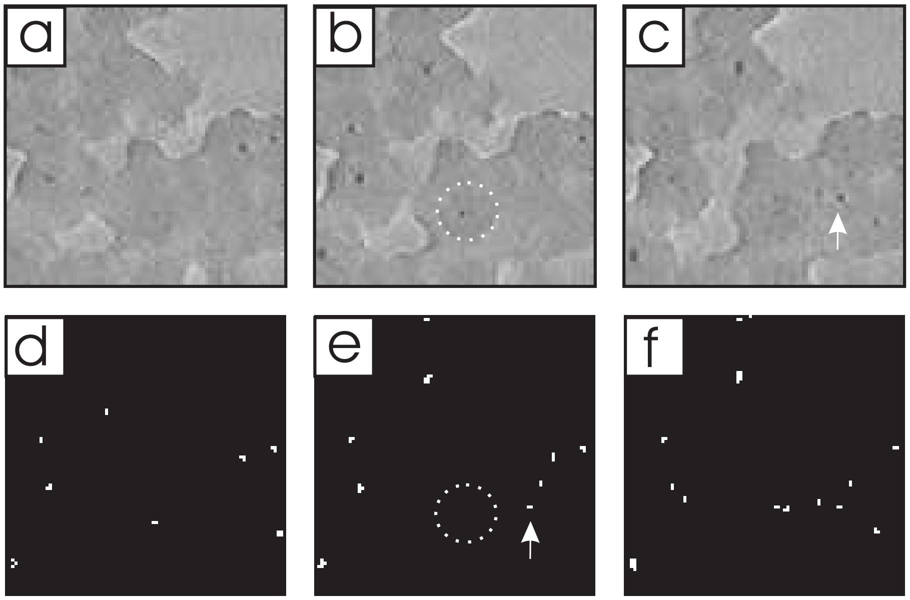

Figure 2.5: Detail of three slices: (a) n-2, (b) n, and (c) n+2 and of their segmented versions (d to f). The two particles circled in (b) are smaller than 1 pixel and are lost during the segmentation. Some particles appear in the binary image but they are visible mostly in a neighbouring slice (arrows in e and c).

image, there are still some spurious objects that correspond to the border of the silica skeleton. Since it is difficult to discriminate between the shadow-like objects (Figure 2.3a) and actual particles, all the objects touching the border are removed. The latter step is actually performed in 3D: all the rough images of the Pd particles (similar to Figure 2.3h) are stacked, and the 3D objects touching the border of the 3D silica skeleton are removed. Figure 2.3i is a slice out of the final 3D binary image of the Pd particles.

In order to better visualize the characteristics of the obtained binary image of the palladium particles, three consecutive slices are displayed in Figure 2.5. The distance between these slices is two pixels, *i.e.* only one slice out of two is represented. The central image, Figure 2.5b, is the same detail of Figure 2.2a as in Figure 2.3. Most Pd particles are correctly segmented. Two very small particles however, circled in Figure 2.5b, are lost during the segmentation procedure. The loss results from the elimination of all objects with a size of 1 pixel (Figures 2.3d to 2.3f). It cannot be avoided without introducing a large number of spurious objects in the images. A given object in Figure 2.5e (indicated by an arrow) seems to be absent in the corresponding grey level image. It is however present in a neighboring slice (Figure 2.5c). It is obvious that the detection of the Pd particles by the proposed methodology is not as accurate as it could have been using high resolution 3DTEM [Weyland & Midgley 2004]. It must, however, be stressed that in the latter case, at most a few ten Pd particles could have been considered, while in the present study about 1000 particles are detected per 3D image, and several such images are used to characterize a single sample. It is merely a matter of strategy to choose either to describe precisely the particles out of a poor sampling, or to coarsely describe the particles out of a sampling that could be statistically representative. The second option was chosen in the present study.

## 2.3 Results

### 2.3.1 Qualitative results

Binary images of the silica skeleton and of the palladium particles, obtained by the method described previously, are represented in Figure 2.6. In this representation, the complex structure of the silica skeleton can be visualized together with the distribution of palladium particles inside the silica. Owing to the morphological complexity of the amorphous silica support, a reliable description of the structure cannot be obtained through simple visual inspection and a statistical approach is required. The purpose of this section is to describe how quantitative morphological characteristics are extracted from the images, in order to better compare the structure of the two analyzed catalysts. For each sample, the analysis is conducted on five tomograms similar to those of Figure 2.6, which accounts for a total of approximately 3000 Pd nanoparticles for each sample.

In sample Pd3.1, the large Pd particles that were previously observed by 2DTEM [Lambert *et al.* 2004d], are also detected by 3DTEM. Figure 2.7 displays such a large particle, the size of which is larger than about 10 nm. From the few similar large particles observed in the tomograms, it seems that they are mainly located at the surface of the silica, contrary to the smallest particles. It should be emphasized that the binary image of Figure 2.7 was segmented by selecting manually the appropriate thresholds. Indeed, the large particles are not detected by the automatic segmentation procedure described in section 2.2.3, as they are not revealed by the top-hat or gradient filter, which highlights only the small features of the images. For these reasons, the large particles are not taken

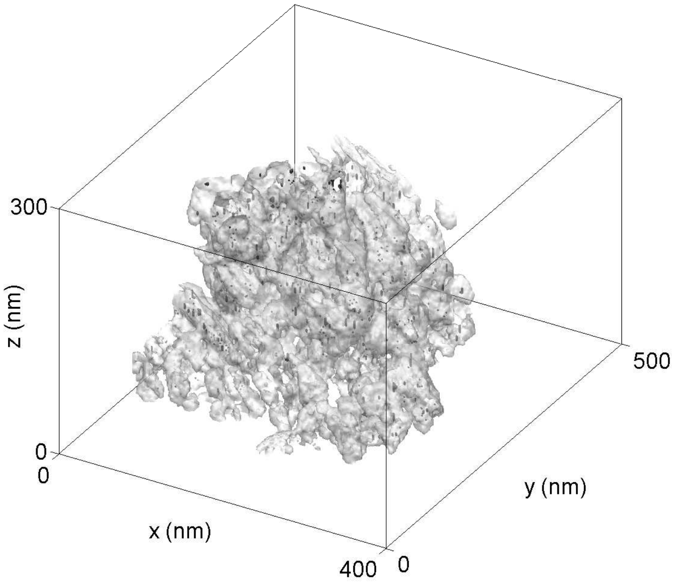
300
z (nm)
0
0
x (nm)
400
0
y (nm)
500

(a) Pd1.1

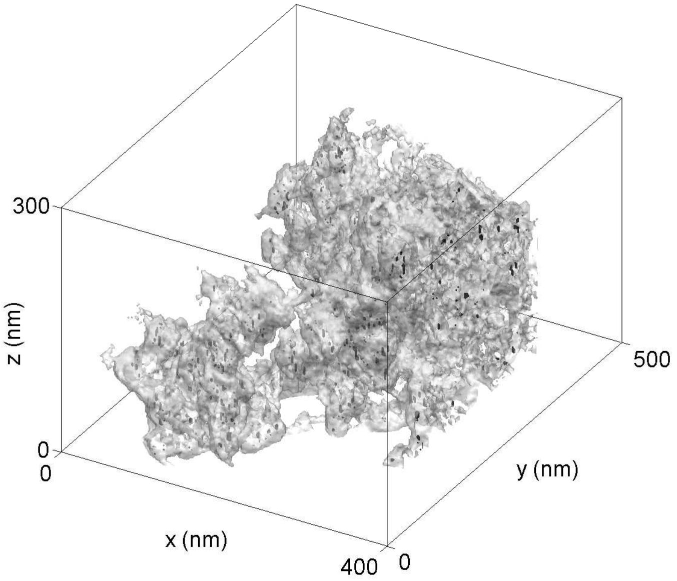
300
z (nm)
0
0
x (nm)
400
0
y (nm)
500

(b) Pd3.1

Figure 2.6: Examples of binary tomograms of the Pd particles and of the silica skeleton of xerogel catalysts (a) Pd1.1 and (b) Pd3.1. The semitransparent bright grey sheet is the surface of the silica skeleton, and the black dots are the Pd particles. Note that the tomograms are cut so that part of the interior of the silica skeleton is visible.

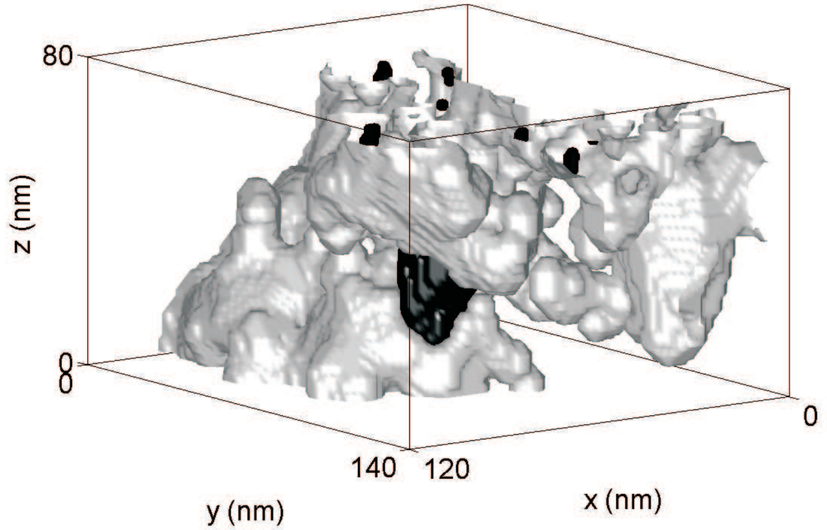

Figure 2.7: Example of a large Pd particle in xerogel catalyst Pd3.1. Contrary to the smallest particles, the large particles are outside the silica skeleton.

into account for the statistical analysis.

As the actual macroscopic metal loading of the samples is known [Lambert *et al.* 2004d], it is useful to compare it with the local metal content of the tomograms. An order of magnitude of the palladium content of the catalysts can be obtained as the ratio of the number of voxels in the Pd image over the number of voxels in the silica image, and correcting this ratio by an estimation of the densities of the two phases. Taking 12 g/cm$^3$ as the density of palladium, and 2 g/cm$^3$ as the density of silica, leads to a Pd loading of *ca* 3 wt.% for both Pd1.1 and Pd3.1. Although the order of magnitude is correct, this value overestimates the loading of Pd1.1 that should be closer to 1 wt.%. It is likely that this error results from an overestimation of the size of the particles. As can be seen on Figures 2.6 and 2.7, most particles have a shape that is elongated in the z direction, which is an artifact due to the missing wedge (in Fourier space, caused by limited angular range) of single axis tomography. Although the same effect is visible for the images of Pd3.1, it seems that the overestimation of the metal loading is not so large for this sample. This issue is related to the presence of undetected very large Pd particles and it is discussed in

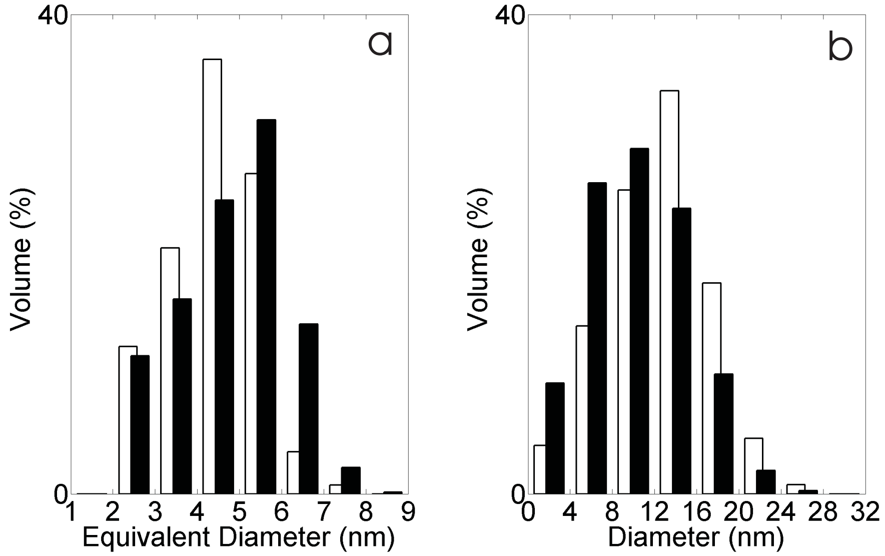

Figure 2.8: Statistical size distributions (a) of the Pd particles and (b) of the silica skeleton. The white bars are for Pd1.1 and the black bars for Pd3.1.

section 2.4.

### 2.3.2 Size distributions

The size of each palladium nanoparticle can be estimated by its equivalent diameter, *i.e.* the diameter of the sphere having the same volume. Figure 2.8a compares the size distribution of the palladium particles of both Pd1.1 and Pd3.1. The particles appear to have very similar sizes in both samples, but slightly larger in Pd3.1 than in Pd1.1, as reported in Table 2.2. This was already found previously using other experimental techniques [Lambert *et al.* 2004b]. Such a standard granulometry cannot be used to characterize the silica skeleton, as it is made of a single object, the size of which would be representative only of the grinding of the sample prior to the microscopic observation. A so-called opening size granulometry is therefore performed [Russ 2002; Soille 1999]. By this technique, any given pixel of the silica skeleton is said to belong to a structure with a size equal to the diameter of the largest sphere containing that pixel and being entirely included within the silica. Figure 2.8b compares the opening size granulometry of samples Pd1.1 and Pd3.1. The most frequent size is slightly smaller for Pd3.1 and the width of the size distribution is almost the same for both samples (Table 2.2).

Table 2.2: Characteristics of xerogel catalysts Pd1.1 and Pd3.1 estimated from image analysis.

| Sample | Pd1.1 | Pd3.1 |
|---|---|---|
| Diameter of Pd particles (nm) | 4.4 ± 1.1 | 4.8 ± 1.3 |
| Diameter of silica skeleton (nm) | 12.5 ± 4.8 | 10.3 ± 4.8 |
| Distance from Pd particle to pore surface (nm) | 7.9 ± 2.3 | 6.5 ± 2.0 |
| Fraction of free surface of the Voronoi cells ( - ) | 0.39 ± 0.19 | 0.41 ± 0.22 |
| Mean distance to neighboring Voronoi cells (nm) | 12.8 ± 5.6 | 14.6 ± 7.0 |
| Number of neighboring Voronoi cells ( - ) | 5.8 ± 2.6 | 6.4 ± 2.9 |

### 2.3.3 Spatial distribution of the Pd particles

An important aspect of metal dispersion that is difficult to address using physicochemical macroscopic methods is the spatial distribution of the metallic particles on or within the support. The qualitative observation of the micrographs suggests that the metallic particles are located inside the silica skeleton (insets of Figure 2.1). A quantitative characterization is obtained by considering the statistical distribution of the distance between the center of gravity of each Pd nanoparticle and the surface of the nearest pore. The distributions are plotted in Figure 2.9. In the case of Pd1.1, the distribution has a maximum at a finite distance from the surface, while for Pd3.1 the maximum is nearer to the silica surface. The cutoff in the distributions at *ca* 4 nm results from the fact that all particles touching the silica surface have been eliminated during the segmentation (see Section 2.2.3 and Figure 2.3h-i). The loss of the particles closest to the silica surface is unavoidable with low resolution tomograms since shadow-like artifacts near the silica surface cannot be discriminated from actual particles. The mean value and standard deviation of the distance between Pd and pore space is reported in Table 2.2.

It is also of interest to assess whether the Pd particles are clustered or uniformly distributed inside the silica. This issue can be addressed by using the concept of influence zones of the particles [Soille 1999], also called generalized Voronoi cells [Ohser & Mücklich 2000]. The approach enables determining which particles are neighbors. Around each Pd particle, an influence zone (or a Voronoi cell) is defined as the locus of all points of the silica that are closer to that particle than to any other. In this way, the entire silica skeleton is

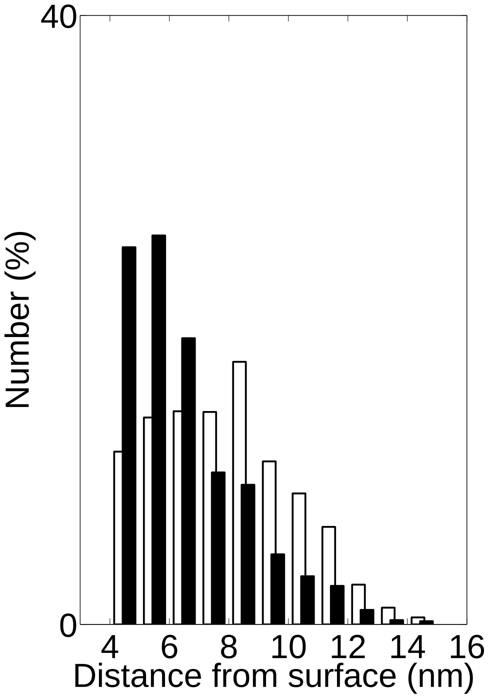

Figure 2.9: Statistical distributions of the distance between the Pd particles and the surface of their nearest pore. The white bars are for Pd1.1 and the black bars for Pd3.1.

split into as many zones as there are Pd particles. In the present case, the influence zones were defined through the use of the geodesic distance [Soille 1999], corresponding to the length of the shortest path inside the silica skeleton between that point and the particle. The resulting tessellation of the silica skeleton is illustrated in Figure 2.10, in which each color corresponds to the zone of influence of a given Pd particle. The main interest of Voronoi tessellation is that it enables the notion of neighborhood to be defined: two Pd particles are called neighbors if their Voronoi cells share a common boundary. It was noticed that each particle has generally two types of neighbors. Indeed, the total surface of a mean Voronoi cell accounts for approximately 1000 voxels. There are a few main neighbors with which the surface of contact is several hundred voxels, and secondary neighbors with which the surface of contact is only a few ten voxels. The latter neighbors are generally also more distant than the former. For the analysis below, the Voronoi cells that share less than 50 voxels are considered as not being neighbors.

Figure 2.11 displays some statistical distributions derived from the Voronoi tessellation

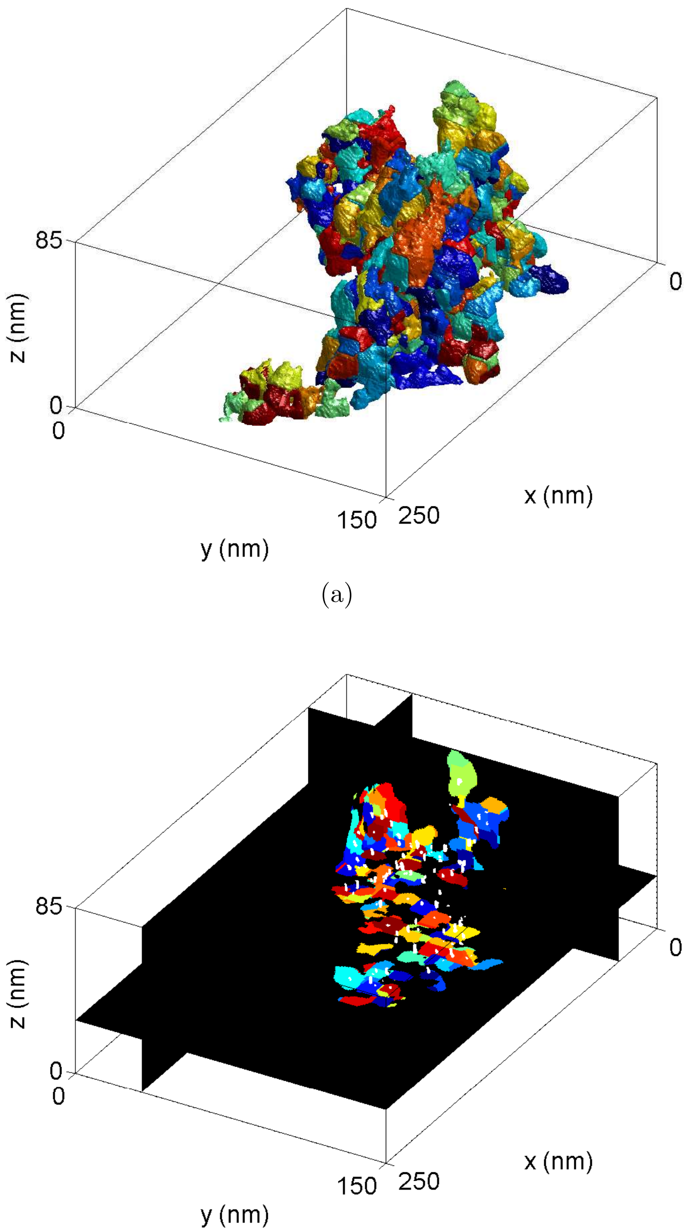
85
z (nm)
0
0
150
y (nm)
250
x (nm)
0
85
z (nm)
0
0
150
y (nm)
250
x (nm)
0

(a)

(b)

Figure 2.10: Example of Voronoi tessellation of the silica skeleton of a fragment of xerogel catalyst Pd1.1; each color corresponds to a zone of influence of a specific Pd particle. Subfigure (a) is the outer surface of the Voronoi cells, and subfigure (b) are three orthogonal cuts inside the same fragment, with the Pd particles in white.

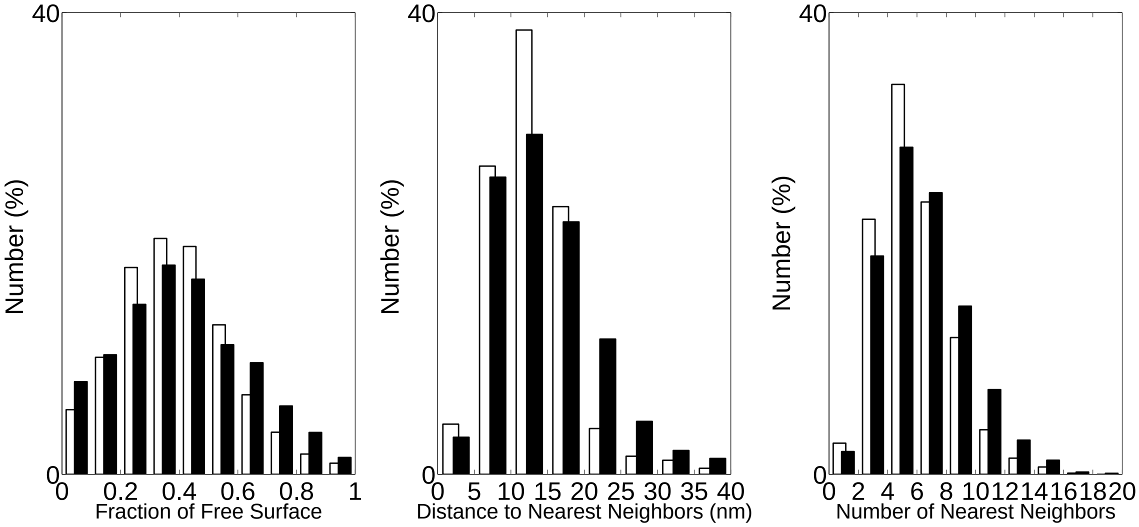

(a) (b) (c)

Figure 2.11: Characteristics of the Voronoi cells: (a) fraction of their surface exposed to pore space, (b) mean distance between neighboring cells, and (d) number of nearest neighbors. The white bars are for Pd1.1 and the black bars for Pd3.1.

of samples Pd1.1 and Pd3.1. A first quantity of interest is the fraction of the surface of each cell that touches the pore space, the rest of the surface being in contact with neighboring cells. Figure 2.11a shows approximately 40% of the surface of most cells is in contact with pore space (see also Table 2.2). This means that the structure is quite open and that there is a free surface in the vicinity of most Pd particles.

The distribution of the mean distance between a particle and all of its neighbors is a parameter that is relevant for the particles' dispersion. For instance, in the case of clustering of the Pd particles, the distribution would be broad because inter-cluster and intra-cluster distances are expected to be very different. One sees from Figure 2.11b and Table 2.2 that the statistical distributions of the mean distance between neighbors are quite narrow, with a standard deviation much smaller than the mean, which means that the particles are well dispersed in both samples. An interesting observation from Table 2.2 is that the mean value of the distance between neighboring particles (12.8 nm and 14.6 nm for Pd1.1 and Pd3.1 respectively) compares reasonably with the size of the silica skeleton estimated by opening granulometry (12.5 nm and 10.3 nm for Pd1.1 and Pd3.1 respectively).

The number of neighbors of each cell is also of interest as it conveys some information on the way in which the particles are spread within the silica (Figure 2.11c). A large number of neighbors is presumably associated with a large heterogeneity of the spatial distribution. As reported in Table 2.2, the mean number of neighbors passes from 5.8 to 6.4 from Pd1.1 to Pd3.1.

## 2.4 Discussion

The main purpose of this study is the determination of the localization of the palladium particles with respect to the silica skeleton, in heterogeneous catalysts synthesized by the cogelation method. Based mainly on 2DTEM observations, it has been suspected for long that the smallest metallic particles in these catalysts are located in the middle of the silica skeleton [Heinrichs *et al.* 1997a;b; Lambert *et al.* 2004a;b;c;d; 2005; Sacco *et al.* 2005]; this conclusion was still doubtful because 2DTEM only gives access to projections of the objects. The present use of electron tomography allows a clear demonstration to be given that indeed the smallest metallic particles are inside the silica skeleton. The present analysis also confirms that the very large particles that appear for high metal loadings are mainly located at the surface of the silica skeleton. It is important to stress that the small Pd particles are fully accessible, despite their being inside the silica skeleton. Nitrogen adsorption-desorption measurements performed on the catalysts reveal a significant amount of very small pores, with a size comparable to that of the nitrogen molecule [Lambert *et al.* 2004b]. Obviously these pores went undetected on the low resolution tomograms used in the present study.

The use of low resolution tomograms enables a statistically representative amount of Pd particles (about 3000 per sample) to be handled. The resolution of the tomograms can be roughly estimated as the ratio of the thickness of the sample to the number of projections used for the reconstruction [Frank 1992]. Considering that the samples are about 100 nm thick and that 140 projections are used (section 2.2.2), the resolution is expected to be of the same order of magnitude as the size of the Pd particles. The difference between the actual size of the particles, as assessed by chemisorption, and the size estimated by image analysis is also of the same order of magnitude, about 2 nm. Even if the size of the particles is close to the resolution, their contrast with the silica is sufficient for their unambiguous localization (see *e.g.* Figure 2.2a). Furthermore, once the particles are localized, the low resolution is not expected to bias the estimation of the distances between themselves or to the surface of the silica skeleton.

For sample Pd1.1, the metal loading estimated from image analysis (about 3 wt.%) overestimates the macroscopic metal loading (1.1 wt.%). It is, however, of the same order of magnitude. This suggests that most of the palladium in that specific sample is under the form of particles located inside the silica. The overestimation results from an artificial elongation of the metallic particles due to the limited angular range in single axis tomography. The overestimation of the size of the Pd particles is also visible when their size estimated by image analysis, 4.4 nm (Table 2.2), is compared with the size estimated from CO chemisorption, 2.7 nm according Lambert *et al.* [2004d]. The same artifact is also present in the tomograms of sample Pd3.1. This is the reason why, despite the presence of very large Pd particles not taken into account in the statistics, the metal loading of that sample is not severely underestimated by image analysis. For that sample, chemisorption predicts a size of 4.6 nm [Lambert *et al.* 2004d], but this value is an average of the size of the smallest particles inside the silica and of the very large particles on its surface.

The present analysis, and most notably the use of Voronoi tessellation, enables clear conclusions to be drawn on the statistical localization of the particles. First, it is particularly interesting to note that the diameter of the silica skeleton and the distance between neighboring palladium particles are almost identical for Pd1.1 (Table 2.2). Second, the distance between the palladium particles and the silica surface is approximately half the aforementioned distance. These two observations show that the Pd particles in Pd1.1 are almost regularly dispersed in the middle of the struts of the silica skeleton. In that respect, the results of the present image analysis are in agreement with the simplified geometrical model of the catalysts proposed by Heinrichs *et al.* [1997b], according to which the Pd particles would be in the centre of silica particles (Figure 1.5 on page 11).

The spatial distribution of the small Pd particles also evolves when the metal loading is increased. As already known from previous studies by Lambert *et al.* [2004b;d], the characteristic size of the silica skeleton decreases when more metal (and consequently more EDAS) is used. As the distance between the particles and the surface of the silica follows the same trend (Table 2.2), it seems that the palladium particles could still be in the middle of the silica skeleton for Pd3.1. It is interesting to note that the detected particles in Pd3.1 are on average more distant from one another than those in Pd1.1, notwithstanding the smaller dimension of the silica skeleton. Also, the mean number of neighbors, as well as the width of the distribution of distance between neighbors, is larger in Pd3.1 than in Pd1.1 (Table 2.2), which suggests that the dispersion of palladium in Pd3.1 is less homogeneous.

## 2.5 Conclusion

The present study shows that cogelled Pd/$SiO_2$ catalysts synthesized from TEOS and EDAS-Pd complexes are characterized by nanometer-sized Pd particles located deep inside the silica skeleton.

The use of digital image analysis enables quantitative conclusions to be drawn from the electron tomograms. For the catalyst with the lowest Pd loading, the Pd particles are optimally dispersed in the middle of the struts of the silica support, with distances between them comparable to the width of the struts. For the sample with a larger metal loading, the same conclusion holds qualitatively for the particles inside the silica, but a significant fraction of the metal seems to be located outside of the silica.

# Chapter 3

# *In situ* SAXS analysis of the formation of cogelled Pd/SiO$_2$ gels

## 3.1 Introduction

Electron tomography coupled with image analysis (Chapter 2) leads to the conclusion that the metal particles in cogelled Pd/SiO$_2$ catalysts are optimally dispersed in the middle of the struts of the silica support, with distances between neighbouring particles comparable with the width of the struts. This unique spatial distribution naturally raises the question of the physicochemical mechanisms that govern the development of such a dispersion of the metal.

Two main questions are addressed in the present chapter. *What are the physicochemical mechanisms that govern the development of the nanometer structure of the Pd/SiO$_2$ catalysts analyzed in Chapter 2? What is the influence of the amount of metal-complexant on the structural development of these materials?*

The present chapter is based on time-resolved Small Angle X-ray Scattering (SAXS). This technique enables to follow *in situ* and in a non invasive way the formation of the gels' structure at the nanometer scale. It is applied in the present work to analyse the formation of Pd/SiO$_2$ gels synthesized by the cogelation method, *i.e.* by incorporating 3-(2-aminoethylamino)propyltrimethoxysilane (EDAS) and a Pd salt in various proportions to a tetraethoxysilane (TEOS)-based alcoholic solution. The SAXS patterns and their time evolution are analysed in the light of models proposed in the literature to describe the formation of similar nanostructured materials. Finally, the structure of the dry xerogel

Table 3.1: Some characteristics of the Pd/SiO$_2$ gels and xerogels.

| | $t_{gel}$ (min) | $l_C^{(i)}$ (nm) | $l_C^{(e)}$ (nm) | $l_{KP}$ (nm) | $\beta$ | $\alpha$ |
|---|---|---|---|---|---|---|
| Pd1.1 | 60 | 23 | 42 | 33 | 1 | 3 |
| Pd3.1 | 76 | 16 | 36 | 17 | 1 | 3 |
| Pd4.5 | 104 | 11 | 36 | 14 | 1 | 3 |

$t_{gel}$: gel time, $l_C^{(i)}$: initial characteristic length of the gels determined from the position of the maximum in Cahn's exponential growth rate $R(q)$, $l_C^{(e)}$: final characteristic length of the gels determined from the final position of the maximum in the SAXS pattern, $l_{KP}$: characteristic size of the xerogels determined from a Kratky-Porod analysis, $\beta$: coarsening exponent defined as $l_C \sim t^{\beta}$, $\alpha$: final value of the asymptotic scattering exponent, defined as $I \sim q^{-\alpha}$.

catalysts is also analysed by SAXS in order to help bridging the gap between the wet and dry materials.

## 3.2 Experimental section

### 3.2.1 Synthesis of the samples and microscopy

The composition of the gels is given in Table 2.1 on page 18; three samples -labelled Pd1.1, Pd3.1 and Pd4.5- are analyzed in the present chapter. The gel time of the solutions, $t_{gel}$ is determined as the moment when the solutions no longer flow when the flask is tilted. This quantity is reported in Table 3.1. Xerogels catalysts are obtained by drying and calcining the gels as described in section 2.2.1 on page 17.

The samples are prepared for the microscopy by grinding them in a mortar into a very fine powder, of which a few mg are dispersed in ethanol. The solution is left to rest for a few minutes, a drop of the supernatant is deposited on a carbon-coated grid, and the ethanol is evaporated.

Figure 3.1 shows transmission electron micrographs of fragments of samples P1.1, Pd3.1 and Pd4.5, after drying. The silica skeleton adopts the morphology of elongated struts with local spherules that are sometimes referred to as *particles*, *e.g.* [Heinrichs *et al.* 1997b; Lambert *et al.* 2004a;d]. Similar structures are encountered in resorcinol/formaldehyde xerogels [Al-Muhtaseb & Ritter 2003] which are sometimes referred to as strings of pearls [Pekala & Schaefer 1993; Schaefer *et al.* 1995]. Globally, for a larger metal loading, the size

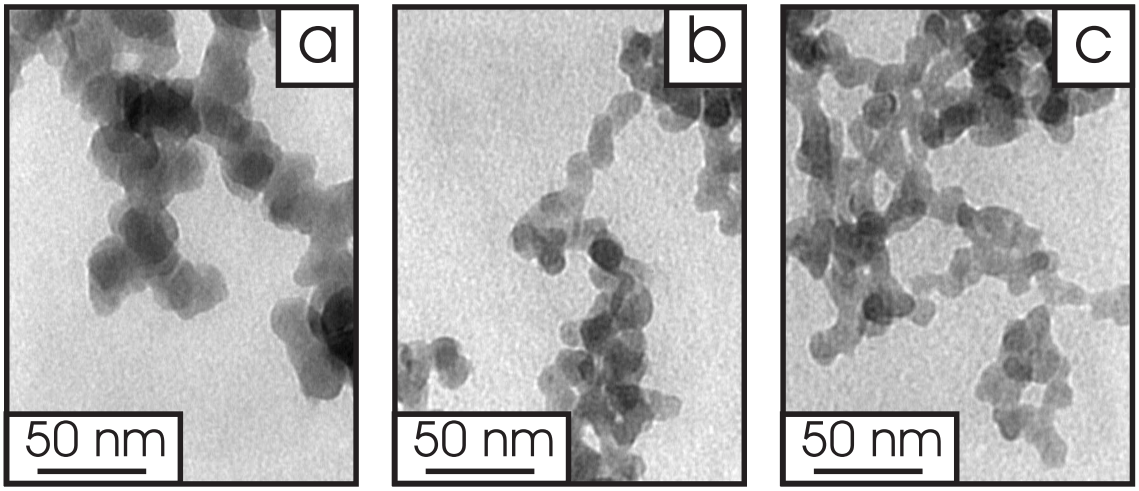

Figure 3.1: Example of TEM micrographs of fragments of non-calcined Pd/$SiO_2$ xerogels (a) Pd1.1, (b) Pd3.1, and (c) Pd4.5.

of the nanostructures becomes smaller, as already noted in Chapter 2 for samples Pd1.1 and 3.1, as well as in previous works by *e.g.* Heinrichs *et al.* [1997b].

The effect of calcining the xerogels is illustrated in Figure 3.2. Qualitatively, calcining leaves the silica skeleton almost unchanged, but leads to the appearance of the Pd particles, that are not visible in the simply dried xerogels.

### 3.2.2 SAXS measurements

Small angle X-ray scattering (SAXS) measurements were performed at DUBBLE, the Dutch-Flemish SRG beam line (BM26B) at the European Synchrotron Radiation Facility (ESRF) in Grenoble, France.

Immediatly after its preparation, a small fraction of the reacting solution is extracted from the flask and placed in a 1.5 mm thick cell with parallel mica windows. Consecutive *in situ* pinhole SAXS patterns are recorded over time spans of 10 s on a quadrant detector placed at 4.25 m from the sample. A correction is made for the detector response and the data are normalized to the intensity of the primary beam measured by an ionization chamber placed upstream from the sample. A second ionization chamber placed downstream from the sample enables the absorption of X-rays by the sample to be determined. The sample holder is coupled to motors that enable it to be moved in the two directions perpen-

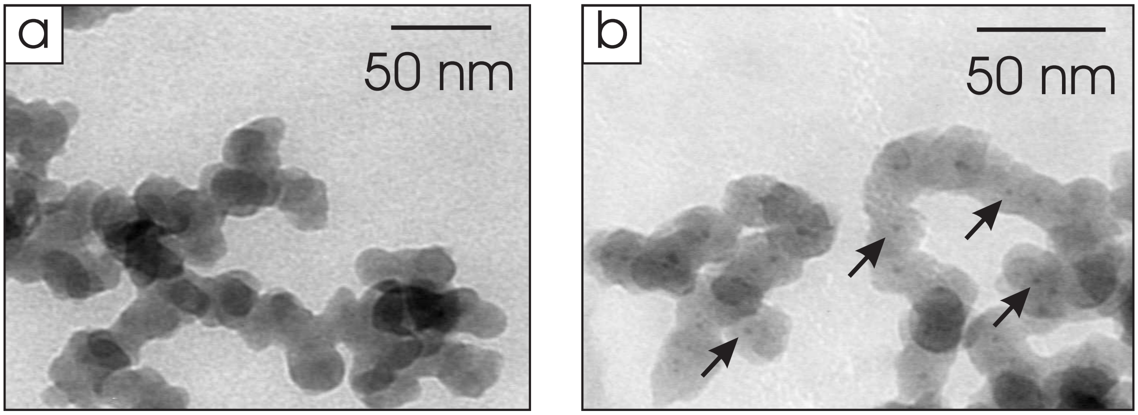

Figure 3.2: Example of TEM micrographs of fragments of Pd/$SiO_2$ xerogel Pd1.1 after (a) drying and (b) drying and calcining. The black dots in figure b are Pd particles that appear during the calcining.

dicular to the beam. The SAXS intensity is expressed as a function of the scattering vector modulus, $q$, which is calibrated using a collagen standard and with $q = 4\pi/\lambda \sin(\theta/2)$, $\lambda$ being the wavelength (set to 1 Å) and $\theta$ the scattering angle. The intensity scattered by the empty sample holder is measured and subtracted from the scattering patterns.

For all patterns, the lowest measured angle corresponds to $q \simeq 0.01$ Å$^{-1}$, and the highest angle to $q \simeq 0.2$ Å$^{-1}$. This means that, in the used configuration, the SAXS probes structures that are smaller than $2\pi/q \simeq 60$ nm and larger than $2\pi/q \simeq 3$ nm.

The SAXS patterns of the xerogels were collected in the Laboratorium voor Macromoleculaire Structuurchemie, at the Katholieke Universiteit Leuven, on a Bruker NanoSTAR apparatus. The device is configured with with the HI-STAR 2D detector at 107 cm from the sample. The 2D patterns are corrected for the detector response, distorsion, and background. Finally the isotropic patterns are averaged azimuthally, and expressed as a function of $q$.

## 3.3 Results

### 3.3.1 Time-resolved SAXS measurements of the gelling solutions

Figure 3.3 plots the scattering patterns $I(q,t)$ as a function of the scattering vector $q$ and reaction time $t$. For all samples, a maximum in the patterns appears early during the reaction. Its intensity progressively increases and its position shifts towards smaller scattering angles with time, as emphasized in each pattern by a circle. The thick black line corresponds to the gel time.

At very low angles ($q < 0.01$ Å$^{-1}$), the scattered intensity seems to increase with decreasing $q$, which suggests the existence of larger structures that are inaccessible with the used experimental set-up. The structural evolution of the gels at the nanometer scale seems to level off towards the end of the experiment for all samples. The moment when the evolution of the SAXS patterns stops apparently coincides with the macroscopic gel point.

The total scattered intensity, the so-called invariant $Q$ [Glatter & Kratky 1982; Schmidt 1995], is defined as

$$Q = \int_0^\infty q^2 I(q) dq \qquad (3.1)$$

Since the scattering pattern is only measured on a limited $q$ interval, the total scattered intensity is estimated by extrapolating the patterns at high $q$ by a Porod law with exponent 4 [Glatter & Kratky 1982]. For all samples, the value of $Q$ initially increases with time (Figure 3.4a). Afterwards, $Q$ either levels off (Pd1.1) or decreases again (Pd3.1 and Pd4.5). At larger times, the total scattered intensity increases again, slightly for Pd1.1 and markedly for Pd3.1. For Pd4.5, the evolution of $Q$ for times larger than about 90 min becomes slightly irregular.

Figure 3.4b displays on logarithmic scales the time evolution of the characteristic length $l_C$ determined from the position of the maximum $q_{max}$ as $l_C = 2\pi/q_{max}$. For every sample there exists a time interval in which the evolution obeys a power law of the type $l_C \sim t^\beta$. Two specific theoretical power laws, with $\beta = 1$ and $\beta = 1/3$ are added to this figure and contribute to the discussion section.

The maximum in $I(q,t)$ is a characteristic of the low-$q$ part of the scattering patterns. As far as the high-$q$ regions are concerned, they are often analyzed by viewing them on a double logarithmic plot, as in Figure 3.5. Apparently, an asymptotic power law of the type $I \sim q^{-\alpha}$ exists at high $q$ towards the end of the experiment; at shorter times no linear region can be identified. Although an asymptotic linear trend in $\log(I)$ against $\log(q)$ is not visible at early reaction times in Figure 3.5, a slope is extracted anyway from its

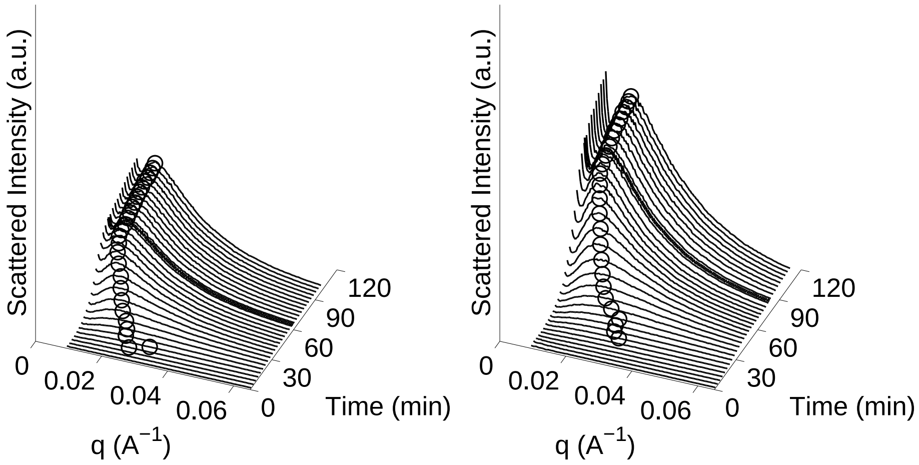

(a) Pd1.1

(b) Pd3.1

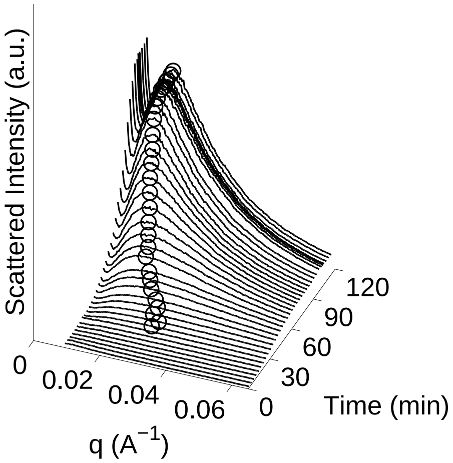

(c) Pd4.5

Figure 3.3: Time-resolved SAXS curves measured on the gelling solutions for samples (a) Pd1.1,(b) Pd3.1 and (c) Pd4.5. The maximum is superimposed with a circle, when it is visible. The thick solid line is the pattern corresponding to the gel point, as assessed by the fact that the solution no longer flows when the vessel is tilted.

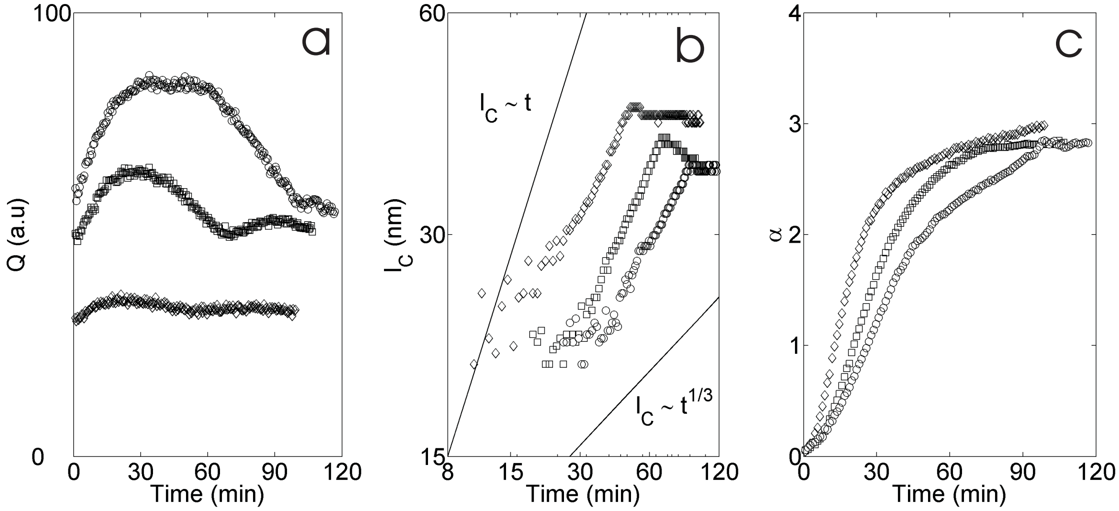

Figure 3.4: Time evolution (a) of the invariant $Q$, (b) of the characteristic length $l_C = 2\pi/q_{max}$, and (c) of the indicative asymptotic exponent $\alpha$, for samples Pd1.1 ($\Diamond$), Pd3.1 ($\Box$) and Pd4.5 ($\bigcirc$). Note the double logarithmic scales in subfigure b.

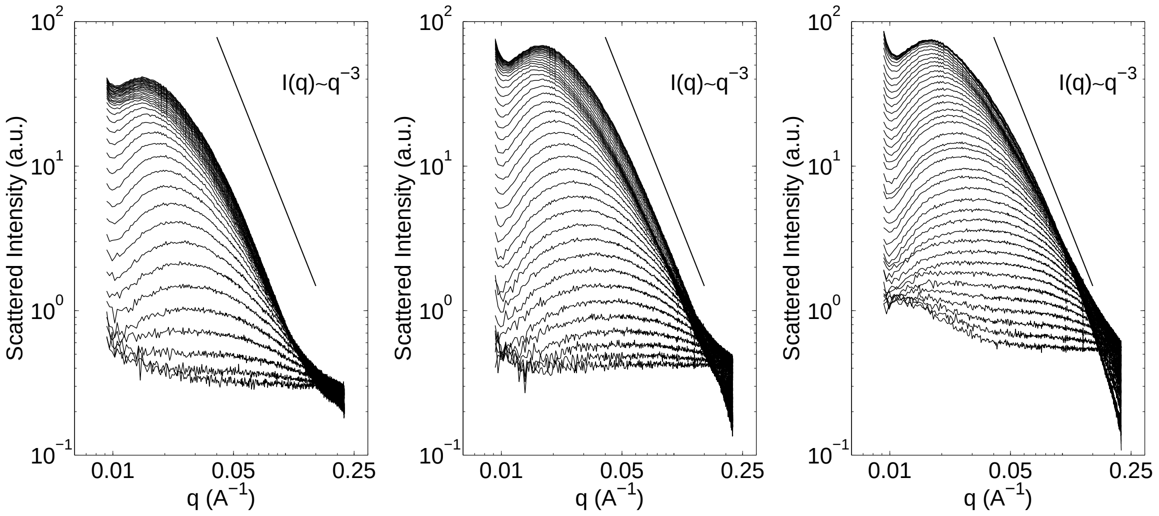

(a) Pd1.1 (b) Pd3.1 (c) Pd4.5

Figure 3.5: Logarithmic representations of the time resolved SAXS measurements of samples (a) Pd1.1, (b) Pd3.1 and (c) Pd4.5. On each graph, the plotted patterns are separated by 2.5 min.

linear portion (Figure 3.4c) to characterize the shape evolution of the scattering patterns. The characteristic exponents $\alpha$ increase continuously with time. A similar observation is reported during the Stöber synthesis of silica colloids; it is attributed to the densification of the scattering structures [Boukari *et al.* 1997]. At the end of the runs $\alpha$ is close to 3 for all EDAS-Pd gels.

### 3.3.2 Photoreduction of Pd by X-rays

The samples undergo a very localized blackening where they are exposed to the X-ray beam. At the end of the measurements, all samples have a thin black line crossing their entire thickness at the exact spot where they were crossed by the beam.

For all samples, the onset of the blackening phenomenon coincides with the gel point. This was checked by moving very slowly the sample holder containing the irradiated reacting solution, at a constant pace of about 15 $\mu$m/min. When the sample is examined at the end of the run, it is translucent where it was hit by the X-rays while it was still liquid, but it is black where it was hit by the X-rays while it was already a gel.

The blackening is accompanied by an increase of the scattered intensity and of the of X-ray absorption by the sample. Figure 3.6 is a 2D scan with the X-ray beam, in the $x$ and $y$ directions, of the portion of sample Pd4.5 that was exposed to the X-rays. During the reaction, the sample was moved in the $y$ direction at a rate of about 15 $\mu$m/min, so that the 4 mm range of the $y$ axis, from 0 mm to +4 mm, corresponds to approximately 2 h of reaction time. The position of the black zone in the sample coincides with the increase of the scattered intensity and of the absorption in Figure 3.6, it occurs at the same time as the gel point.

### 3.3.3 SAXS comparison of Pd/SiO$_2$ gels and xerogels

SAXS is among the few experimental techniques than can be applied to characterize both wet and dry samples [Kaneko 1994]. In order to develop an analysis of the SAXS patterns of the gels that is compatible with what is known about the xerogels, SAXS measurements are performed on those as well.

Figure 3.7 compares the SAXS patterns of the xerogels to the final patterns of the wet

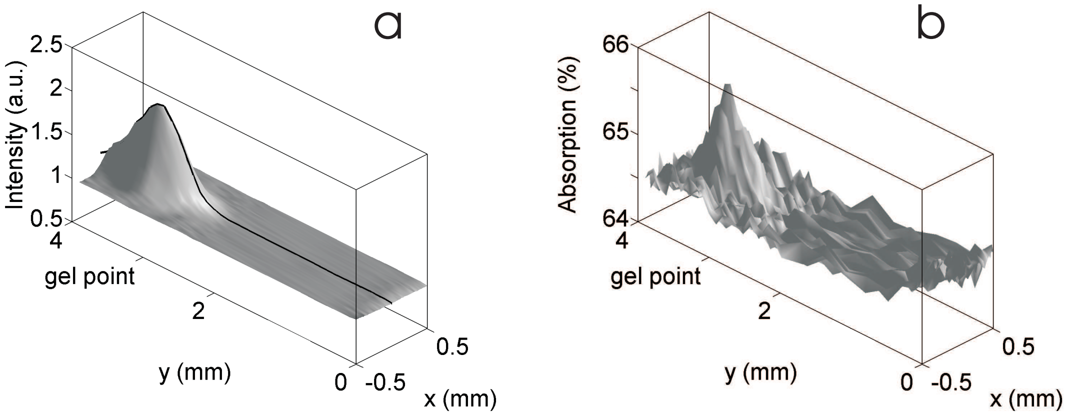

Figure 3.6: 2D scan in the $x$ and $y$ directions of the region of sample Pd4.5 irradiated by X-rays during the reaction: (a) total scattered intensity, and (b) X-ray absorption. During the reaction, the X-ray beam moved regularly from $y = 0$ mm ($t = 0$ min) to $y = 4$ mm ($t \simeq 120$ min), along the black line indicated in subfigure a.

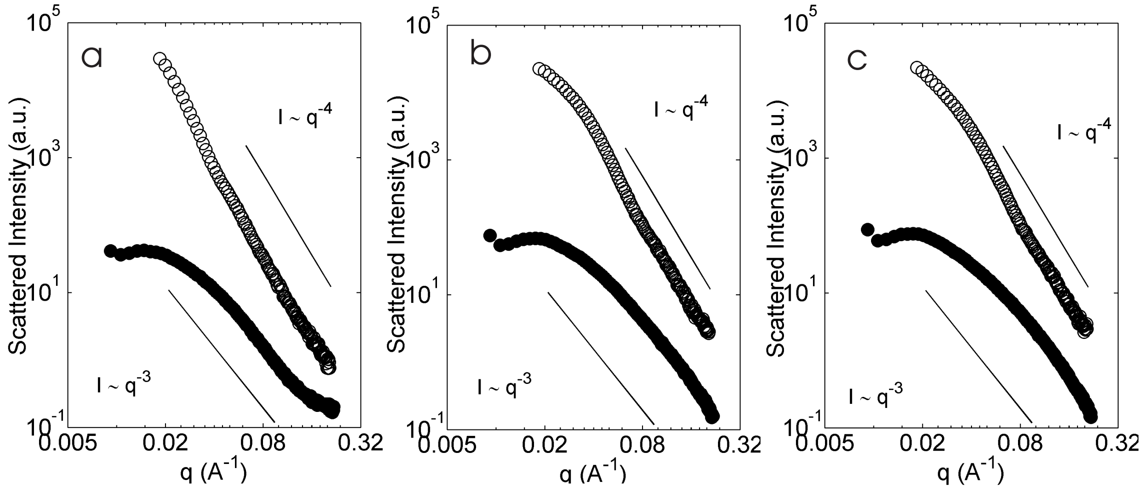

Figure 3.7: Comparison of SAXS patterns measured on the gels (full symbols) and xerogels (open symbols) for samples (a) Pd1.1,(b) Pd3.1 and (c) Pd4.5.

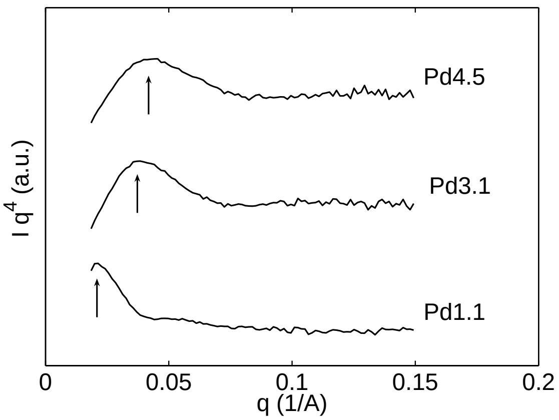

Figure 3.8: Kratky-Porod plots of xerogels Pd1.1, Pd3.1, and Pd4.5, exhibiting a maximum, from the position of which the characteristic length $l_{KP}$ is determined.

gels, on logarithmic scales. The curves of the gels are the same as plotted in Figure 3.3 at the largest time, *i.e.* the approximately 2 h old gels.

The asymptotic power law exponent in the high $q$ range changes from *ca* 3 for the wet to 4 for the xerogels. To extract a characteristic length out of the SAXS patterns of the xerogels, a Kratky-Porod analysis is done [Glatter & Kratky 1982], by which $Iq^4$ is plotted against $q$ (Figure 3.8). A maximum in $Iq^4$ is seen, the position of which $q_{KP}$ is related to a characteristic size by $l_{KP} = 2\pi/q_{KP}$. The values of $l_{KP}$ for Pd1.1, Pd3.1 and Pd4.5 are reported in Table 3.1. The values of $l_{KP}$ are in reasonable agreement with the width of the struts in Figure 3.1.

## 3.4 Discussion

### 3.4.1 General interpretation of the SAXS data

A practical difficulty in analyzing the SAXS patterns comes from the fact that the nanostructure of the samples is triphasic. It comprises (i) the silica, (ii) the pore space filled with the gel's mother liquor, and (iii) the palladium particles. It is therefore *a priori* not obvious how the SAXS data have to be analyzed, and to which phase any particular feature of the SAXS patterns has to be assigned.

From the point of view of X-ray scattering, what characterizes a phase is its electron density. Two phases with the same electron density are indistinguishable by SAXS. It is

Table 3.2: Physical characteristics of the molecules in their pure state.

| | $\rho_m$ (g/cm$^3$) | $M$ (g/mol) | $N_e$ (F/mol) | $V_M$ (cm$^3$/mol) | $\rho$ (F/cm$^3$) |
|---|---|---|---|---|---|
| Water | 1 | 18 | 10 | 18 | 0.55 |
| Ethanol | 0.79 | 46 | 26 | 58 | 0.45 |
| TEOS | 0.93 | 208 | 114 | 223 | 0.51 |
| $SiO_2$ | 2 | 60 | 30 | 30 | 1 |
| Pd | 12 | 103 | 46 | 8.6 | 5.3 |
| EDAS | 1.02 | 222 | 122 | 218 | 0.56 |
| Pd-EDAS complex | - | - | 168 | 226.6 | 0.74 |

$\rho_m$: density, $M$: molar mass, $N_e$: number of electrons in the neutral molecule, $V_M$: molar volume, $\rho$: estimated electron density.

therefore useful to estimate the electron densities of all three phases. The electron density of the molecules involved in the sol-gel reaction can be roughly estimated as $N_e/V_M$, where $N_e$ is the number of electrons in the neutral molecule and $V_M$ is its molar volume (see Table 3.2).

Pd particles are not visible in TEM micrographs of the simply dried xerogels (Figure 3.1). When the xerogels are calcined, however, they become visible, as illustrated in Figure 3.2. This suggests that Pd is not present under a metallic form in the gels, but that it is under the form of an organometallic complex with EDAS. A similar conclusion was reached by Sacco *et al.* [2005] for Pd/$SiO_2$ uncalcined xerogels synthesized with Si-PzPy-Pd complexes (see Table 1.1 on page 9). The latter xerogels exhibit the same catalytic activity for the cyclopropanation of olefins than the PzPy-Pd complexes in homogeneous solution, which suggests that Pd is under the same molecular state in both cases.

In order to estimate the electron density of the Pd-EDAS organometallic complex, it is assumed that the molar volume of the complex is the sum of the volume of the metal and of the complexant molecule. The values are reported in Table 3.2; all the molecules that are likely to be present in the mother liquor -ethanol, water, TEOS, EDAS- have very similar values of $\rho$ close to 0.5. The silica phase in the gel is expected to have an electron density intermediate between that of TEOS and of dense silica, *e.g.* $\rho \simeq 0.75$ F/cm$^3$. The value is very close to the estimated value of the electron density of the EDAS-Pd complex.

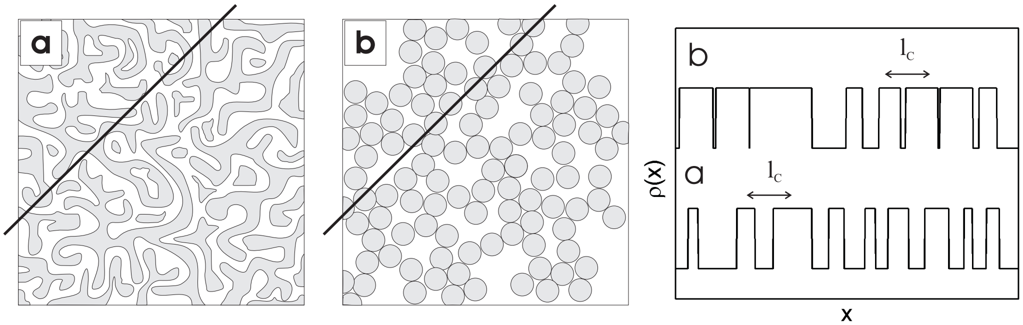

Figure 3.9: Two examples of structures with a characteristic length: (a) a spinodal-like structure and (b) a dense packing of monodisperse spherical particles. When a line is drawn randomly through one of these structures, the variation of the density $\rho$ along the line is almost periodic with periodicity $l_C$. The scattering patterns of these structures would exhibit a maximum at $q \simeq 2\pi/l_C$.

Therefore, from the point of view of the SAXS the Pd-EDAS complex and the partially densified silica are presumably indistinguishable.

The blackening phenomenon reported in section 3.3.2 may be related to the appearance of metallic Pd through the photoreduction of Pd cations under X-ray irradiation. A similar photoreduction phenomenon by X-rays has been reported for several other metal complexes such as Ni [Collison *et al.* 1998] and Mg [Haumann *et al.* 2002]. After the photoreduction process, one expects Pd to have the electron density of the metallic species (5.3 F/cm$^3$ in Table 3.2), by which it should contribute to the X-ray scattering. The blackening of the sample is actually accompanied by an increase of the total scattered intensity (Figure 3.6). Such an increase in $Q$ at the gel time can also be seen in Figure 3.4a, especially for Pd3.1 at about $t = 70$ min. In the case of Pd1.1, the increase is much less pronounced but it must be noted that the sample contains about 3 times less metal than Pd3.1.

In summary, for reaction times lower than the gel time, the SAXS patterns can be analyzed as if they resulted from the scattering of a biphasic system made of (i) the mother liquor phase and (ii) a single silica phase containing the Pd-EDAS complex. This is no longer the case after the gel point, when metallic Pd is present in the samples, with an electron density significantly higher than that of silica.

### 3.4.2 Possibility of several mechanisms

The presence of a maximum in SAXS patterns generally hints at a phase separation phenomenon, and at spinodal-like structures (see Figure 3.9a) [Berk 1987; Guenoun *et al.* 1987]. More generally, a maximum in a SAXS pattern reveals some kind of periodicity in the structure of the scattering system. For a spinodal structure, the periodicity comes from the fact that the alternation of both phases along any given line drawn through the system is almost periodic [Guenoun *et al.* 1987]. The same conclusion holds for a dense packing of non overlapping monodisperse spheres (Figure 3.9b), for which the pseudo-periodicity is the minimal distance between particles corresponding to their diameter [Kotlarchyk & Chen 1983; Mortensen & Pedersen 2001]. It is important to stress that a pseudo-periodicity is not expected for diluted particulate systems in which particles are too distant to interact with one another; no maximum is observed in the scattering patterns of such systems [Glatter & Kratky 1982]. As the presence of a maximum does not allow to discriminate between phase separation on one hand and particles formation on the other hand, both scenarios shall be considered.

Let us consider a nucleation-growth-aggregation scenario. A maximum can appear in SAXS patterns during a colloidal aggregation process. The maximum can result from the regular spacing of monodisperse aggregates [Bibette *et al.* 1992] as can be obtained from a Diffusion Limited Cluster-Cluster Aggregation (DLCCA) [Hasmy & Jullien 1995]. It can also result from the existence of a boundary-layer-like depletion zone surrounding the growing aggregates [Carpineti *et al.* 1995]. In both cases, the scattering curves recorded at different times can be scaled onto a unique curve, and the position of the maximum is the only parameter that changes during the material formation [Carpineti *et al.* 1995; Hasmy & Jullien 1995]. In the present case the shape of the patterns changes with time, as evidenced by the evolution of the asymptotic exponent $\alpha$ in Figure 3.4c; the scaling of the patterns onto a unique curve is therefore impossible.

In the ambit of a particle growth model, the presence of a maximum in the SAXS patterns from the very beginning would mean that the particles already touch each other when they are formed. As the dilution of the reacting solution is rather high, this would mean that the particles are created in clusters[1]. The increase of the intensity and the simultaneous shift of the maximum toward smaller angles would have to be interpreted in this context as an increase of the distance between neighbouring particles as they grow, which the opposite of the expected aggregation process.

Also, in the frame of any aggregation model, gelation is the event with the largest length scale. It cannot occur before the clusters formed by the aggregated particles fill the space and begin to inter-penetrate [Dietler *et al.* 1986; Hasmy & Jullien 1995]. During the process, the evolution begins at the smallest scale, first when the particles themselves are formed, then when two of them meet, and the process ends at largest scale when the largest aggregates touch each other. This is not the case in the present study in which the gel point coincides with the moment when the manometer structure of the gel has just been formed, as assessed by the end of the evolution of the SAXS patterns (see Figure 3.3).

Let us now consider a phase separation scenario. When a maximum appears in the scattering curves of a multicomponent system, this is generally associated with the occurrence of phase separation. For instance, in the case of spinodal decomposition [Bates & Wiltzius 1989; Guenoun *et al.* 1987; Olabisi *et al.* 1979] the existence of a characteristic length, and of a maximum in the scattering patterns, results from the balance between the tendency of like species to segregate and the diffusional limitations that prevent them to separate macroscopically. In the case of phase separation in a polymer network [deGennes 1979a], the tendency of like species to cluster is balanced by the polymer entanglement or by the cross-linking. A phase separation mechanism has been proposed to explain the SAXS curves obtained on resorcinol/formaldehyde gels [Pekala & Schaefer 1993; Schaefer *et al.* 1995], with a string of pearl structure similar to the systems analyzed in the present study (see Figure 3.1). Given the incompatibility of the reported time-resolved measurements with the colloidal aggregation models of gelation, the possibility of a phase separation process is explored.

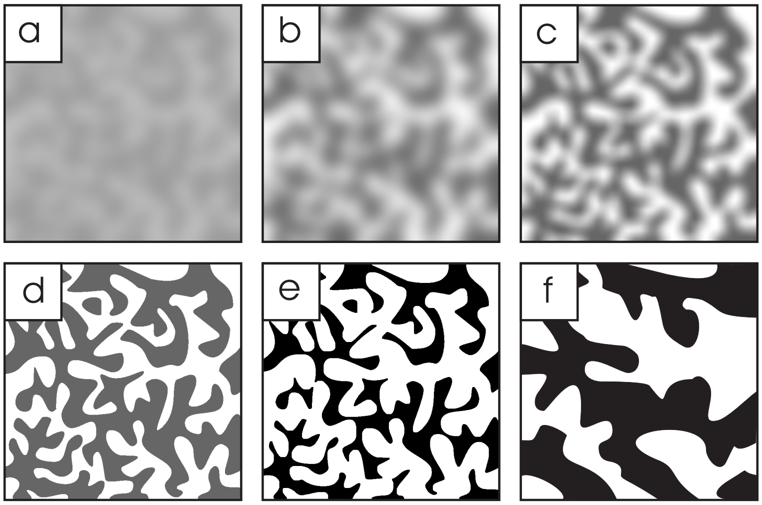

Figure 3.10: Sketch of the three stages of spinodal decomposition (SD): (a) and (b) amplification of the statistical concentration fluctuations during the early stage, (c),(d) and (e) phase differentiation during the intermediate stage and (f) phase coarsening during the late stage. The grey level symbolises the density of the polymer-rich phase.

### 3.4.3 Phase separation model

Figure 3.10 sketches the various possible stages of a reaction induced spinodal-like phase separation [Olabisi *et al.* 1979] of precursor molecules polymerizing in a solvent. At the very beginning of a polymerization-induced phase separation process, the molecules are miscible with the solvent and the solution is homogeneous. The growth of the molecular weight lowers the entropy of mixing of the species, which triggers the phase separation [deGennes 1979b; Ishii & Ryan 2000; Nakanishi 1997]. If demixing occurs *via* a spinodal decomposition (SD) mechanism, some of the spontaneous statistical concentration fluctuations are amplified. Initially, the phases and the concentration gradients have a comparable size, which leads to a wave-like morphology (Figure 3.10a and 3.10b).

The scattering pattern reflects the distribution of concentration wavelengths with a periodicity given by $2\pi/q$ and an attendance given by the corresponding scattered intensity. The favoured wavelength corresponds to the position of the maximum in the scattering patterns. Spatial concentration fluctuations are accurately described by Ornstein-Zernicke theory [Stanley 1971] and produce a power law scattering with exponent $\alpha = 2$. It has been

---

[1] Assuming that the silica phase has a density of 2 g/cm$^3$, the solid fraction of the gels is estimated to be close to 3.5% from the synthesis conditions (Table 2.1 on page 18).

argued that such a power law may appear early during SD [Schaefer *et al.* 1989]. In SD any concentration fluctuation tends to increase resulting in neighbouring regions getting more and more different in terms of polymer concentration (Figure 3.10c). The sharpening of the concentration gradient continues and eventually gives rise to an ideal two-phase system with clear-cut phase boundaries (Figure 3.10d), and a Porod power law with $\alpha = 4$ in the scattering patterns [Glatter & Kratky 1982; Schmidt 1995]. The structural evolution can continue after the appearance of a sharp interface. This can occur either if the polymer-rich phase expels the solvent it contains (microsyneresis, Figure 3.10e) or by the growth of large domains at the expense of smaller ones (Figure 3.10f). The latter coarsening process is reflected in a shift of the scattering maximum towards smaller angles.

The sequence of events characteristic of SD can be followed in the Pd-EDAS-TEOS systems by considering the evolution of the total scattered intensity, also called invariant $Q$, as often done for other polymeric systems [Elwell *et al.* 1996; Ishii & Ryan 2000]. Let the two phases be a silica-rich phase (A) with electron density $\rho_A$, that will eventually contain the percolating network responsible for the gelation, and a solvent-rich phase (B) with electron density $\rho_B$, bound to become the porosity of the final gel. In the case where the two phases are separated by a linear electron density gradient with thickness $E$, theoretical calculations show that the invariant $Q$ can be written as [Vonk 1973]

$$Q = C\left[\phi(1-\phi) - EO_S\right](\rho_A - \rho_B)^2 \tag{3.2}$$

where $C$ is a constant, $\phi$ is the volume fraction of phase B, and $O_S$ is the specific area of the interface. The precise spatial arrangement of the phases has no influence on the value of $Q$.

The expected evolution of the various terms in Equation 3.2 during the three stages of SD is the following. (i) The factor $(\rho_A - \rho_B)^2$ is expected to increase continuously during early and intermediate stages as the phases become more and more dissimilar and reach a constant value by the late stage. (ii) Since the concentration fluctuations in which the spinodal decomposition originates are described by symmetric sinusoidal waves (see figure 3.10a), the corresponding volume fractions of the phases, $\phi$ and $(1-\phi)$ are equal to 0.5 during the early stage. Hence, the factor $\phi(1-\phi)$ is maximal at the onset of phase separation, and phase differentiation (Figures 3.10d and 3.10e) can only lead to a decrease of this factor. (iii) During the intermediate stage, the interface between the two phases becomes more clearly defined, $E$ decreases accordingly with time. The surface tension associated with the interface will drive the coarsening that leads to a decrease of $O_S$ (see figure 3.10f). The latter coarsening process is the only one that continues during the late stage. If $E$ has reduced to zero by that time, coarsening will not affect $Q$ as the term that contains $O_S$ will have vanished. Otherwise, a reduction of $O_S$ with time will result in an increase of $Q$. In summary, all quantities in $Q$ tend to an increase except for the factor $\phi(1-\phi)$. In that respect, it is interesting to note that the calculated values of $Q$ plotted in Figure 3.4a exhibit a maximum. This is particularly clear for Pd3.1 at $t \simeq 30$ min and Pd4.5 at $t \simeq 45$ min. This indicates that $\phi$ shifts away from 0.5 and that, beyond the maximum, phase separation has evolved into the intermediate stage[2]. As discussed in section 3.4.1, the second increase in $Q$ visible in Figure 3.4a is associated with the photoreduction of Pd and it has nothing to do with the phase separation phenomenon.

More evidence for a spinodal type of phase separation can be found in the compatibility of the Cahn-Hilliard theory [Olabisi *et al.* 1979] with the SAXS data during the early stage. According to this theory, the intensity $I(q,t)$ at a given $q$, grows exponentially with time as

$$I(q,t) = I(q,0)\exp(2R(q)t) \tag{3.3}$$

where $R(q)$ is an exponential growth rate. An example of semi-logarithmic plot of scattered intensity *versus* time (sample Pd3.1, $q \simeq 0.05$ Å$^{-1}$) is plotted as an inset to Figure 3.11. Shortly after the beginning of the reaction, a regime where $\log(I)$ grows linearly with time is observed, which allows $R(q)$ to be calculated. The time range during which the exponential growth is observed for all scattering angles generally does not last longer than 10 min. Figure 3.11 displays the estimated growth rate, $R(q)$, as a function of $q$ for all three samples. The curves exhibit a maximum at a position corresponding to the most unstable concentration fluctuations, which determines the length scale of the initial phase separated domains (see Figures 3.10a and 3.10b). The position of the maximum is converted to the initial characteristic length of the domains $l_C^{(i)}$ through the relation $l_C^{(i)} = 2\pi/q$ and is

---

[2] The present analysis neglects the fact that a microsyneretic process (Figure 3.10d to Figure 3.10e) is necessarily accompanied by an increase of the contrast between the two phases, because phase A becomes more concentrated in silica. The increase of $\rho_A - \rho_B$ might well counterbalance the decrease of $\phi(1-\phi)$. This issue is discussed more thoroughly in section 4.4.3 of Chapter 4.

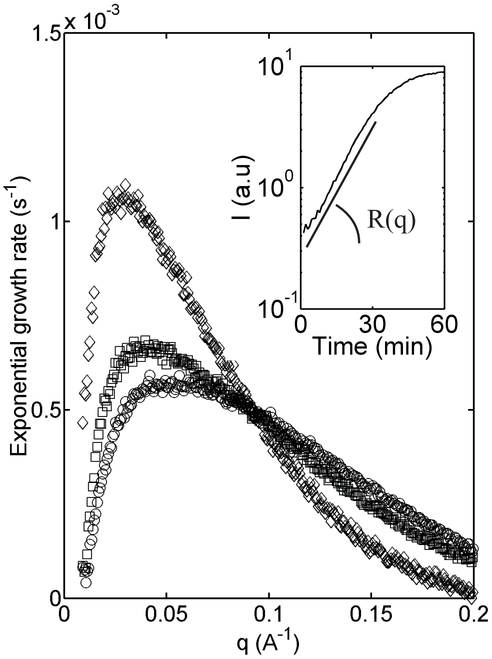

Figure 3.11: Cahn-Hilliard exponential growth rate $R(q)$ of samples Pd1.1 ($\Diamond$), Pd3.1 ($\Box$) and Pd4.5 ($\bigcirc$). The inset shows how $R(q)$ is obtained for Pd3.1 at $q \simeq 0.05$ Å$^{-1}$.

reported in Table 3.1. The initial domains are thinner when a larger amount of EDAS-Pd is used.

The progressive shift of the maximum with time towards smaller angles (Figure 3.4b) is characteristic for the intermediate and late stages of SD; it reflects phase coarsening. Pure late stage behavior (constant $Q$ and increase of $l_C$) cannot be identified for any sample; $Q$ and $l_C$ seem to evolve concomitantly (Figure 3.4). Several physical mechanisms may be responsible for the coarsening. It is customary to distinguish between the diffusive and the hydrodynamic coarsening of the phase separated domains [Siggia 1979; Tanaka 2000]. In the case of a diffusion-controlled growth mechanism, such as the sticking or coalescence of initially distinct domains, one would have $l_C \simeq t^{1/3}$. In a hydrodynamically controlled mechanism, driven for instance by surface tension between the two phases, the coarsening should obey $l_C \simeq t$. From Figure 3.4b the coarsening seems to be controlled by hydrodynamic rather than by diffusional phenomena. This can be taken as an argument in favour of the demixing mechanism above the aggregation model. During the same time, the condensation reactions continue in the silica-rich phase, rendering it more and more viscous and eventually elastic, and the coarsening stops. For the present samples, this event seems to be related to gelation as the movement of the maximum towards smaller angles stops at the macroscopic gel point (Figure 3.3).

The question arises about the chemical mechanism by which increasing the amount of EDAS-Pd results in thinner initial phase separated domains. Due to the presence of methyl groups instead of ethyl groups, EDAS is more rapidly hydrolyzed than TEOS. It may therefore be argued that the overall polymerization rate is increased when a larger amount of EDAS is used. In the frame of chemically induced phase separation, polymerization plays the role of a chemical quench [Kaji *et al.* 1994; Nakanishi 1997]. Increasing the amount of EDAS-Pd speeds up the polymerization, and the phase separation occurs when the molecular weight of the species is larger. Increasing the molecular weight lowers the solubility of the polymeric species, which favors the phase separation, but on the other hand it reduces their mobility. When passing from Pd1.1 to Pd4.5, the rate $R(q)$ at which the phase separation occurs becomes lower (Figure 3.11) and the gel time increases too (Table 3.1). It can therefore be concluded that the dominating effect of increasing the molecular weight is a lowering of the mobility. In this context, it is not surprising that the initial size of the phase separated domains $l_C^{(i)}$ decreases from Pd1.1 to Pd4.5.

## 3.5 Wet and dry samples

The final asymptotic exponent $\alpha$ of the gels is close to 3, which suggests that that the silica-rich phase does not have a well defined surface [Schmidt 1995]. The Porod exponent $\alpha = 4$, characteristic of a structure with clear-cut interfaces [Glatter & Kratky 1982], only appears after the desiccation (Figure 3.7). To assess the influence of drying on the small scale structure of the samples, the characteristic sizes $l_C^{(e)}$ and $l_{KP}$ of the gels and xerogels are compared. Although their ratio does not necessarily correspond to the actual shrinkage of any nanostructure, it can serve as a measure of the shrinkage of the samples at the nanometer scale. It is seen that $l_{KP}/l_C^{(e)}$ decreases from 0.8 to 0.4 from Pd1.1 to Pd4.5 (Table 3.1). This means that the structures obtained with a larger amount of Pd-EDAS undergo a much larger shrinkage during desiccation.

This trend is probably related to the observation that the molecular weight of the phase separating species is larger for larger amounts of EDAS-Pd, as inferred from the kinetics of phase separation. When phase separation occurs at low molecular weight, the species still possess many degrees of freedom, by which the silica-rich phase can reach a high density. This is not possible for already highly reticulated and high molecular weight demixing species. It is therefore not surprising that the extent of shrinkage during desiccation is larger for Pd4.5 than for Pd1.1.

## 3.6 Conclusion

Time-resolved SAXS measurements were performed on a series of silica gels synthesized by co-polymerizing TEOS with 3-(2-aminoethylamino)propyltrimethoxysilane (EDAS) complexing palladium. From the very beginning of the reaction, the SAXS patterns exhibit a maximum that increases in intensity and progressively shifts towards smaller scattering angles with time.

The SAXS patterns cannot be analyzed in terms of a nucleation-growth-aggregation model of gelation, and a phase separation mechanism is proposed instead. The latter scenario is shown to be in agreement with the SAXS patterns. In the frame of the proposed phase separation model, physical reasons are proposed for the observed influence of the amount of EDAS on the nanometric structure of the wet gels and dry xerogel. The amount of EDAS-Pd is shown to control the scale at which the phase separation initially occurs, the coarsening of the phases, and also the amount of shrinkage that the phases undergo at the nanometer scale during desiccation.

# Chapter 4

# Role of the co-reactant during the formation of cogelled silica gels, assessed by *in situ* SAXS

## 4.1 Introduction

The time-resolved SAXS data of Chapter 3 shows that the manometer structure of EDAS-Pd gels forms *via* a reaction induced phase separation. The latter mechanism is different from the colloidal aggregation process often reported in the literature for the formation of similar systems, and previously proposed by Heinrichs *et al.* [1997b] to explain the impact of metal loading on the texture of cogelled xerogel catalysts (see section 1.3.1). The question arises whether the occurrence of phase separation is related to the presence of the metal salt, to the presence of a co-reactant molecule, or to the general conditions of dilution and pH of the silica precursors.

The present chapter therefore aims at gaining insight into the following issues. *What is the mechanism that governs the structure development of pure silica gels under comparable dilution and pH conditions? Does the phase separation process also occur with silica and a co-reactant molecule alone, without any metal? What is the role of the co-reactant molecule? Finally, are the SAXS features that were assigned in Chapter3 to the photoreduction of Pd absent from the patterns of metal free gels, as they should?*

To answer the questions, time-resolved SAXS experiments are carried out on the following series of gels synthesized from TEOS in ethanol: (i) pure silica gels synthesized by the two step Acid/Base method, (ii) gels synthesized with increasing amounts of 3-(2-

aminoethylamino)propyltrimethoxysilane (EDAS) without metal. Previous work by Alié *et al.* [2001] showed that, contrary to EDAS, increasing the amount of 3-aminopropyltriethoxysilane (AES) has only a limited impact on the structure of the final xerogel (see also Section 1.3.2). To check whether such a qualitative difference is related to the very occurrence of phase separation, time-resolved SAXS experiments were carried out also on (iii) gels synthesized with increasing amounts of AES.

## 4.2 Experimental section

### 4.2.1 Synthesis of the samples

#### Two step Acid/Base pure silica gels

Two pure silica gels, AB1 and AB2, are synthesized from tetraethoxysilane (TEOS) in ethanol according to the two step Acid/Base method [Brinker & Scherer 1990; Fidalgo *et al.* 2003]. Compared to the simply base-catalyzed or acid-catalyzed synthesis, this procedure leads to much shorter gel times. The two investigated gels have a dilution and hydrolysis ratios of $D = 10$ and $H = 4$ respectively, corresponding to 10 ethanol and 4 water molecules per TEOS molecule.

Two acidic solutions, A1 and A2, are prepared that contain all the TEOS, 75% of the water, 90% of the ethanol and hydrochloric acid in proportions HCl/TEOS = 0.001 (A1) and HCl/TEOS = 0.003 (A2). The two solutions are aged for 60 min at 60°C.

The rest of ethanol and water is then added to these two solutions, with ammonium in proportion $NH_3$/TEOS = 0.0035 for A1 and $NH_3$/TEOS = 0.0055 for A2. The solutions are aged for another 120 min at 60°C. Gelation occurs after about 60 min for both gels, as reported in Table 4.1. The two samples are referred to hereafter as AB1 and AB2.

#### Gels synthesized with EDAS and AES as co-reactants

Gels are also prepared in ethanol from TEOS, $H_2O$, and $NH_3$ *via* a single-step base-catalyzed hydrolysis and condensation, with 3-(2-aminoethylamino) propyltrimethoxysilane (EDAS) or 3-aminopropyltriethoxysilane (AES) as co-reactants, as described elsewhere [Alié *et al.* 1999; 2001].

Table 4.1: Characteristic sizes and exponents determined from SAXS on the gels.

| | $t_{gel}$ (min) | $l_C^{(i)}$ (nm) | $l_C^{(e)}$ (nm) | $\beta$ | $\alpha$ |
|---|---|---|---|---|---|
| AB1 | 60 | 6 | 11 | 1/2 | 2 |
| AB2 | 60 | 4 | 9 | 1/2 | 2 |
| ET025 | 63 | 23 | 47 | 1 | 2.5 |
| ET04 | 58 | 22 | 43 | 1 | 2.5 |
| ET06 | 54 | 20 | 43 | 1 | 2.5 |
| ET20 | 55 | 13 | 40 | $1-1/3$ | 2 |
| AT05 | 69 | 37 | 42 | 1/3 | 3.5 |
| AT15 | 25 | 29 | 39 | 1/3 | 3.5 |
| AT40 | 10 | <26 | 37 | 1/3 | 3.5 |

$t_{gel}$: gel time, $l_C^{(i)}$: initial characteristic length determined as the initial value of $R_G$ for AB gels and from the position of the maximum in the Cahn amplification factor for EDAS and AES gels, $l_C^{(e)}$: final characteristic length determined as the final value of $R_G$ for AB gels and from the final position of the maximum in the SAXS pattern for EDAS and AES gels, $\beta$: coarsening exponent defined as $l_C \sim t^\beta$, $\alpha$: asymptotic scattering exponent defined as $I \sim q^{-\alpha}$.

To a mix containing the co-reactant, TEOS and half the ethanol, a solution of aqueous $NH_3$ in the remaining ethanol is added under stirring. The stirring is then stopped and the flask is closed. The water solution has a $NH_3$ content of 0.18 mol/l. The hydrolysis and dilution ratios are $H = 4$ and $D = 10$ for all gels. In the present context, the hydrolysis ratio is defined as $H = \mathrm{H_2O/(TEOS{+}3/4\ co\text{-}reactant)}$ where the 3/4 factor comes from the fact that the co-reactants contain only three hydrolyzable groups, while TEOS contains four of them. The dilution ratio is $D = \mathrm{ethanol/(TEOS{+}co\text{-}reactant)}$. The synthesis is performed at room temperature.

Four EDAS-based samples ET025, ET04, ET06 and ET20, corresponding to molecular ratios EDAS/TEOS = 0.025, 0.04, 0.06 and 0.02 respectively, and three AES samples AT05, AT15 and AT40, corresponding to molecular ratios AES/TEOS = 0.05, 0.15 and 0.4 respectively, are analyzed. These are part of a larger series of samples that are further studied in Chapters 5 and 6, the synthesis conditions of which are reported in Table 5.1 on page 82. The observed gel times are reported in Table 4.1.

### 4.2.2 Small Angle X-ray Scattering

Small angle X-ray scattering (SAXS) measurements were performed at DUBBLE, the Dutch-Flemish SRG beam line (BM26B) at the European Synchrotron Radiation Facility (ESRF) in Grenoble, France.

The time-resolved SAXS of EDAS and AES samples is measured at room temperature as was done for the EDAS-Pd samples (see section 3.3.1 of Chapter 3). Immediately after its preparation, a small fraction of the reacting solution is extracted from the flask and placed in a 1.5 mm thick cell with parallel mica windows, with no temperature control. Consecutive pinhole SAXS patterns are recorded over time spans of 10 s on a quadrant detector placed at 4.25 m from the sample.

In the case of Acid/Base samples, the temperature is set to 60°C. A 2D detector placed at 4.25 m from the sample is used, and patterns are recorded over time spans of 30 s. The SAXS patterns are isotropic and they are averaged over all directions to yield 1D patterns.

In all cases, a correction is made for the detector response and the data are normalized to the intensity of the primary beam measured by an ionization chamber placed upstream from the sample. The SAXS intensity is expressed as a function of the scattering vector modulus, $q$, which is calibrated using a collagen standard and with $q = 4\pi/\lambda \sin(\theta/2)$, $\lambda$ being the wavelength (set to 1 Å) and $\theta$ the scattering angle. The intensity scattered by the empty sample holder is measured and subtracted from the scattering patterns [Glatter & Kratky 1982].

For all patterns, the lowest measured angle corresponds to $q \simeq 0.01$ Å$^{-1}$, and the highest angle to $q \simeq 0.2$ Å$^{-1}$. This means that, in the used configuration, the SAXS probes structures that are smaller than about $2\pi/q \simeq 60$ nm and larger than $2\pi/q \simeq 3$ nm.

## 4.3 Results

### 4.3.1 Acid/Base gels

Figure 4.1 reports the time-resolved SAXS patterns measured during the formation of samples AB1 and AB2. During the acid-catalyzed reactions, *i.e.* for $t < 60$ min, a

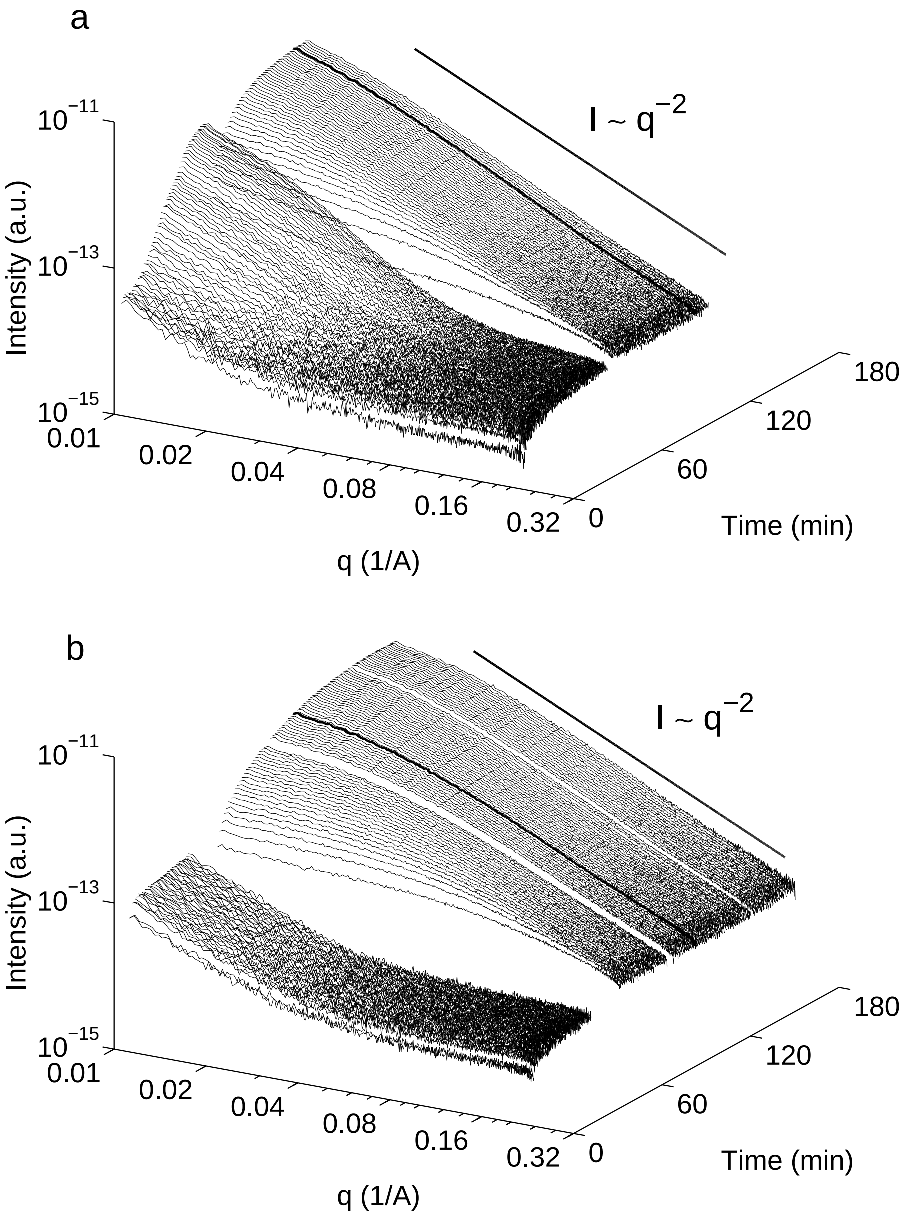

Figure 4.1: Time-resolved SAXS patterns measured during the formation of Acid/Base gels (a) AB1, and (b) AB2, on logarithmic scales. The acid-catalyzed reaction takes place for $t < 60$ min, and the alkaline solution is added at $t = 60$ min. The thick black line corresponds to the gel time.

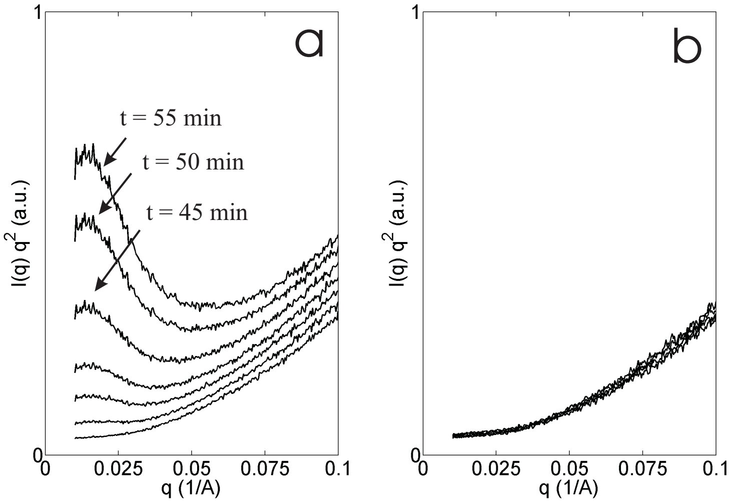

Figure 4.2: Kratky plots of the SAXS patterns measured during the acid catalyzed evolution of samples (a) AB1 and (b) AB2.

marked scattering develops in sample AB1 at low angles, *i.e.* at low $q$, and progressively moves towards larger scattering angles. In the case of AB2, the SAXS patterns exhibit a slight scattering at low angles and no time evolution is observed. Figure 4.2 shows the Kratky plots of the SAXS patterns measured during the acid-catalyzed reaction, obtained by plotting $I(q)q^2$ against $q$ [Burchard 1977; Glatter & Kratky 1982]. At high angles, the Kratky plots increase, which is attributed to the presence of a significant background scattering, corresponding to the low areas of Figure 4.1a. In the case of AB1, a maximum is visible in the Kratky plots, with a position that remains unchanged at $q \simeq 0.015$ Å$^{-1}$. Its intensity increases with reaction time. No maximum is seen for AB2. For this sample a small plateau exists in the Kratky plots at $q < 0.025$ Å$^{-1}$; at higher angles only background scattering is detected.

During the base catalysed reaction (Figure 4.1 for $t > 60$ min) the SAXS patterns are qualitatively different. They exhibit a plateau at small scattering angles and a power law decay at large angles, $I(q) \sim q^{-\alpha}$, with exponent $\alpha = 2$. For increasing reaction times, the asymptotic decay remains unchanged, but its cut-off with the plateau shifts towards smaller scattering angles.

The total scattered intensity, $Q$, defined by equation 3.1 is calculated from the SAXS

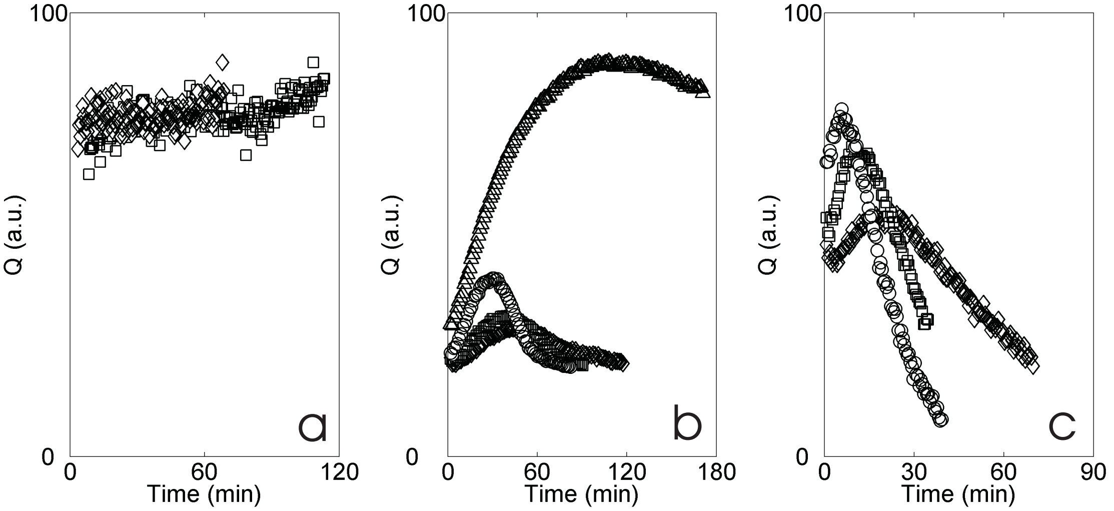

Figure 4.3: Total scattered intensity $Q$ of (a) Acid/Base samples AB1 (◊) and AB2 (□), (b) EDAS samples ET025 (◊), ET04 (□), ET06 (○), and ET20 (Δ), and (c) AES samples AT05 (◊), AT15 (□), AT40 (○).

patterns of the alkaline solution, by extrapolating the patterns with a Porod law with exponent $\alpha = 4$ [Glatter & Kratky 1982]. It appears that $Q$ remains constant during the reaction (Figure 4.3a). The time evolution of the cut-off between the plateau and the power law decay is analysed by fitting the low angle scattering with Guinier's equation [Glatter & Kratky 1982]

$$\ln(I(q)) = \ln(I_0) - \frac{(qR_G)^2}{3} \tag{4.1}$$

where $I_0$ is a constant and $R_G$ is the radius of gyration of the scattering objects, defined as the radius of the sphere having the same moment of inertia as the scattering objects. The estimated values of $R_G$, plotted in Figure 4.4a, show that the growth of the scattering objects obeys $R_G \sim t^\beta$ with $\beta = 1/2$.

The asymptotic exponent $\alpha = 2$ remains constant during the entire base-catalysed reaction, for both samples AB1 and AB2 (Figure 4.5a). Figure 4.6a displays the final SAXS patterns of AB1 and AB2 on double logarithmic scales. The asymptotic exponent is $\alpha = 2$ over almost the entire investigated $q$ range. The value of this exponent is reported in Table 4.1, together with the initial and final values of $R_G$ and with exponent $\beta$.

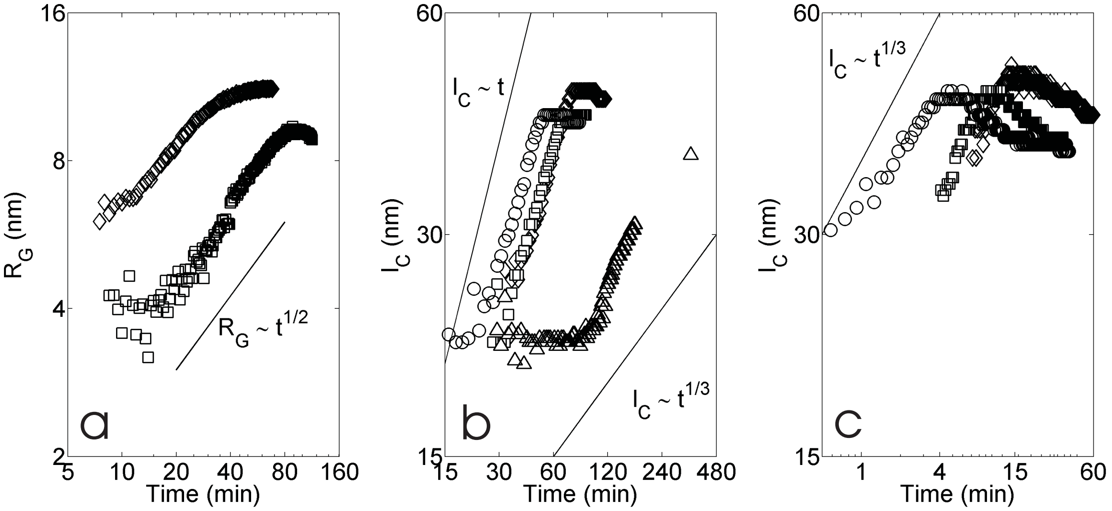

Figure 4.4: Coarsening of the gels' nanometer structure, assessed (a) from the Guinier radius of Acid/Base samples AB1 (◊) and AB2 (□), and from the position of the maximum of the scattered intensity expressed as $l_C = 2\pi/q_{max}$ for (b) EDAS samples ET025 (◊), ET04 (□), ET06 (◯), and ET20 (Δ), and (c) AES samples AT05 (◊), AT15 (□), AT40 (◯).

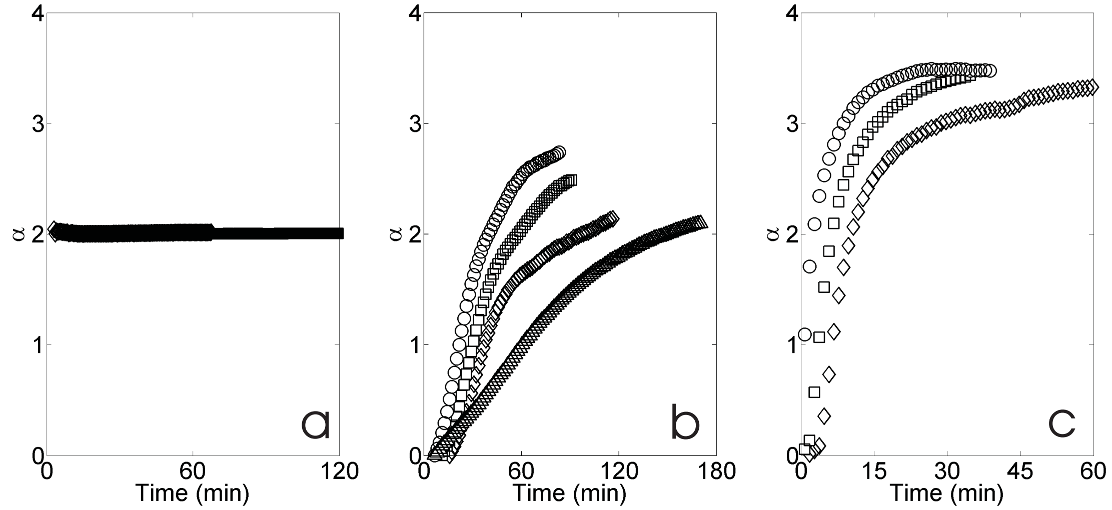

Figure 4.5: Evolution of the asymptotic exponent $\alpha$ of (a) Acid/Base samples AB1 (◊) and AB2 (□), of (b) EDAS samples ET025 (◊), ET04 (□), ET06 (◯), and ET20 (Δ), and of (c) AES samples AT05 (◊), AT15 (□), AT40 (◯).

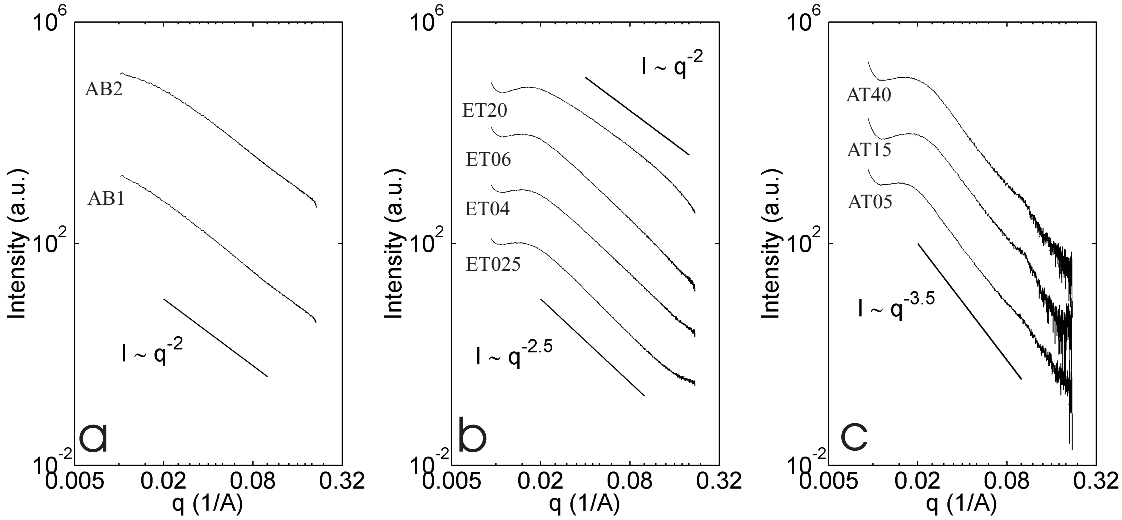

Figure 4.6: Final SAXS patterns on logarithmic scales of (a) Acid/Base gels, of (b) EDAS gels, and of (c) AES gels. The curves are arbitrarily shifted vertically.

### 4.3.2 EDAS and AES gels

Figures 4.7 and 4.8 plot the time-resolved SAXS data collected during the formation of EDAS and AES gels. Globally, the SAXS patterns measured on the samples are very similar to those measured on the samples synthesized with Pd (see Figure 3.3 on page 42), and they are qualitatively different from the Acid/Base samples. They exhibit a maximum since the very beginning of the reaction, with an intensity that increases with time and with a position that progressively shifts towards smaller scattering angles. The phase separation process, proposed to analyze the formation of the EDAS-Pd gels, seems therefore to apply to EDAS and AES gels as well, even without metal.

Increasing the amount of AES results in a lower gel time (Table 4.1) and a more rapid formation of the gels' nanostructure, as is visible from a faster evolution of the SAXS patterns (see Figure 4.8). No such effect of EDAS is seen on the kinetics of the gels' formation. On the contrary, the kinetics of formation of the sample synthesized with the largest amount of EDAS (sample ET20, Figure 4.7d) is markedly slower, as the evolution is far from being completed at the end of the run after 120 min.

Unlike EDAS-Pd samples, for which the evolution of the SAXS patterns ends at the gel point (Figure 3.3 on page 42), the gel time does not seem to coincide with any particular

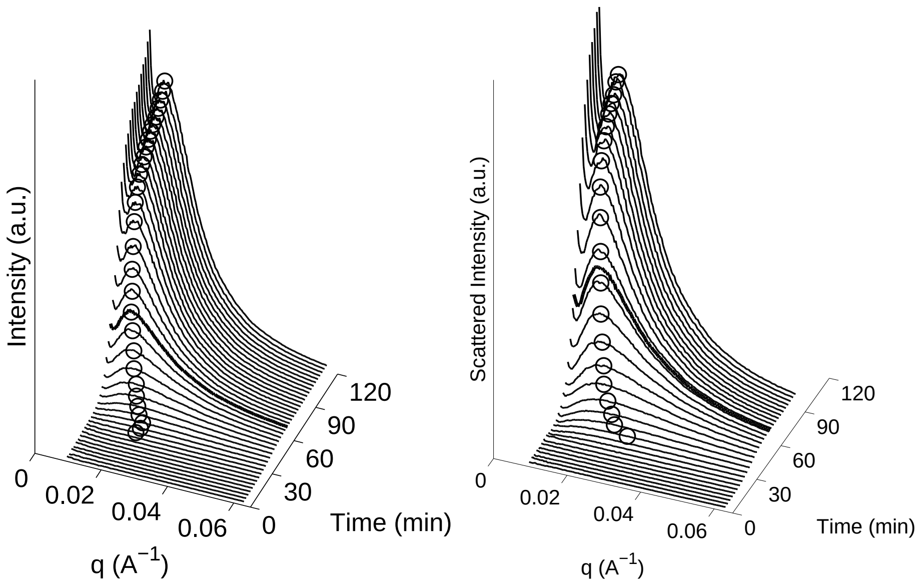

(a) ET025 (b) ET04

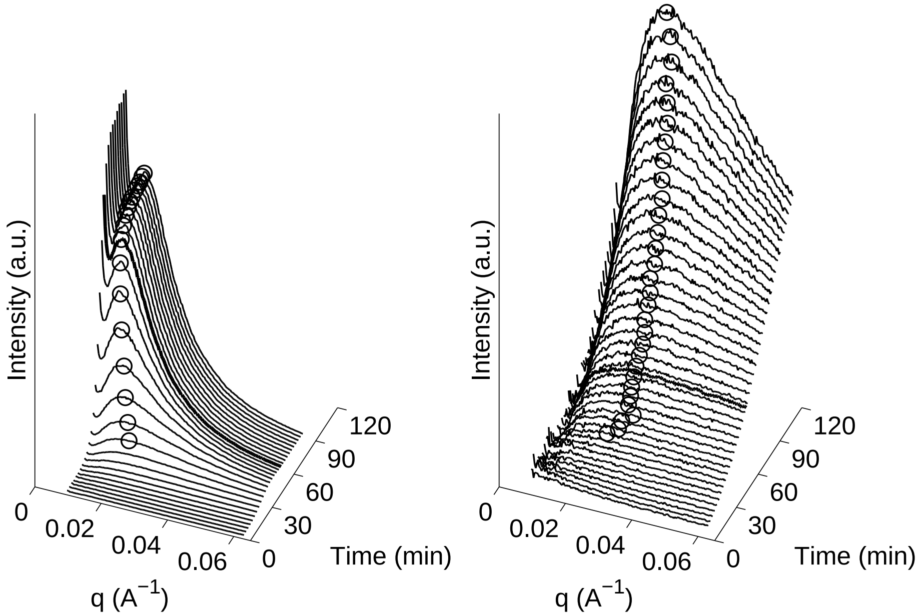

(c) ET06 (d) ET20

Figure 4.7: Time-resolved SAXS patterns of samples (a) ET025, (b) ET04, (c) ET06 and (d) ET20. The circles highlight the position of the maximum in the patterns, and the thick black line corresponds to the gel time.

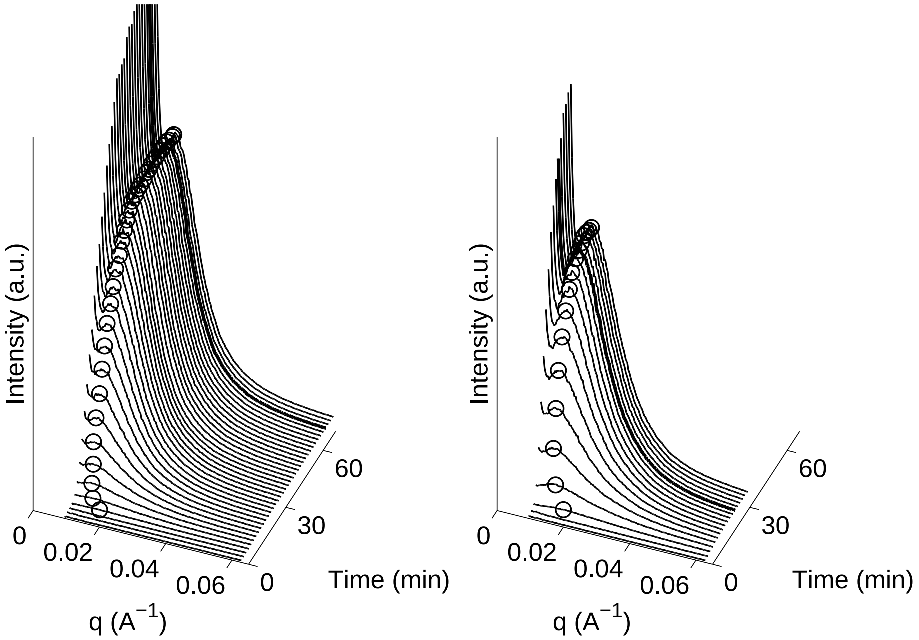

(a) AT05 (b) AT15

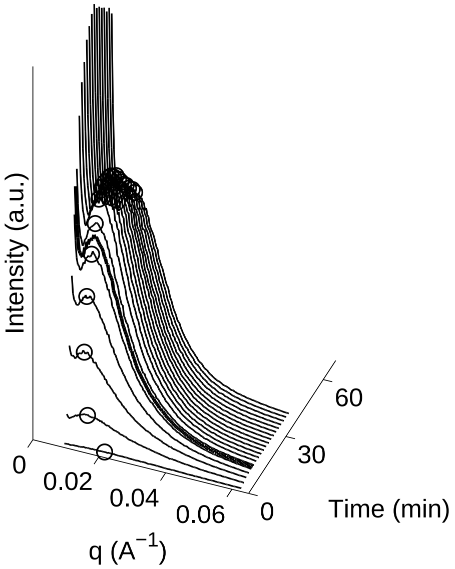

(c) AT40

Figure 4.8: Time-resolved SAXS patterns of samples (a) AT05, (b) AT15 and (c) AT40. The circles highlight the position of the maximum in the patterns, and the thick black line corresponds to the gel time.

event in the case of EDAS and AES gels. For AES gels, it seems that the nanometric evolution ends before the gel point, as is particularly clear for AT05 (Figure 4.8a). The opposite is true for EDAS samples, such as ET20 (Figure 4.7d), for which the gel point occurs when the nanostructure is obviously not formed yet.

Figures 4.3b and 4.3c display the time evolution of the total scattered intensity, $Q$, of EDAS and AES samples, calculated as in section 4.3.1. The total intensity exhibits an increase, followed for most gels by a decrease. The second stepped increase in $Q$ that is reported for EDAS-Pd samples (see Figure 3.4a on page 43) is not observed here. This confirms our previous analysis, according to which the phenomenon is associated with the presence of the Pd.

The position of the maximum in the SAXS patterns is converted to a characteristic length $l_C$ through the relation $l_C = 2\pi/q_{max}$; $l_C$ is plotted as a function of time in Figures 4.4b and 4.4c on logarithmic scales. As discussed in Chapter 3, the movement of the maximum towards smaller scattering angles corresponds to a coarsening of the phase separated domains. In the case of EDAS samples, the coarsening obeys $l_C \sim t$. For AES samples, the time span during which the maximum shifts towards smaller angles does not last more than a few minutes; it seems that the coarsening obeys $l_C \sim t^{1/3}$. An interesting feature shared by all AES samples is that the maximum moves again towards larger angles near the end of the runs (Figure 4.4c). A similar trend is also observed for some EDAS samples (Figure 4.4b) and also for some samples synthesized with Pd (Figure 3.4b on page 43b). The final value of $l_C$, at the end of the runs, is reported in Table 4.1 as $l_C^{(e)}$.

Similarly to EDAS-Pd samples (Figure 3.5), the asymptotic exponent $\alpha$ of the scattered intensity increases continuously with time, as plotted in Figures 4.5b and 4.5c. Figure 4.6 compares on double logarithmic scales the final SAXS patterns of the Acid/Base, EDAS and AES gels. As pointed out in section 4.3.1, the asymptotic exponent of Acid/Base gels is $\alpha = 2$, which corresponds to a fractal structure with dimension $d = 2$, and is typical of many polymeric structures in solution [Daoud & Martin 1989; Richards 1980]. The same exponent is found for the final state of EDAS gel ET20 (Figure 4.6b). Slightly larger fractal dimensions, $d = 2.5$, are obtained at the end of their evolution for all other EDAS samples, which suggests a denser polymeric structure. AES samples in their final state are characterized by a significantly larger exponent $\alpha = 3.5$. Exponents larger than 3 point at

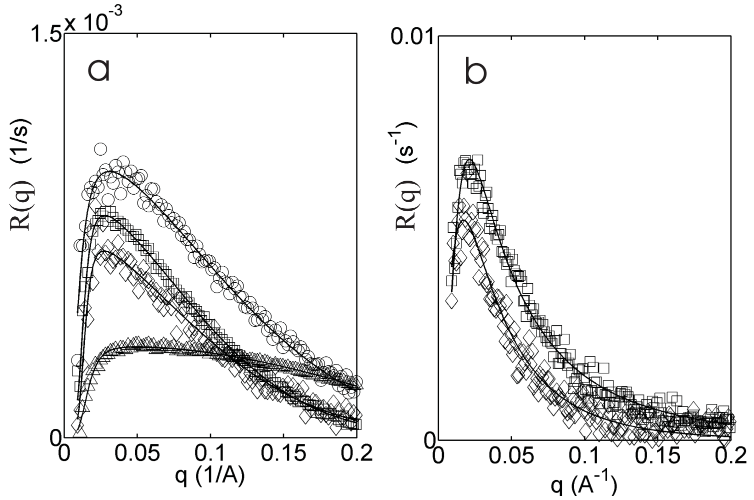

Figure 4.9: Initial exponential growth rates $R(q)$ of the scattered intensity of (a) EDAS samples ET025 (◊), ET04 (□), ET06 (◯), and ET20 (Δ) and of (b) AES samples AT05 (◊), and AT15 (□). Note the different scales in both graphics.

a nanostructure made up by non-porous objects with a fractally rough surface [Schmidt 1995].

At early reaction times, the scattering of EDAS and AES samples is in agreement with Cahn's linear theory [Bates & Wiltzius 1989], as was the case for EDAS-Pd samples (see Section 3.4.3). Accordingly, the intensity scattered at a given angle increases exponentially with time as

$$I(q,t) = I(q,0)\exp(2R(q)t) \tag{4.2}$$

The initial exponential growth rates of the concentration fluctuations $R(q)$ are plotted in Figure 4.9. For all solutions, $R(q)$ exhibits a maximum; its position is converted to the initial characteristic lengths $l_C^{(i)}$ of the phase separated domains, as reported in Table 4.1. In the case of AT40, the evolution is so rapid that $R(q)$ cannot be calculated. For that sample, the value reported as $l_C^{(i)}$ in Table 4.1 is derived from the position of the maximum on the first measured SAXS pattern.

## 4.4 Discussion

### 4.4.1 Pure silica Acid/Base samples

The pure silica samples exhibit qualitatively different scattering patterns in acid and in subsequent alkaline conditions. The evolution of the SAXS patterns measured during the acid-catalyzed evolution of sample AB1 is typical of an increasing branching of polymeric species in solution [Burchard 1977]. This is most clearly visualized through the Kratky plots of Figure 4.2a that show a maximum with an amplitude that increases with time, while its position remains unchanged at $q \simeq 0.015$ Å$^{-1}$. The very existence of a maximum in Kratky plots is typical of branched polymers in solution [Benoît *et al.* 1993; Burchard 1977]. The fact that the position of the maximum remains unchanged means that the size of the macromolecules does not change either [Burchard 1977]. The SAXS patterns measured during the acid-catalyzed evolution of samples AB2 suggest that the polymerization of TEOS in the most acidic condition leads very rapidly to extended and weakly branched macromolecules.

Once the alkaline $NH_3$ solution is added, the evolution of the SAXS patterns changes. The time-resolved SAXS of the base-catalyzed solutions is characterized by a constant power law asymptotic scattering that progressively extends to smaller angles. This is typical of an aggregation of particles smaller than resolution limit of the SAXS, according to the Diffusion-Limited Cluster Cluster Aggregation (DLCCA) process frequently used to model gelation [Brinker & Scherer 1990; Hasmy & Jullien 1995; Viscek 1992]. This is further confirmed by the fact that $\beta = 1/\alpha$, which relation is predicted by the DLCCA model [Hasmy & Jullien 1995; Vollet *et al.* 2001]. A final observation that supports the DLCCA scenario of gelation is that the gel point coincides with the end of the evolution of the SAXS patterns, *i.e.* with the end of the growth of the clusters. Again, this is in agreement with the theory [Hasmy & Jullien 1995] that predicts that gelation occurs when the clusters fill the space and begin to inter-penetrate.

Globally the observations are in agreement with the well documented effect of pH on the hydrolysis and condensation of TEOS [Brinker & Scherer 1990]. Acidic conditions favour the formation of weakly branched structures, and alkaline conditions lead to denser and more branched structures [Schaefer & Keefer 1984]. It is also interesting to note that one passes rapidly from a weakly branched polymeric structure to denser objects smaller than the resolution limit of the SAXS (about 3 nm), as soon as the alkaline solution is added. The rapid collapse of the weakly branched macromolecules into dense particle-like objects is compatible with the observation of the lower miscibility of TEOS and derived oligomers at higher pH [Lee *et al.* 1997; Sefcik & McCormick 1997].

### 4.4.2 EDAS and AES samples

Globally, the time-resolved SAXS patterns of EDAS and AES gels are similar to those measured on EDAS-Pd samples (Chapter 3), and they are qualitatively different from those of pure silica gels. There is evidence of the three typical stages of phase separation [Bates & Wiltzius 1989] for both EDAS and AES gels.

The first stage of phase separation is characterized by the amplification of the most unstable concentration fluctuations [Bates & Wiltzius 1989]. At early reaction time, the SAXS intensity at any angle increases exponentially with time, which is why they can be analyzed using Cahn's theory (Figure 4.9). In all cases, the exponential growth rate $R(q)$ exhibits a maximum with a position that corresponds to the pseudo-periodicity of the most unstable fluctuations (see *e.g.* Figure 3.10b on page 51). In the general case of the separation of two phases, one of which has a viscoelastic and the other a viscous behaviour, the following theoretical relation is predicted [Tanaka 2000]

$$R(q) = Aq^2(1 - \xi^2 q^2)/(1 + \xi_{ve}^2 q^2) \tag{4.3}$$

where $A$ is a constant, $\xi$ is the correlation length, and $\xi_{ve}$ is the so-called viscoelastic length. The latter length $\xi_{ve}$ is the length scale above which the dynamics is dominated by diffusion and below which it is dominated by viscoelastic effects [Brochard & de Gennes 1977; Tanaka 2000]. Equation 4.3 cannot be satisfactorily fitted to the experimental curves of $R(q)$ (Figure 4.9), except for the sample synthesized with the largest amount of EDAS (ET20). As Figure 4.10 shows, the experimental exponential growth rates observed for ET20 compare well with the theoretical prediction of Equation 4.3 with $A = 155$ Å$^2$s$^{-1}$, $\xi = 3.4$ Å, and $\xi_{ve} = 84.4$ Å. The reason why $R(q)$ of the other samples cannot be analyzed by that simple model probably comes from the fact that several physico-chemical phenomena are at work at the same moment, as *e.g.* a chemical reaction, a coarsening

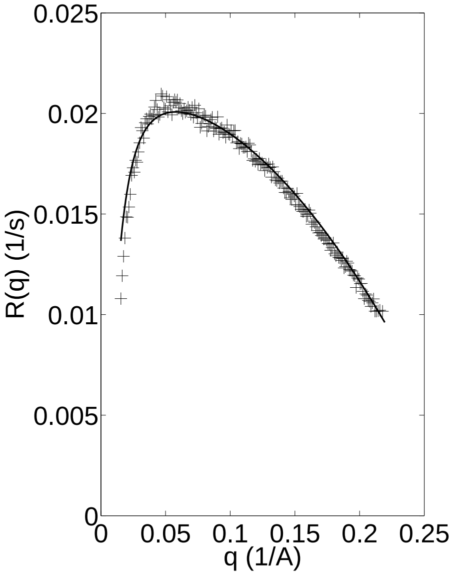

Figure 4.10: Initial exponential growth rates of the scattered intensity of sample ET20 (+) (see Figure 4.9b). The solid line is Equation 4.3 with $A = 155$ Å$^2$s$^{-1}$, $\xi = 3.4$ Å, and $\xi_{ve} = 84.4$ Å.

process, *etc.* In that respect, it is interesting to note that the coarsening of the phases (visible through the shift of the maximum towards smaller angles) begins very early for all samples except for ET20 (see Figure 4.4b).

Phases differentiate during the second stage of phase separation, and their interface becomes clear-cut [Bates & Wiltzius 1989]. In the present case, this can occur through a syneretic process by which the silica-rich phase expels the solvent and loses some of its porosity. As a phase separation phenomenon results from an incompatibility of the silica with the solvent, syneretic processes are expected in the course of the phase separation. As syneresis can occur in gels at the macroscopic scale [Brinker & Scherer 1990], we shall refer hereafter to the process analyzed by SAXS as microsyneresis to distinguish it from macrosyneresis.

The possible ways in which microsyneresis can occur and its impact on the total scattered intensity is discussed in more detail in section 4.4.3. The change of structure that accompanies the compaction of the silica-rich phase can be followed by the evolution of the scattering exponent $\alpha$ in Figure 4.5 [Boukari *et al.* 1997]. In the case of a scattering system with clear-cut interfaces, one would expect an asymptotic exponent of 4 in agreement with

Porod's law [Glatter & Kratky 1982; Schmidt 1995]. Lower values of the exponent can generally be interpreted in terms of fractal structure, either a mass fractal for an exponent lower than 3, or a surface fractal for an exponent between 3 and 4 [Schmidt 1991]. In the present case, the final state of the EDAS gels is characterized by exponents close to 2, hinting at a fractally porous structure. AES gels are characterized by exponents close to 3.5, pointing at homogeneous phases with a fractally rough surface.

The phases coarsen during the late stage of phase separation. This process is accompanied by a shift of the maximum in the SAXS patterns towards smaller angles with time (Figure 4.4). The shift is far less pronounced for AES gels than for EDAS gels, as can also be seen by comparing the differences between $l_C^{(e)}$ and $l_C^{(i)}$ in Table 4.1. During a limited time interval, the coarsening obeys a power law of the type $l_C \sim t^{\beta}$. The specific value of $\beta$ is characteristic of the underlying physico-chemical coarsening mechanism. For all EDAS gels $\beta$ is close to 1, which points at a hydrodynamic coarsening, driven *e.g.* by surface tension effects [Siggia 1979]. For all AES gels, a better agreement could be obtained with $\beta = 1/3$, which would be expected for a diffusional process such as Ostwald ripening, or the coalescence of domains [Siggia 1979]. It must however be noted that this latter exponent is not very precise as the extent of coarsening is very limited. Furthermore, for AES gels the coarsening is followed by an opposite evolution by which the characteristic length decreases again after the end of the coarsening (Figure 4.4c). A possible explanation for this behaviour is given in the next section.

### 4.4.3 Impact of microsyneresis on the total scattered intensity

For all EDAS and AES gels, the increase of the total scattered intensity $Q$ is followed by a decrease at larger reaction times (Figure 4.3). A similar phenomenon is observed for EDAS-Pd gels (Figure 3.4a on page 43). The increase of $Q$ is expected as phase separation leads to the appearance of a structure, but the subsequent lowering is less easily understandable. The lowering of $Q$ is analyzed in terms of microsyneresis in Chapter 3 (Equation 3.2 in section 3.4.3). The analysis is carried out in more depth hereafter. There are different ways in which microsyneresis can occur: they are characterized by different scales (see Figure 4.11) and are expected to have a different effect on the total scattered intensity.

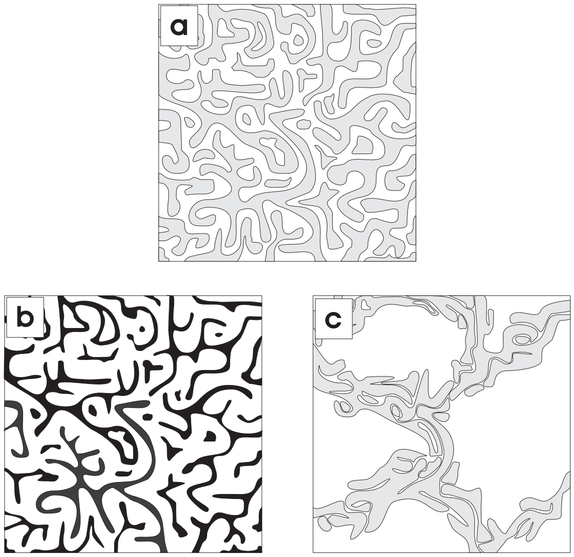

Figure 4.11: Example of two possible microsyneretic processes in a phase separated system. The initial phase separated system (a) can expel its solvent at various scales. Each silica-rich domain can shrink and expel the solvent it contains (b), or the silica-rich domains can get closer to each other, by creating large vacuoles (c). The grey level symbolizes the silica concentration.

**Small scale microsyneresis** could occur, by which the silica-rich domains expel the solvent they contain and therefore concentrate in silica (see Figure 4.11a to b and also Figure 3.10d to e). In the case of a biphasic system with clear-cut interfaces, the term proportional to the thickness of the interface vanishes in Equation 3.2, which leads to [Glatter & Kratky 1982; Schmidt 1991]

$$Q = C(\rho_A - \rho_B)^2 \phi(1 - \phi) \tag{4.4}$$

where $C$ is a constant, $\rho_A$ and $\rho_B$ are the electron densities of the silica-rich and of the solvent-rich phases, and $\phi$ is the volume fraction of the silica-rich phase A. During syneresis, the volume fraction of the silica-rich phase $\phi$ decreases away from its initial value $\phi = 0.5$, characteristic of the initial stage of spinodal phase separation. This is presented in section 3.4.3 as a possible explanation for the lowering of $Q$, since the factor $\phi(1 - \phi)$ is maximum for $\phi = 0.5$. It must however be noted that the silica-rich phase necessarily concentrates in silica during the process: the electron density contrast between the two phases increases. It is therefore not clear at this stage whether this process should actually be accompanied by a decrease of $Q$.

Let us analyze more quantitatively how microsyneresis modifies the electron density contrast between the two phases, $\rho_A - \rho_B$. Let $x_{Si}$ and $x_l$ be the total silica and liquor volume fractions. Liquor stands for the mixture of ethanol, water and low molecular weight silica that fills the pore space of the gels. We shall assume that the liquid that is is expelled from phase A during microsyneresis has the same composition as the liquor. Let $\rho_{Si}$ and $\rho_l$ be the electron densities of the silica and of the liquor. The superscript A and B refer to the two phases: $x_{Si}^A$ refers to the volume of silica in the silica-rich phase, divided by the total volume of the solvent-rich and silica-rich phases. In the same way, $x_l^A$ refers to the volume of liquor in the silica-rich phase, divided by the total volume of the solvent-rich and silica-rich phases. As phase A contains silica and liquor, ones has

$$x_{Si}^A + x_l^A = \phi \tag{4.5}$$

The electron density of phase A can be written as

$$\rho_A = (\rho_{Si} x_{Si}^A + \rho_l x_l^A)/\phi \tag{4.6}$$

As, by definition of the liquor, the solvent-rich phase B is pure liquor, one has $\rho_B = \rho_l$. Taking this into account, the combination of Equations 4.5 and 4.6 leads to the following relation

$$\rho_A - \rho_B = (\rho_{Si} - \rho_l)\frac{x_{Si}^A}{\phi} \tag{4.7}$$

This equation reduces to $\rho_A - \rho_B = \rho_{Si} - \rho_l$ in the particular case where $\phi = x_{Si}^A$, *i.e.* if the silica-rich phase contains no liquor. Introducing Equation 4.7 into Equation 4.4 leads to

$$Q = C(\rho_{Si} - \rho_l)^2 (x_{Si}^A)^2 \frac{1-\phi}{\phi} \tag{4.8}$$

As microsyneresis leaves the amount of polymerized silica in phase A unchanged, $x_{Si}^A$ is a constant during microsyneresis, and the only variable left is $\phi$. As the factor $(1-\phi)/\phi$ increases when $\phi$ decreases, from the two contributions $\phi(1-\phi)$ and of $(\rho_A - \rho_B)^2$ in Equation 4.4, the latter is the leading one. In other words, Equation 4.8 shows that the small scale microsyneresis process represented in Figure 4.11b can only lead to an increase of $Q$.

**Large scale microsyneresis** could occur if the regions of silica-rich phase get closer to each other and expel the solvent between them by creating large vacuole-like solvent-rich zones (see Figure 4.11a to 4.11c). If the solvent-rich zones are large enough to leave the range of sizes measured by the SAXS, they do not contribute to the total scattered intensity. Under those conditions, the expression for $Q$, Equation 4.4, has to be corrected by a factor $\Phi$ corresponding to the volume fraction of the sample that is occupied by the structures that scatter in the measured $q$-range. One can therefore assume

$$Q = C(\rho_A - \rho_B)^2 \phi(1-\phi)\Phi \tag{4.9}$$

where $\phi$ corresponds here to the local volume fraction of the silica-rich phase, within the scattering phase. The microsyneretic process corresponds to a lowering of $\Phi$, that is necessarily accompanied by an increase of $\phi$, because the silica-rich domains get closer to each other. The conservation of the volume of the silica-rich phase implies

$$\phi = \frac{\phi_0}{\Phi} \tag{4.10}$$

where $\phi_0$ is the initial value of $\phi$, *i.e.* when $\Phi = 1$. Introducing this relation in Equation 4.9 leads to

$$Q = C(\rho_A - \rho_B)^2 \phi_0(1 - \frac{\phi_0}{\Phi}) \tag{4.11}$$

where the contrast factor $\rho_A - \rho_B$ is a constant if no small scale microsyneresis occurs at the same time. Therefore, Equation 4.11 predicts that $Q$ decreases during a large scale microsyneresis (*i.e.* for a lowering of $\Phi$), for any value of $\phi_0$.

Large scale microsyneresis could therefore be responsible for the lowering of $Q$. The appearance of large vacuole-like solvent-rich zones, too large to scatter within the measured $q$-range, is indirectly supported by the samples becoming turbid during the formation of the gels. Turbidity is associated with the presence of structures whose size is comparable with the visible light wavelength, *i.e.* a few hundred nm, an issue further discussed in Chapter 5. Another aspect that could be accounted for by a large scale microsyneresis is the shift of the maximum in the SAXS patterns towards larger angles again at the end of the runs (Figure 4.4). The $q$-position of the maximum, $q_{max}$, is roughly related to the distance $l$ between neighboring domains though the approximate relation $l \simeq 2\pi/q_{max}$.

The shift of $q_{max}$ towards larger values could therefore be associated with the silica-rich domains getting closer to each other, by a large scale microsyneresis (Figure 4.11c).

### 4.4.4 AES and EDAS gels

From the preceding sections, it appears that the general mechanism that governs the formation of the nanostructure of both EDAS and AES gels is a phase separation. There is evidence of all the physicochemical events typical of the various stages of phase separation [Bates & Wiltzius 1989], such as the initial amplification of the concentration fluctuations, the phase differentiation, and the phase coarsening. However, the processes occur at the same time, and none of the pure stages of phase separation is observed. The difference in the rate and extent of these events is responsible for the particularities of EDAS and AES gels.

The first significant difference between EDAS and AES gels is the rate of the phase separation, which is faster for AES. This is visible from the values of the initial exponential growth rate $R(q)$ that are 6 times larger for AES than for EDAS (Figure 4.9) as well as from the gel times that are significantly shorter for some AES gels than for EDAS gels (see Table 4.1). From a purely chemical point of view, this observation is puzzling because EDAS is far more prone to hydrolyse and condense than AES, owing to the presence methoxy groups instead of ethoxy groups [Brand *et al.* 1999]. Moreover, increasing the amount of AES further speeds up the formation of the nanostructures as the evolution of $Q$, $l_C$ and of $\alpha$ becomes more rapid (see Figures 4.3c, 4.4c, and 4.5c). This is also surprising because in alkaline conditions, organically substituted alkoxysilanes, such as AES, are less reactive than the non-substituted molecule, such as TEOS [Avnir *et al.* 1998]. A possible explanation for the accelerating effect of AES could be the amine function carried by the molecule (see table 1.1 on page 9) that could catalyse the hydrolysis and condensation reactions [Hüsing *et al.* 1999].

In the case of EDAS samples, the rate of phase separation first increases when increasing the amount of EDAS (from ET025 to ET06) and then drops for larger amounts (ET20), as visible in Figure 4.9a. It seems therefore that the accelerating role of EDAS, expected to speed up the phase separation in the same ways as AES does, is balanced by some antagonistic effect. Taking account of the larger reactivity of EDAS compared to AES and to TEOS, it is likely that the molecular weight and possibly the reticulation of the separating species is larger for large amounts of EDAS. This would explain the importance of viscoelastic effects for the sample synthesized with the largest amount of EDAS (see Figure 4.10).

The succession of events that control the final state of the gel is complex. For instance, the final size $l_C^{(e)}$ of the nanostructures of EDAS and AES gels is determined from the initial scale $l_C^{(i)}$ at which the phases separate, and from the amount of coarsening. From Table 4.1, it is seen that increasing the amount of EDAS or AES results in a significant lowering of the initial size, but also in a significant increase of the amount of coarsening. The most visible difference in the scattering patterns of final EDAS and AES gels is found in the asymptotic exponent (Figure 4.6 and Table 4.1). The values of $\alpha$ point at a fractal-like structure for the silica-rich phase of EDAS gels, and at a non-porous inner structure for the silica-rich phase of AES gels. This contributes to the discussion of the impact of desiccation on the nanostructure of the gels in Chapters 5 and 6.

## 4.5 Conclusion

Time-resolved SAXS shows that gels synthesized with EDAS and AES alone, without any metal, undergo the same reaction-induced phase separation at the nanometer scale as the already analysed EDAS-Pd gels (Chapter 3). For the sake of completeness, the same methodology was applied to analyse the structure development of the well known two-step Acid/Base catalyzed samples. It has been confirmed that the nanostructure formation of these gels follows the aggregation mechanism extensively described in the literature for similar systems.

The various stages of the phase separation in EDAS and AES gels have been interpreted in terms of amplification of the concentration fluctuations, of phase differentiation and microsyneresis, and of phase coarsening. In particular, it has been shown that the lowering of the total scattered intensity, already observed for EDAS-Pd gels, could result from a microsyneretic process that create large vacuole-like structures.

Quite generally, the size of the nanostructures in the final EDAS and AES gels are comparable; increasing the amount of both co-reactants results in a slight decrease of their final characteristic sizes. The most marked difference between EDAS and AES final gels at the investigated length scale is that the inner structure of the silica-rich phase is fractally porous for EDAS gels and non-porous for AES gels.

# Chapter 5

# The structure of AES and EDAS xerogels in the light of phase separation

## 5.1 Introduction

The previous two chapters show that a reaction-induced phase separation is responsible for the nanostructure of the gels synthesized by co-polymerizing TEOS with EDAS-Pd complexes, with EDAS, or with AES. The structure of the gels and the characteristic size of their phases depend on the nature and amount of co-reactant.

In order to understand the relation between the phase separation process and the structure of the final desiccated materials, the textural characterization of AES and EDAS xerogels is carried out in this chapter. Previous characterisation work has been conducted on AES and EDAS xerogels after calcining [Alié *et al.* 1999; 2001], a process that may have modified their texture. The present chapter re-examines the micro- and nano-structure of non calcined AES and EDAS xerogels using independent experimental techniques that probe the samples at various scales.

The following questions are addressed: *Are there remnants of the phase separation process in the nanometer structure of the xerogels? How are the characteristics of the various gels affected by the desiccation?*

The micro- and nano-structures of the two series of xerogels are analyzed using nitrogen adsorption measurements, SAXS, and electron microscopy coupled with digital image analysis. The impact of the co-reactant on the texture of the xerogels at various scales is assessed. The results are discussed in the light of the time-resolved SAXS.

## 5.2 Experimental section

### 5.2.1 Synthesis of the samples

The gels are synthesized as described in section 4.2 on page 58. The gels are aged for 1 week at 60°C. Next, the flasks are opened and put in a drying oven heated at 60°C where, over a period of a week, the pressure is progressively lowered from atmospheric to about 1000 Pa, and the temperature raised to 150°C. Note that the samples are not calcined.

Six AES-based and six EDAS-based samples are studied in this paper, with increasing amounts of co-reactant; their names and compositions are reported in Table 5.1. During the reaction, the samples become turbid and eventually gelify; the time for turbidity and the gel time of the samples are reported in the same table. The gel time is determined as the moment when the solution no longer flows when the flask is tilted. The liquid to gel transition of the samples is generally abrupt so that the gel times reported in Table 5.1 are reliable; the transition from transparent to turbid is quite progressive and the reported turbidity times must be considered as an indication.

At the gel time, AES gels are white and opaque, and EDAS gels are milky but translucent, with a slight increase in translucency when more EDAS is used. Sample AT025 did never gelify, even over a period of months, and it resulted in a stable white liquid. In their final dry state, the xerogels are all white and opaque, except samples ET10, ET15 and ET20. The latter are yellow; samples ET15 and ET20 are also translucent.

### 5.2.2 Physical characterization of the samples

The bulk densities of the xerogels, $\rho_b$, are measured by mercury pycnometry, *i.e.* from an independent measurement of the mass and volume of a monolithic sample. The skeletal densities of the samples, $\rho_s$, are measured on a Micromeritics AccuPyc 1330 Helium pycnometer. The specific porous volume, is estimated as $V_p = 1/\rho_b - 1/\rho_s$. The porosity is estimated as $\epsilon = 1 - \rho_b/\rho_s$.

Nitrogen adsorption-desorption isotherms are measured at 77 K on a Carlo Erba Sorptomatic 1990 volumetric device, after outgasing the samples overnight at room temperature

Table 5.1: Synthesis of the samples.

|  | Co-reactant | $D$ | $H$ | Co-reactant/TEOS | $t_{turbidity}$ (min) | $t_{gel}$ (min) |
|---|---|---|---|---|---|---|
| AT025 | AES | 10 | 4 | 0.025 | $< 60$ | $>$ months |
| AT05 | AES | 10 | 4 | 0.05 | 27 | 95 |
| AT10 | AES | 10 | 4 | 0.10 | 21 | 35 |
| AT25 | AES | 10 | 4 | 0.25 | 13 | 21 |
| AT40 | AES | 10 | 4 | 0.40 | 9 | 15 |
| ET025 | EDAS | 10 | 4 | 0.025 | 38 | 77 |
| ET04 | EDAS | 10 | 4 | 0.04 | 60 | 71 |
| ET06 | EDAS | 10 | 4 | 0.06 | 60 | 69 |
| ET10 | EDAS | 10 | 4 | 0.10 | 60 | 66 |
| ET15 | EDAS | 10 | 4 | 0.15 | 60 | 66 |
| ET20 | EDAS | 10 | 4 | 0.20 | 55 | 70 |

Co-reactant : nature of the co-reactant, $D$: dilution molar ratio Ethanol/(TEOS + co-reactant), $H$: hydrolysis molar ratio Water/(TEOS+3/4 co-reactant), Co-reactant/TEOS: molar ratio, $t_{turbidity}$ : time elapsed from the mixing of water with the silica precursors to the moment when to the solution loses its transparency, $t_{gel}$: time elapsed from the mixing of water with the silica precursors to the moment when to the solution no longer flows.

at a pressure lower than $10^{-4}$ Pa. The data are analyzed using standard techniques [Lecloux 1981]. The porous volume $V_{N2}$ is estimated from the desorption branch as the amount of nitrogen sorbed at $p/p_0 = 0.98$. The data are also fitted with the BET model; the specific surface area $S_{BET}$ and the BET constant $C_{BET}$ are estimated. Following the IUPAC recommendations [Rouquerol *et al.* 1994] a pore of width $w$ is called a micropore if $w < 2$ nm, a mesopore if 2 nm $< w <$ 50 nm, and a macropore if $w >$ 50 nm.

Small Angle X-ray scattering patterns were collected in the Laboratorium voor Macromoleculaire Structuurchemie, at the Katholieke Universiteit Leuven, on a Bruker NanoSTAR apparatus. The apparatus is configured with the HI-STAR 2D detector at 107 cm from the sample. The 2D patterns are corrected for the detector response, distortions due to the use of a flat detector, and background. Finally the isotropic patterns are averaged azimuthally and expressed as the scattered intensity as a function of the scattering vector $q = 4\pi/\lambda \sin(\theta/2)$, $\lambda$ being the wavelength (1.54 Å), and $\theta$ being the scattering angle.

### 5.2.3 Microscopy and image analysis

Two different methods are used to prepare the xerogels for observation on a Philips CM100 transmission electron microscope operated at 100 kV.

**Preparation A**: The xerogels are first embedded in an epoxy resin that polymerizes inside its pores, approximately 60 nm thick slices are cut out of the embedded xerogel and deposited on the microscopy grid.

**Preparation B**: The xerogels are ground in a mortar into a very fine powder, of which a few mg are are dispersed in ethanol, and the suspension is left a few minutes under ultrasonic agitation. The dispersion is left to rest for another few minutes, a drop of the supernatant is deposited on a carbon-coated microscopy grid and the ethanol is evaporated.

The images obtained from both types of preparation are analyzed with standard techniques of image analysis, using the Matlab® software and its image processing toolbox. All analyses presented are an average of measurements performed on at least 15 micrographs.

## 5.3 Results

### 5.3.1 TEM and image analysis

Figures 5.1 and 5.2 show examples of the micrographs obtained from preparations A and B on the first and last samples of AES and EDAS series. With preparation A the large scale structure of the xerogels is accessible, characterized by lengths of a few hundreds of nanometers, whereas with preparation B (insets) objects with typical size of a few ten nanometers are visible.

The large scale structure of the samples, as visible from A micrographs consist in large empty spaces separated by filamentous structures. In the case of xerogels synthesized with a large amount of EDAS (Figure 5.2b) no clear feature can be detected, because the structures are smaller than the thickness of the slice (about 60 nm).

The insets of Figures 5.1 and 5.2 are B micrographs, obtained by grinding the samples. The observed fragments of the xerogels correspond to the elongated structures previously described; they can now be observed without overlap. Because of local spherules in these structures (*e.g.* Figure 5.1a) they are sometimes referred to as “strings of pearls” in the

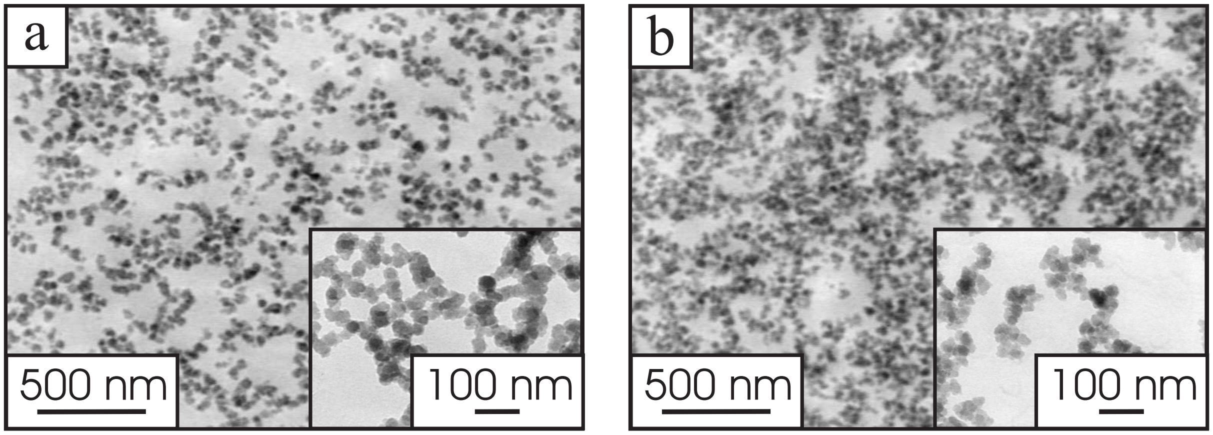
a
500 nm
100 nm
b
500 nm
100 nm

Figure 5.1: Typical TEM micrographs of AES xerogels (a) AT05 and (b) AT40. The main images are typical of the embedded samples (preparation A), and the insets are typical of the ground samples (preparation B).

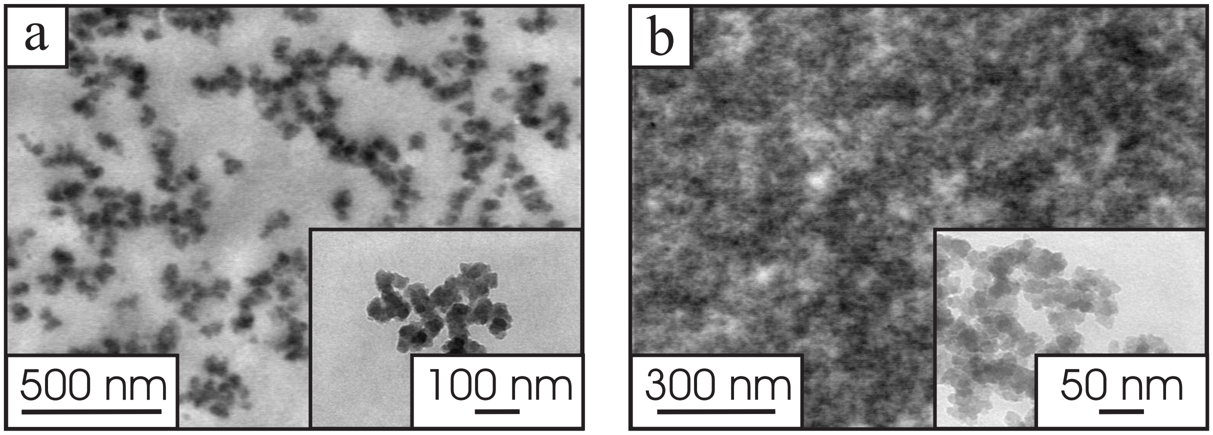
a
500 nm
100 nm
b
300 nm
50 nm

Figure 5.2: Typical TEM micrographs of EDAS xerogels (a) ET025 and (b) ET20. The main images are typical of the embedded samples (preparation A), and the insets are typical of the ground samples (preparation B).

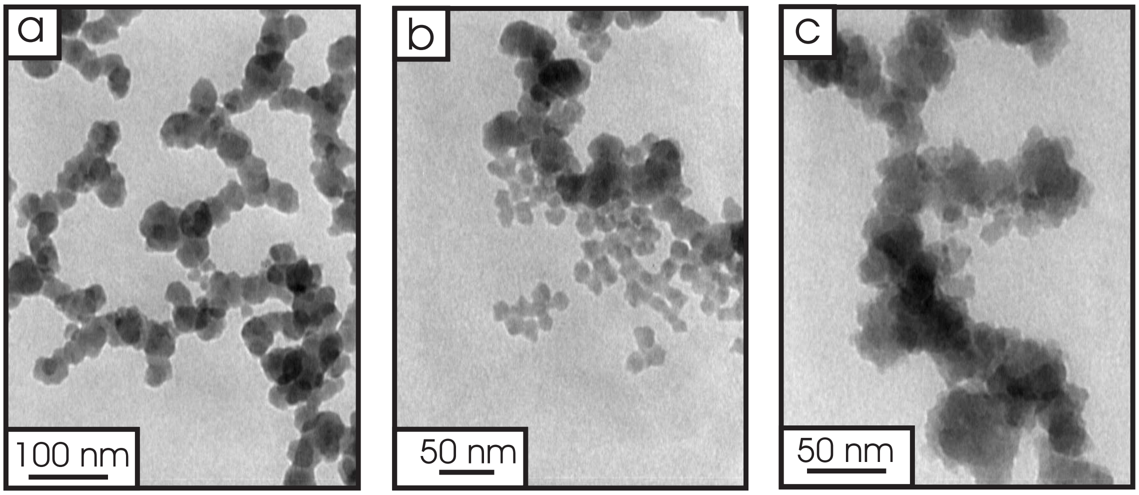

Figure 5.3: Example of TEM micrographs obtained from liquid sample AT025, on which (a) the filaments, (b) the particles and (c) the particles within the filaments are visible.

sol-gel literature [Pekala & Schaefer 1993; Schaefer *et al.* 1995]. For the present samples however, the pearls are generally poorly defined and we shall refer to these structures as *filaments*.

On most type B micrographs, the filaments seem to have a substructure. This is particularly clear for the sample synthesized with the lowest amount of AES (AT025) that resulted in a white liquid and never gelified. Filaments and smaller objects are visible in the sample (Figure 5.3). Although there is no evidence that these objects are particulate, we shall refer to them as *particles*. On all other samples, particles are not isolated and they are only visible as small globular objects that protrude out of the filaments, as in Figure 5.3c. To make these observations more quantitative, the characteristic size of the pores, filaments and particles are measured using image analysis.

The regions between neighboring filaments are the pores of the samples. Their width, $L_{pore}$, is estimated from type A micrographs. Since they are projections of 60 nm thick slices, they can reliably be used to measure objects larger than that size. Because the shape of the pore space is complex, $L_{pore}$ is estimated using an opening granulometry [Serra 1982]. The principle of the method is outlined in Appendix A; it basically consists in assigning a size $L$ to any region of the images that can contain a disk of diameter $L$. This idea is closely related to the more familiar concept of chord length, often used to measure objects with a complex shape [Ohser & Mücklich 2000]. Opening granulometry does not require any user intervention and it is therefore totally objective. The values of $L_{pore}$ reported in Table 5.2 show that the size of the pores is almost the same for all AES samples, and that the pores become much smaller when more EDAS is used. Whenever $L_{pore}$ is smaller that about 60 nm, the size of the pores is underestimated because of the projection effects involved.

Since the filaments are thinner than 60 nm, they presumably overlap in type A micrographs. Preparation B was therefore used to measure their width $L_F$. In order to avoid user subjectivity, an opening granulometry is used here as well. Note that the smallest objects visible in the slices are comparable in size with $L_F$, which means that the grinding of the samples does not modify the width of the filaments. Table 5.2 shows that $L_F$ slightly decreases when more AES is used. The effect is much more marked for EDAS. There is an abrupt increase of $L_F$ from ET15 to ET20. The jump probably reflects a different structure of sample ET20 (see insets of Figure 5.2) and the value of $L_F$ should not be interpreted as the width of the filaments for this sample.

The measurement of the diameter of the particles, $L_{part}$, is more problematic because the filaments cannot be resolved into particles. As the particles overlap everywhere, no user-free method can be used; the globular structures visible on the edges of the filaments are measured manually. The values of $L_{part}$ reported in Table 5.2 are the average and standard deviation of particle size measured on 15 type B micrographs for each sample. The particles are only considered when they are clearly visible, which leads to approximately 20 measurements for each sample. Table 5.2 shows that $L_{part}$ is unchanged when more AES is used and that it decreases markedly when more EDAS is used. At this stage, it is however admitted that the reliability of $L_{part}$ rests mainly on how the values will compare with the other characterization data in the discussion section.

### 5.3.2 Pycnometry and nitrogen adsorption

The bulk and skeletal densities, $\rho_b$, and $\rho_s$, obtained from mercury and helium pycnometry, are reported in Table 5.3. For both AES and EDAS samples, increasing the amount of co-reactant results in a lowering of the skeletal density, as reported for other organo-

Table 5.2: Characteristic lengths of the xerogels, obtained from the various characterization techniques.

| | $L_{pore}$ (nm) | $L_F$ (nm) | $L_{part}$ (nm) | $l_S$ (nm) | $l_P$ (nm) | $L_{KP}$ (nm) | $L_{SAXS}$ (nm) |
|---|---|---|---|---|---|---|---|
| AT05 | 87 | 37 | 12 ± 1 | 9 | 46 | $> 40$ | -$^b$ |
| AT10 | 77 | 34 | 13 ± 2 | 14 | 64 | 31 | -$^b$ |
| AT15 | 76 | 31 | 13 ± 2 | 15 | 66 | 31 | -$^b$ |
| AT25 | 71 | 31 | 15 ± 2 | 16 | 68 | -$^a$ | -$^a$ |
| AT40 | 64 | 29 | 13 ± 2 | 19 | 69 | 31 | -$^b$ |
| ET025 | 240 | 45 | 16 ± 2 | 12 | 69 | $> 40$ | 16 |
| ET04 | 135 | 33 | 14 ± 2 | 10 | 56 | -$^b$ | 12 |
| ET06 | 57 | 27 | 11 ± 2 | 9 | 46 | -$^b$ | -$^b$ |
| ET10 | 28 | 15 | 7.6 ± 1 | 8 | 36 | 16 | -$^b$ |
| ET15 | 23 | 13 | 7.0 ± 1 | 8 | 32 | 12 | -$^b$ |
| ET20 | 9 | (26) | 11 ± 2 | 6 | 18 | 6 | -$^b$ |

$L_{pore}$: size of the pores obtained from the opening granulometry of type A micrographs, $L_F$ : width of the filaments obtained from the opening granulometry of type B micrographs, $L_{part}$: size of the particles measured manually on the type B micrographs, $l_S$ and $l_P$: solid and pore chord lengths, $L_{KP}$: Kratky-Porod size, $L_{SAXS}$: characteristic length corresponding to the position of the hump in the SAXS patterns.
$^a$: data not available
$^b$: not measurable.

Table 5.3: Textural characteristics of the xerogels.

| | $\rho_b$ (g/cm$^3$) | $\rho_s$ (g/cm$^3$) | $V_p$ (cm$^3$/g) | $\epsilon$ (-) | $V_{N2}$ (cm$^3$/g) | $C_{BET}$ (-) | $S_{BET}$ (m$^2$/g) |
|---|---|---|---|---|---|---|---|
| AT05 | 0.39 | 2.26 | 2.15 | 0.83 | 1.50 | 142 | 187 |
| AT10 | 0.38 | 2.08 | 2.17 | 0.82 | 1.40 | 89 | 136 |
| AT15 | 0.38 | 2.02 | 2.12 | 0.81 | 0.85 | 79 | 129 |
| AT25 | 0.38 | 1.96 | 2.11 | 0.81 | 1.53 | 36 | 124 |
| AT40 | 0.40 | 1.88 | 1.94 | 0.78 | 1.02 | 53 | 113 |
| ET025 | 0.30 | 2.65 | 2.84 | 0.85 | 0.53 | 320 | 165 |
| ET04 | 0.32 | 2.13 | 2.62 | 0.85 | 0.67 | 124 | 179 |
| ET06 | 0.34 | 2.10 | 2.49 | 0.84 | 0.90 | 94 | 215 |
| ET10 | 0.37 | 2.04 | 2.18 | 0.82 | 1.34 | 72 | 243 |
| ET15 | 0.39 | 1.97 | 2.07 | 0.80 | 1.53 | 75 | 256 |
| ET20 | 0.50 | 1.91 | 1.49 | 0.74 | 1.52 | 54 | 327 |

$\rho_b$ : bulk density, $\rho_s$ : skeletal density, $V_p$ : porous volume, $\epsilon$ : porosity, $V_{N2}$: amount of nitrogen adsorbed at $p/p_0 = 0.98$, $C_{BET}$: BET constant, $S_{BET}$: BET specific surface area.

silica materials [VanBlaaderen & Vrij 1993]. For the AES xerogels no marked evolution is observed for the bulk density $\rho_b$, while a marked increase in $\rho_b$ is observed when the amount of EDAS is increased.

Figure 5.4 reports the nitrogen adsorption-desorption isotherms measured on the xerogels, the corresponding textural characteristics are in Table 5.3. The isotherms of all the AES samples (Figure 5.4a) are of type II [Lecloux 1981; Rouquerol *et al.* 1994] with a very narrow hysteresis at high pressure, as generally observed for non porous or macroporous solids. This is also the case for the samples synthesized with a small amount of EDAS (ET025 to ET06). On the contrary, for larger amounts of EDAS (ET10 to ET20), the isotherms progressively transform into type IV, that is typical of mesoporous solids wherein capillary condensation occurs [Lecloux 1981; Rouquerol *et al.* 1994]. The porous volumes $V_{N2}$ exhibit no clear trend when increasing the amount of AES (AT05 to AT40), whereas for EDAS xerogels, they clearly increase when more co-reactant is used (ET025 to ET20). For all samples $V_{N2}$ is much lower than $V_p$, except for ET20.

The specific surface $S_{BET}$ undergoes a 40% decrease when increasing the amount of AES (from AT05 to AT40), but it almost doubles when increasing the amount of EDAS (from ET025 to ET20). The BET constant, $C_{BET}$, is relevant for the energy of interaction

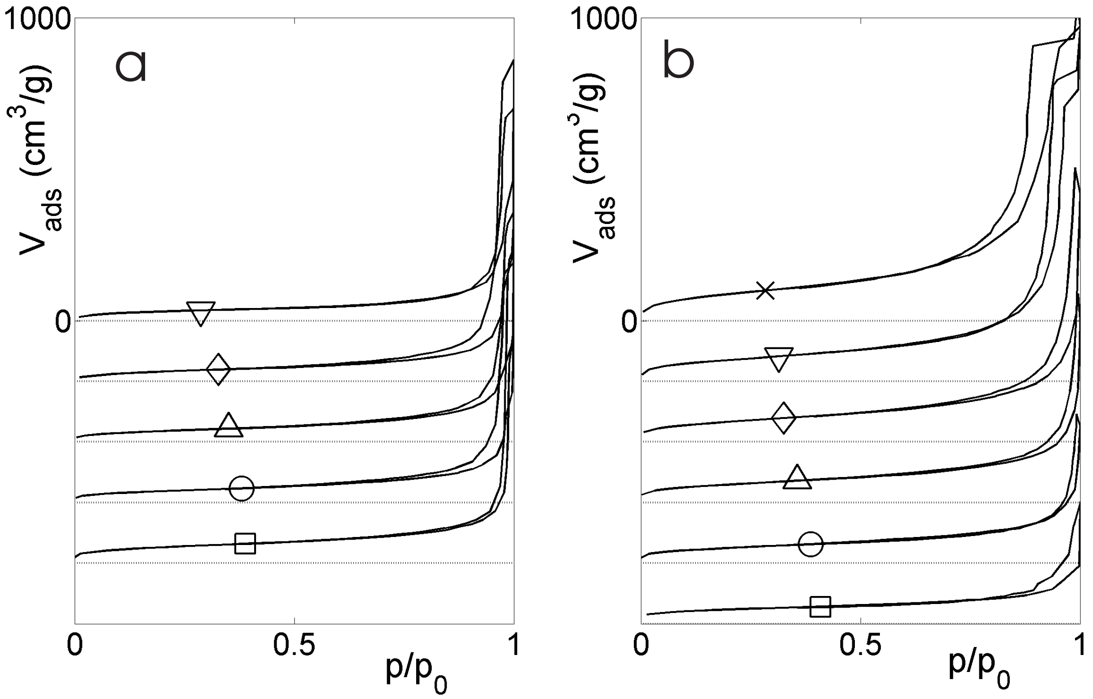

Figure 5.4: Nitrogen adsorption-desorption isotherms measured (a) on AES xerogels AT05 (□), AT10 (◯), AT15 (△), AT25 (◊) and AT40 (▽), and (b) on EDAS xerogels ET025 (□), ET04 (◯), ET06 (△), ET10 (◊), ET15 (▽), and ET20 (×). The isotherms are arbitrarily shifted vertically.

between the nitrogen molecule and the surface of the xerogels, and it can serve as a measure of the polarity of the adsorbent surface. It decreases when the amount of any co-reactant increases (Table 5.3).

The general concept of chord links the specific surface of a solid to the characteristic size of its skeleton or pore space, independently of its geometry [Ohser & Mücklich 2000; Schaefer *et al.* 2004]. Let a two phase (A-B) solid be penetrated by a test line. The chord length $l_A$ of phase A is defined as the average length of the intersections of the test line with phase A. Under general assumptions, the chord length is related to the specific volume $V_A$ and specific area of the interface $S_{AB}$ through the relation $l_A = 4V_A/S_{AB}$ [Russ & Dehoff 1999]. This relation can be used to estimate the pore chord $l_P$ and solid chord $l_S$ of a porous solid as

$$l_P = \frac{4V_p}{S_{BET}} \quad \text{and} \quad l_S = \frac{4}{\rho_s S_{BET}} \tag{5.1}$$

where $V_p$ is the porous volume estimated by pycnometry, and $1/\rho_s$ is the specific volume of the skeleton. The pore and solid chord lengths, $l_P$ and $l_S$, are reported in Table 5.2 together with the other characteristic lengths. For all analyzed samples, $l_P$ is larger than $l_S$, as expected for low density materials. For AES samples, both $l_P$ and $l_S$ increase when the amount of co-reactant is increased, whereas they decrease for EDAS samples.

### 5.3.3 Small Angle X-ray Scattering

The SAXS patterns measured on the xerogels are displayed in Figure 5.5. For AES xerogels, the patterns follow a power law with exponent slightly larger than 4 over a limited range of scattering vector $q$ (Figure 5.5a). The existence of a Porod region, with exponent 4, is typical of the scattering by objects with a smooth surface [Glatter & Kratky 1982]. A deviation from the power law is observed at low $q$, where the patterns exhibit a convex curvature. The value of $q$ at which the deviation is observed is inversely related to the size of the scattering objects. Practically, the characteristic size of the scattering objects is determined from a Kratky-Porod plot, by plotting $Iq^4$ against $q$ [Glatter & Kratky 1982] (Figure 5.6a). The characteristic length is determined as $L_{KP} = 2\pi/q_{max}$, where $q_{max}$ is the position of the maximum of $I(q)q^4$ (Table 5.2). For AT05, $Iq^4$ continuously increases with decreasing $q$, which means that $L_{KP}$ is larger than the limit of the SAXS (about 40

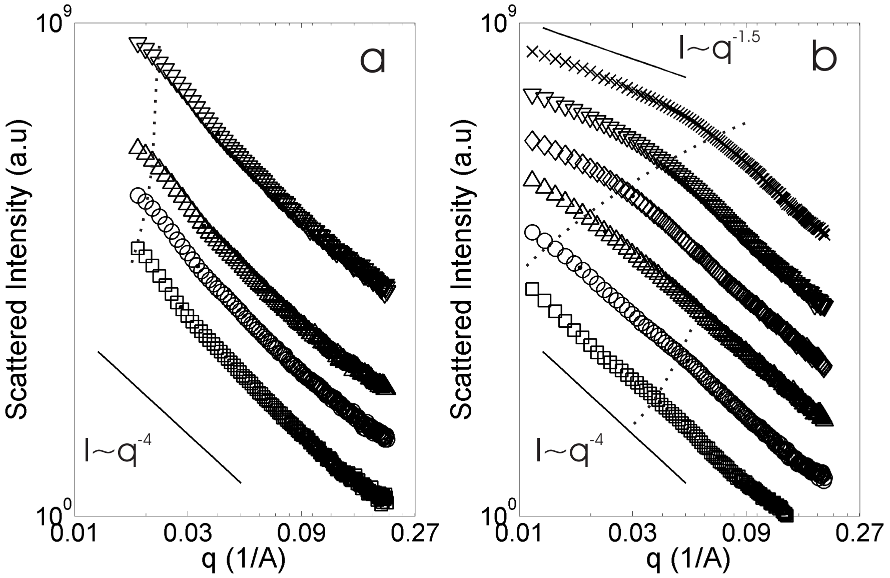

Figure 5.5: SAXS patterns measured (a) on AES xerogels AT05 (□), AT10 (◯), AT15 (△), AT25 (◊) and AT40 (▽), and (b) on EDAS xerogels ET025 (□), ET04 (◯), ET06 (△), ET10 (◊), ET15 (▽), and ET20 (×). The dotted lines highlight the evolution of the characteristic lengths upon increasing the amount of additive.

nm for the used configuration). The dotted line in Figure 5.5a is a guide for the eye, it passes approximately through the estimated values of $L_{KP}$.

The SAXS patterns of EDAS xerogels are more complex (Figure 5.5b). The SAXS of ET20 exhibits a Porod scattering at high angles, and a power law scattering with an exponent slightly larger than 1 at lower angles. In the present context, the pattern can be interpreted as the scattering from filaments, with a diameter corresponding to the cut-off between the two observed power laws, and with lengths too large for the measured $q$ range [Glatter & Kratky 1982]. Decreasing the amount of EDAS (from ET20 to ET06), the shape of the scattering patterns remains unchanged, but the cut-off shifts towards smaller angles, which means that the diameter of the filaments becomes larger. For the sample with the smallest amount of EDAS (ET025), the diameter becomes larger than about 40 nm and it leaves the measured $q$ range. The diameters of the filaments are called $L_{KP}$ and are reported in Table 5.2; they are calculated as previously from a Kratky-Porod plot (Figure 5.6b). For ET04 and ET06, $L_{KP}$ cannot be estimated because $Iq^4$ exhibits no maximum. For samples ET04 and ET025, a slight hump is present in the middle of the

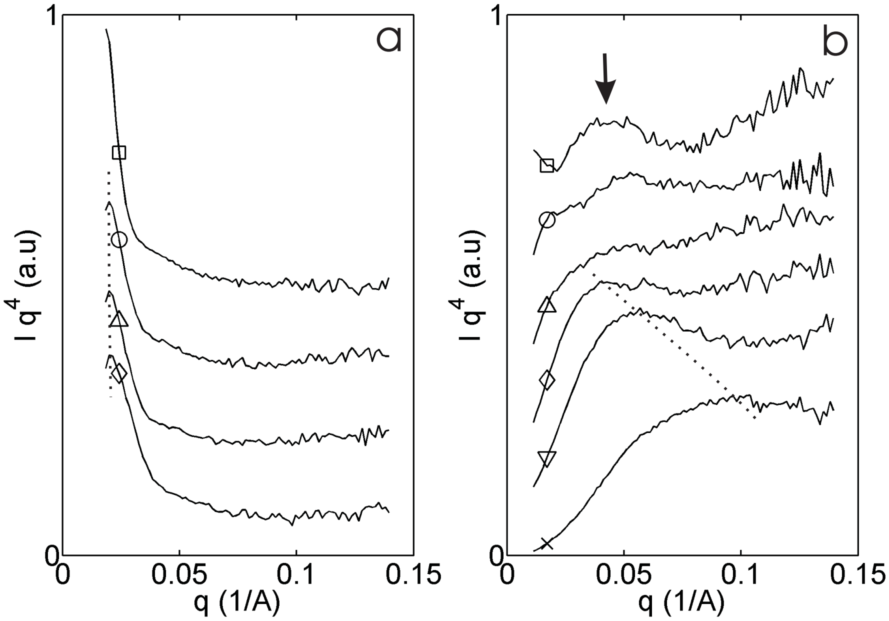

Figure 5.6: Kratky-Porod plots of the SAXS patterns of (a) AES xerogels AT05 (□), AT10 (○), AT15 (△), AT25 (◇) and AT40 (▽), and of (b) EDAS xerogels ET025 (□), ET04 (○), ET06 (△), ET10 (◇), ET15 (▽), and ET20 (×). The dotted lines highlight the position of the maximum. The hump in the SAXS pattern of ET025 is indicated by an arrow.

Porod region (see Figure 5.5b). The very presence of a hump suggests that the interior of the filaments is not uniform, but that it has itself a structure. The length scale of these substructures, corresponding to the $q$ position of the hump through the approximate relation $L_{SAXS} = 2\pi/q$, is reported in Table 5.2.

## 5.4 Discussion

### 5.4.1 Local and global evidence for the hierarchical structure of the xerogels

Electron microscopy shows that the structure of AES and EDAS xerogels is hierarchical. It is a macroporous sponge-like structure, supported by filaments, with each filament being made of smaller structures we called particles. Evidence of this structure needs to be found in the global macroscopic characterization data. For that purpose the characteristic length of each identified structural level (macropores, filaments and particles) was estimated from the micrographs.

The large scale structure of the samples is supported by macroscopic evidence. First, the volume of nitrogen sorbed near the saturation, $V_{N2}$, is a fraction of the porous volume $V_p$ estimated from pycnometry, which points at the existence of macropores [Lecloux 1981; Rouquerol *et al.* 1994]. Furthermore, an analysis of the adsorption data of ET025 and ET04 [Gommes *et al.* 2005] shows that the adsorbent surface is convex in these samples, with a radius of curvature that compares well with the width of the filaments. The fact that width of the filaments $L_F$ measured by TEM compares well with $L_{KP}$ for all samples (Table 5.2) suggests that the structures observed by TEM are indeed representative of the entire macroscopic samples.

An important issue is the existence of a substructure within the filaments, which we call particles. For the sample with the lowest amount of AES, that did not gelify, the existence of globular objects within the filaments is evident from TEM (Figure 5.3). For the samples synthesized with a small amount of EDAS, it is also seen from the SAXS that structures with a size smaller than the filaments do exist (Figure 5.5b). As for ET025 and ET04, $L_{SAXS}$ compares well with the size of the particles measured manually on the edges of the filaments, $L_{part}$, the particles can reasonably be thought to exist in these samples as well.

Samples synthesized with larger amounts of co-reactant lack macroscopic evidence of particles. For AES samples, it can however be noted that the specific surface $S_{BET}$ decreases when more AES is used, while the width of the filaments $L_F$ remains almost unchanged, and even slightly decreases (Tables 5.2 and 5.3). It must therefore be admitted that there is an inner structure within the filaments, the surface area of which becomes lower when more AES is used. A similar conclusion can be reached for EDAS samples. However, because all the structures become smaller when more EDAS is used, it is impossible to argue on the sole basis of $S_{BET}$; chord lengths must be considered instead. For ET025, the solid chord length is much smaller than the width of the filaments, but it compares well with $L_{part}$ (Table 5.2). This means that the filaments alone cannot explain the observed value of $S_{BET}$; it can only be obtained with objects of the same size as the particles. The same conclusion can be reached by considering the pore chord length $l_P$, that is significantly smaller than $L_{pore}$ for ET025. This means that pores smaller than those visible on type A micrographs must be present in that sample. On the contrary, for the samples synthesized with large amounts of EDAS, $l_P$ compares well with $L_{pore}$, although image analysis probably underestimates the pore size for these samples (see section 5.3.1).

In summary, the macropore-filament-particle hierarchical structure of the xerogels derived from TEM is in agreement with the macroscopic characterization data. The size of the structures is almost independent of the amount of AES, but it decreases markedly when more EDAS is used. Finally, for small amounts of co-reactant the filaments can be thought of as condensates of particles; increasing the amounts of any co-reactant results in the progressive merger of the particles.

### 5.4.2 Remnants of the phase separation in the xerogels

The fact that each structural level of the xerogels has a well defined length scale suggests that the whole structure results from the succession of different physicochemical events, rather than from their simultaneous occurrence. Quite generally, the succession of events leading to the final material can be bottom-up (BU) or top-down (TD). In the former case, the smallest structures are obtained first and the larger structures are built using the smaller ones as building blocks. In the latter case, the largest structures are obtained first and the smaller objects result from a process that occurs within these larger structures.

The aggregation model of gelation [Brinker & Scherer 1990; Iler 1979] is typically bottom-up. Using this model for EDAS and AES gels, one would have to admit that the initially homogeneous reacting solution leads first to the formation of the particles, then to their aggregation into filaments, until a percolating network is formed at the gel point (upper path of Figure 5.7). Several chemical mechanisms could explain the formation of monodisperse particles [Iler 1979; Lee *et al.* 1997]. It would however be unclear why anisotropic structures such as filaments would form. One would also expect fractal-like structures to form, with no characteristic length [Viscek 1992], whereas the structure of AES and of EDAS xerogels have well defined characteristic length scales. Moreover, in a BU approach, the formation of the large scale percolating network responsible for the gelation is the last event. For both AES and EDAS gels, the time for turbidity is significantly lower than the gel time (Table 5.1). Since turbidity is associated with the formation of

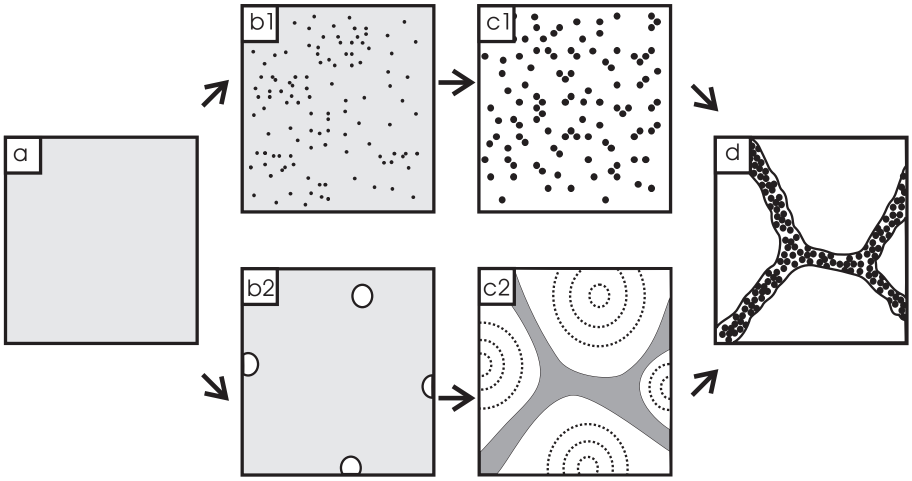

Figure 5.7: Possible bottom-up (upper path) and top-down (lower path) mechanisms for the transition from a homogeneous polymerizing solution (a) to a sponge-like filamentary structure with filaments made of particles (d). Bottom-up mechanism: (b1-c1) nucleation and growth of particles, (c1-d) aggregation of the particles to create the filamentary structure. Top-down mechanism: (b2-c2) nucleation and growth of solvent vacuoles, (c2-d) secondary phase separation by which the particles are created within the filaments.

structures whith a size comparable with the visible light wavelength (larger than about 500 nm), this observation shows that the largest pores of the gels are formed well before the gel point. Furthermore, it has been shown in chapter 4 that the nanometric structures of EDAS gels, *i.e.* the particles and the filaments, are not necessarily formed yet when gelation occurs. These arguments suggest that a BU model cannot explain the formation of the structure of the EDAS and AES xerogels.

Top-down processes are frequently encountered during the structuring of organic polymer blends [Olabisi *et al.* 1979]. Typically, when the mutual solubility of two polymers A and B lowers, resulting *e.g.* from a curing reaction, a phase separation occurs that leads to the creation of A-rich and B-rich phases that are thermodynamically stable for the given state of curing. Since the curing reactions can continue in each phase, they can later become unstable again and an additional phase separation can occur, leading to a further structuring of the A-rich and B-rich phases. If this process continues, it naturally leads to a hierarchical structure containing as many structural levels as successive phase separations. Double phase separations are common [Clarke *et al.* 1995]; as many as three successive phase separations are sometimes reported [VandenPoel *et al.* 2005].

The succession of the possible events involved in a TD process for the formation of AES and EDAS gels is illustrated by the lower path of Figure 5.7. As the hydrolysis and condensation of the silica precursors occur, their solubility in the solvent decreases, which triggers the phase separation [Lee *et al.* 1997; Nakanishi 1997]. In the present case of macromolecules, it is likely that a viscoelastic phase separation is at work [Tanaka 1996]. This scenario is universally encountered whenever the demixing species have different rheological properties, in which case regions of the least viscous phase nucleate and grow. According to these arguments, the phase separation in AES and EDAS gels presumably occurs through the appearance and growth of solvent vacuoles (Figure 5.7b2). Once the nucleated vacuoles have grown sufficiently to touch each other, the silica is concentrated in a phase with the morphology of a sparse columnar network (Figure 5.7c2). Similar structures often result from a competition between gelation and phase separation, as observed for both organic gels [Aubert 1988; Jackson & Shaw 1990; Raman & Palmese 2005] and inorganic gels [Fujita *et al.* 2004]. Since the reactions continue in the silica-rich phase, a secondary phase separation can occur, when the already created filaments decompose into smaller regions that we called particles (Figure 5.7e). It must be noticed that the importance of viscoelastic effects during the early stage of spinodal decomposition of sample ET20 has been evidenced in Chapter 4 (Figure 4.10).

The TD scenario would explain quite naturally the various structural levels of both AES and EDAS xerogels. Moreover, the secondary phase separation is directly supported by time-resolved synchrotron SAXS studies reported in Chapter 4 during the formation of EDAS and AES samples. The length scales analyzed in these previous SAXS studies are in the 3-60 nm range, *i.e.* they encompass the size of the structures that we call particles in the present chapter. The sequence of events in the SAXS measurements is: first the appearance and growth of a maximum in the SAXS patterns, secondly its shift towards smaller angles, and in the meantime a significant increase of the intensity scattered at very low angles. The features are interpreted as a reaction-induced spinodal phase separation [Bates & Wiltzius 1989] in the 3-60 nm range, together with the appearance of a larger structure mainly outside of the measured $q$ range. SAXS also shows that the evolution of nanometer structure can continue long after the gel point. The chronology of the events during the formation of the samples is clearly the following (see also Table 5.1). (i) The reacting solution becomes turbid, which means that structures comparable in size with the visible light wavelength have appeared. In the previous SAXS studies, this corresponds to the appearance of a scattered intensity at very low angles. We now call this process the primary phase separation; it leads to the macropores and filaments. (ii) Gelation occurs as a consequence of the condensation reactions continuing in the silica-rich phase. (iii) The formation of the particles within the filaments occurs in the meantime and it continues after the gel point. It is this secondary phase separation that has been followed by SAXS in Chapter 4.

A marked effect of AES is to speed up the gel formation, as evidenced by its impact on the gel time (Table 5.1). In alkaline conditions however organically substituted trialkoxysilanes are less reactive than tetraalkoxysilanes towards hydrolysis and condensation [Avnir *et al.* 1998]. The accelerating effect of AES could result from the presence of the amine that would act as an internal catalyst of the molecule [Hüsing *et al.* 1999], but the very occurrence of phase separation suggests that physical effects can play an important role as well [Lee *et al.* 1997; Sefcik & McCormick 1997]. For instance, the AES molecule (see Table 1.1 on page 9) could possess an amphiphilic character with a silicon alkoxide head and an organic moiety having different affinities for the two phases. AES could therefore speed up the phase separation, by lowering the surface tension between silica and ethanol phases. The AES molecules would act as surfactants; they would be statistically localized at the silica-ethanol interface. This could be the origin of the lowering of $C_{BET}$ when more co-reactant is used (Table 5.3). Since $C_{BET}$ is a measure of the polarity of the adsorbent surface, the trend suggests that the weakly polarized propyl groups cover the adsorbent surface, as observed by other authors working on similar systems [Hüsing *et al.* 1998; 1999; VanBlaaderen & Vrij 1993].

The role of EDAS is more complex. Owing to its structure (Table 1.1 on page 9) it could have an amphiphilic character and favour the phase separation in the same way as AES does. This scenario is confirmed by the impact of EDAS on the $C_{BET}$ constant (Table 5.3). Furthermore, it has been shown that Pd/$SiO_2$ xerogels synthesized with Si-PzPy-Pd complexes (see Table 1.1) have the same activity for the reaction of cyclopropanation of olefins than the free Si-PzPy-Pd complex in solution [Sacco *et al.* 2005]. This means that the Pd complexes are very accessible in the xerogels, as would be expected if they were at the surface of the silica skeleton. However, as EDAS is far more reactive than TEOS its role cannot be only physical. For instance, the rate of hydrolysis of AES in water at pH = 7 is 0.38 $h^{-1}$ and that of EDAS in the same conditions is 340 $h^{-1}$ [Brand *et al.* 1999]. EDAS can therefore play the role of a surfactant for a very limited period; once it has hydrolyzed and possibly condensed with other molecules its role must change. The polymerization of TEOS is an auto-accelerating process because highly condensed species are more prone to hydrolysis and condensation than monomeric TEOS [Brinker & Scherer 1990; Sefcik & McCormick 1997]. Therefore, a small amount of more reactive EDAS might seed the polymerization and accelerate the whole reaction.

With more EDAS, the polymerization is more rapid and the species are already highly reticulated when they demix. The length scale at which the phase separations occur, results from a balance between the lyophobicity of the species, *i.e.* their incompatibility with the solvent, that favours the formation of large domains, and the reticulation that favours a short-scale phase separation [Olabisi *et al.* 1979; Schaefer *et al.* 2004]. Therefore increasing the reticulation of the silica network, for instance by increasing the amount of EDAS, should naturally lead to smaller structures.

## 5.5 Wet and dry samples

In order to facilitate the comparison of wet and dry samples, Table 5.4 summarizes some characteristics of the gels and of the xerogels taken from Tables 4.1 and 5.2. The analysis below follows the same lines as section 3.5 where the characteristic sizes of Pd/$SiO_2$ gels and xerogels are compared.

The comparison of the final asymptotic exponents $\alpha$ of the gels and xerogels shows a qualitative change of structure during desiccation. Both AES and EDAS xerogels are characterized by $\alpha = 4$. This means that the scattering objects in the xerogels have a clear-cut surface [Glatter & Kratky 1982]. On the other hand for AES gels $\alpha = 3.5$, which suggests that the scattering objects of the gels are non-porous with a fractally rough surface [Schmidt 1991]. For EDAS gels $\alpha \leq 2.5$, which is reminiscent of polymers in solution [Daoud & Martin 1989; deGennes 1979b].

These qualitative changes are necessarily accompanied by a shrinkage of the structures

Table 5.4: Characteristic of the final gels and of the xerogels.

| | $l_c^{(e)c}$ (nm) | $\alpha_g{}^c$ | $L_F{}^d$ (nm) | $L_{part}{}^d$ (nm) | $L_{KP}{}^d$ (nm) | $\alpha_x$ |
|---|---|---|---|---|---|---|
| AT05 | 42 | 3.5 | 37 | 12 ± 1 | > 40 | 4 |
| AT10 | -[a] | -[a] | 34 | 13 ± 2 | 31 | 4 |
| AT15 | 39 | 3.5 | 31 | 13 ± 2 | 31 | 4 |
| AT25 | -[a] | -[a] | 31 | 15 ± 2 | -[a] | -[a] |
| AT40 | 37 | 3.5 | 29 | 13 ± 2 | 31 | 4 |
| ET025 | 47 | 2.5 | 45 | 16 ± 2 | > 40 | 4 |
| ET04 | 43 | 2.5 | 33 | 14 ± 2 | -[b] | 4 |
| ET06 | 43 | 2.5 | 27 | 11 ± 2 | -[b] | 4 |
| ET10 | -[a] | -[a] | 15 | 7.6 ± 1 | 16 | 4 |
| ET15 | -[a] | -[a] | 13 | 7.0 ± 1 | 12 | 4 |
| ET20 | 40 | 2 | (26) | 11 ± 2 | 6 | 4 |

$l_C^{(e)}$: final characteristic size of the gels, $\alpha_g$: final asymptotic scattering exponent of the gels, $L_F$ : width of the filaments of the xerogels, $L_{part}$: size of the particles of the xerogels, $L_{KP}$: Kratky-Porod length of the xerogels, $\alpha_x$: asymptotic scattering exponent of the xerogels.

[a]: data not available

[b]: not measurable

[c]: taken from Table 4.1 on page 59

[d]: taken from Table 5.2 on page 87.

at the nanometer scale. In that respect, it is useful to compare the characteristic sizes obtained on wet and dry samples. As $l_C^{(e)}$ corresponds to the position of the maximum of the scattered intensity, it has to be interpreted as a pseudo-periodicity (see Figure 3.9 at page 48). In the present context $l_C^{(e)}$ must therefore be related to the distance between the particles within the filaments. This length scale is close to 40 nm for all AES and EDAS gels, independently of the amount of co-reactant. After desiccation, the characteristic sizes of AES xerogels $L_{part}$, $L_F$ and $L_{KP}$ are but slightly modified when more co-reactant is used. On the contrary, the corresponding characteristic lengths of EDAS xerogels become markedly smaller when more co-reactant is used. This means that the nanostructure of EDAS gels undergo a larger shrinkage when more co-reactant is used.

## 5.6 Conclusion

The present chapter contributes to fill the gap between the texture of EDAS and AES non calcined xerogels and the *in situ* monitoring of the formation of the gels' nanostructure by SAXS in Chapter 4. A set of independent characterization techniques was applied to investigate the texture of the two series of xerogels. The global structure of both AES and EDAS xerogels comprises several structural levels with well defined length scales: the largest structure is that of the macropores, they are supported by elongated filaments, and each filament is made of smaller particle-like structures. Increasing the amount of AES leaves the final structure of the gels almost unchanged, while increasing the amount of EDAS shifts the final structure towards smaller sizes.

The hierarchy of structural levels and the fact that the largest structures are formed before the smallest ones, hint at multiple phase separation. The primary phase separation would be responsible for the formation of the largest pores and filaments. The secondary phase separation evidenced by SAXS in Chapter 4 creates the smallest structures within the filaments.

An interesting observation that arises from the comparison of the characteristic lengths of the gels and xerogels is that desiccation enhances the differences between various EDAS gels. This is not observed for AES gels. The impact of desiccation of the microstructure of the gels is addressed more thoroughly in Chapter 6.

# Chapter 6

# Porosity of the gels, aerogels and xerogels, by beam-bending and textural characterisations

## 6.1 Introduction

The existence of a hierarchical structure in AES and EDAS xerogels has been demonstrated in the previous chapters, with a filamentary structure at large scale, each filament being itself made up by smaller structures.

The following questions are addressed in the present chapter. *How can it be ascertained that this structure is already present in the gels themselves, before desiccation? What is the impact of desiccation on the microstructure of the gels?*

The existence of structures with a size comparable to that of the filaments' substructure was evidenced in the gels by SAXS in Chapter 4. The large scale porosity of the gels is analyzed in the present chapter using beam bending. The measurements enable one to estimate the gels' permeability, which is related to the size of their largest pores.

It is customary to assume that a supercritical extraction of the solvent preserves the structure of the gel. Aerogels obtained from EDAS and AES are characterized using nitrogen adsorption, Small Angle X-ray Scattering, and mercury porosimetry. The characterisation data of the aerogels are compared with those of the xerogels.

## 6.2 Materials and method

### 6.2.1 Synthesis and moulding of the gels

Silica gels synthesized with EDAS and AES as co-reactants are synthesized as described in the previous chapters. The nomenclature of Table 5.1 on page 82 is used in the present chapter as well.

The bending measurement requires that the gels be synthesized in the form of small elongated cylinders with an aspect ratio close to 10. Because of the absence of syneresis, the gels still adhere to the walls of the vessel in which they are synthesized, even after ageing for weeks. Flawless rods of gel can therefore not be obtained by simple moulding. The used procedure is as follows. First, a roll of polyethylene sheet is introduced inside a glass tube with the appropriate diameter. The tube is closed at one end with a stopper, and the precursor solution is poured inside the tube and the roll. Once the desired ageing is reached, the gel is extracted from the mould by pulling the plastic sheet with tweezers. The plastic sheet is then unrolled outside the glass tube, and the monolithic gel rod is recovered.

### 6.2.2 Bending measurements

The beam bending measurements were performed in the department of Civil and Environmental Engineering at Princeton University on an apparatus developed by Professor G.W. Scherer [Scherer 1994c; 1995]. A sketch of the device is given in Figure 6.1a. The extremity of the pushrod that touches the gel is a cylinder with an approximate diameter of 6.35 mm. This large value is intended to minimize the indentation of the gel at the point of contact. The upper extremity of the pushrod is attached to a load cell with a range of 50 g. The vertical displacement of the pushrod is controlled by a motor, and it is measured by a displacement cell. The extremities of the gel rest on supports with the shape of a V, and each edge of the V is an aluminium roller with diameter 6.35 mm. The gel rods have a diameter of 12 mm and the distance between the supports is 100 mm. The supports are attached to an aluminium tank filled with liquid. The entire apparatus is inside an incubator to maintain the temperature at 30°C.

The gels are positioned on the supports in the tank filled with liquid, and the pushrod

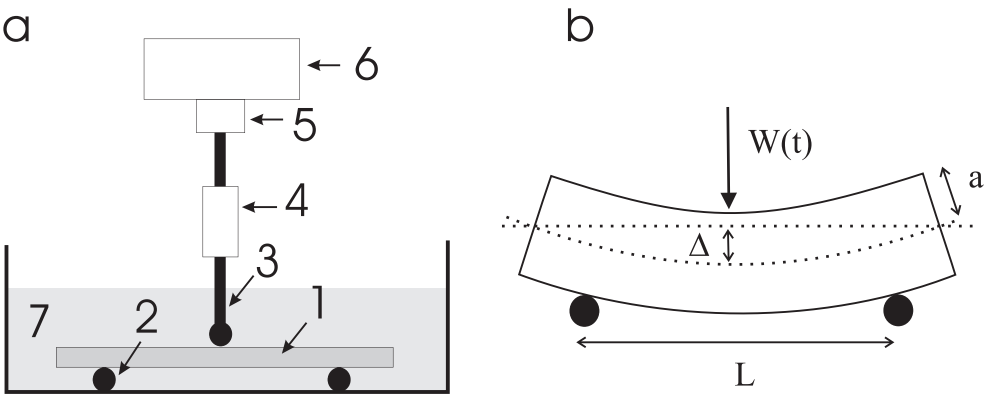

Figure 6.1: (a) Experimental device with (1) gel beam, (2) aluminium roller, (3) pushrod, (4) displacement cell, (5) load cell, (6) step motor, and (7) solvent bath. The entire device is inside an incubator to avoid temperature fluctuations. (b) Scheme of the deformed beam with the applied force $W(t)$, displacement $\Delta$, distance between supports $L$, and beam radius $a$.

is slowly lowered until it touches the surface of the rod. After 1 h of equilibration, the measurement is initiated by lowering rapidly the pushrod by about 2 mm. The parts of the gel above the neutral axis of the rod are put in compression and the parts below are in tension (Figure 6.1b). This induces a flow of the liquid phase of the gel that results in a lowering of the force needed to maintain a given deformation. The force relaxation curves of each sample are obtained by measuring the evolution of the force needed to maintain a given deformation.

Two types of measurements are performed: (i) as synthesized gels are immersed in ethanol and measured, (ii) the same gels are measured in decanol after having been washed for one week in a large excess of that liquid.

### 6.2.3 Drying of the gels and characterization of the xerogels and aerogels

Xerogels of EDAS and AES are obtained by the same vacuum drying procedure as described in section 5.2.1 of Chapter 5. Aerogels of EDAS and of AES are obtained by direct supercritical $CO_2$ drying, which includes a direct dynamic washing with supercritical $CO_2$ before slow isothermal depressurization [Rigacci *et al.* 2004]. The supercritical drying was kindly performed by Dr. A. Rigacci in the École des Mines de Paris, in Sophia-Antipolis, France.

Electron microscopy on the aerogels is performed by grinding the samples, dispersing the powder in ethanol, and depositing a drop of the supernatant on the microscopy grid (Preparation B, in section 5.2.3).

Small Angle X-ray scattering patterns were collected in the Laboratorium voor Macromoleculaire Structuurchemie, at the Katholieke Universiteit Leuven, on a Bruker NanoSTAR apparatus. The apparatus is configured with the HI-STAR 2D detector at 107 cm from the sample. The 2D patterns are corrected for the detector response, distortions due to the use of a flat detector, and background. The isotropic patterns are averaged azimuthally and expressed as the scattered intensity as a function of the scattering vector $q = 4\pi/\lambda \sin(\theta/2)$, $\lambda$ being the wavelength (1.54 Å), and $\theta$ being the scattering angle.

Nitrogen adsorption-desorption isotherms are measured on the aerogels at 77 K on a Carlo Erba Sorptomatic 1990 volumetric device, after outgasing the samples overnight at room temperature at a pressure lower than $10^{-4}$ Pa. The data are fitted with the BET model [Lecloux 1981]; the specific surface area $S_{BET}$ and the BET constant $C_{BET}$ are estimated.

Mercury porosimetry is performed on monolithic samples outgassed down to 0.01 Pa for at least 2 h at room temperature. The samples are transferred to a Carlo Erba Pascal 140 porosimeter on which the mercury pressure is raised from *ca* 0.01 MPa to 0.4 MPa, and afterwards to a Carlo Erba 240 porosimeter on which the pressure is raised from atmospheric pressure to 200 MPa. A blank curve is subtracted from the raw data to correct for the compressibility of mercury.

## 6.3 Results

### 6.3.1 Beam bending results

#### Raw data

Figure 6.2 plots the force relaxation curves of EDAS and of AES gels after one week of ageing. All curves exhibit a two step decay of the force $W(t)$ needed to maintain a given deformation $\Delta$ of the gel rod. The first relaxation, with a duration of about 10 s, is a hydrodynamic process related to the flow of the liquid phase of the gel, from the regions

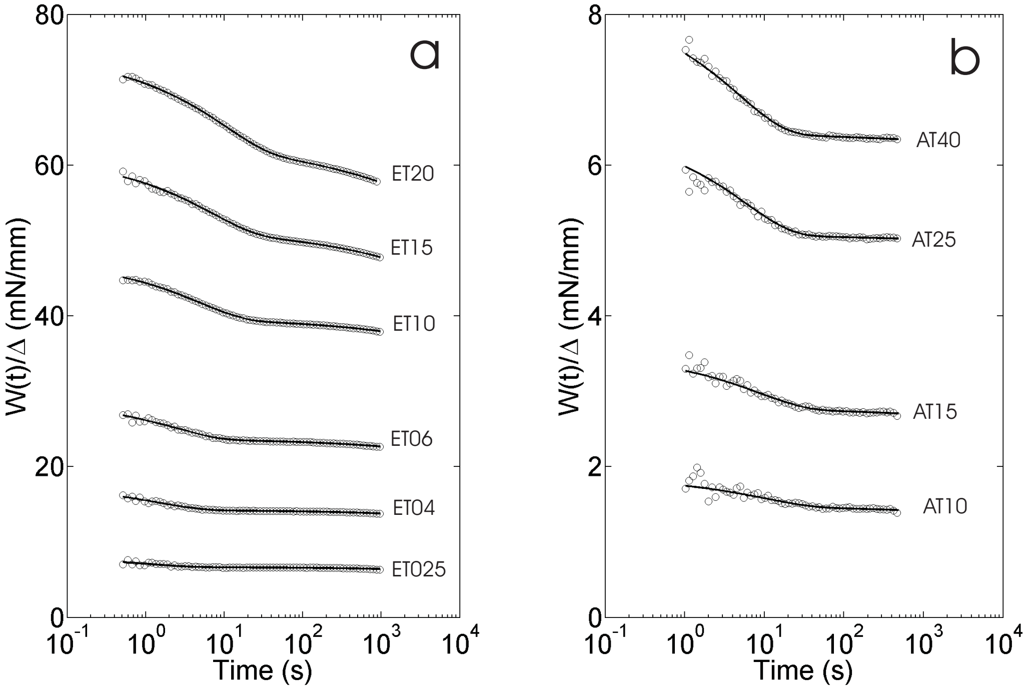

Figure 6.2: Force relaxation curves of (a) EDAS gels and (b) AES gels, measured in ethanol, after one week of ageing. The circles are the experimental data, the solid lines are calculated by adjusting them with Equation 6.1. Note the different scales in the two graphics.

where it is in compression towards the regions where it is in tension [Scherer 1992]. The second slower decay is related to the viscoelastic relaxation of the solid phase itself of the gel [Scherer 1994c]; it typically occurs over a period of hours.

Increasing the amount of EDAS results in an upward shift of the curves in Figure 6.2, which means that the stiffness of the gel increases. A similar conclusion holds for AES gels, although they are globally less stiff than EDAS gels.

In order to test the effect of ageing, EDAS gels were also measured after only 24 h of ageing. Samples ET025 and ET04 are so soft after 24 h that they cannot be measured. For all gels, ageing from 24 h to 1 week results in a larger stiffness and a smaller hydrodynamic relaxation time, as exemplified in Figure 6.3a. All AES gels are too soft to be measured after just 24 h of ageing.

The quantitative analysis of the relaxation data in terms of the permeability of the gel's

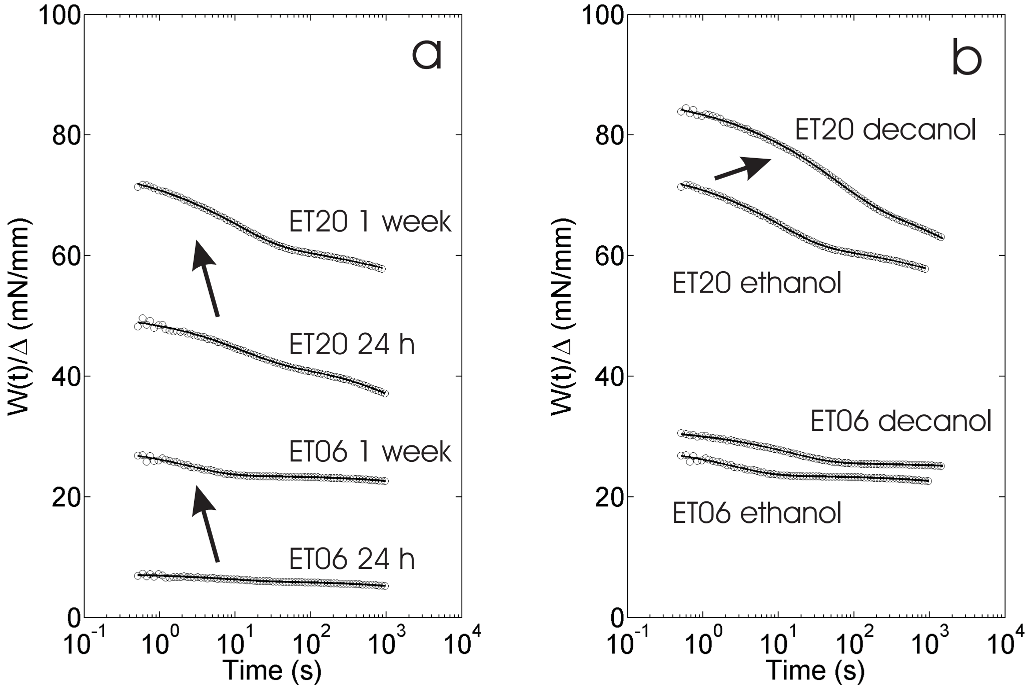

Figure 6.3: Effect of (a) ageing and of (b) ethanol-decanol solvent exchange on the force relaxation curves of gels ET06 and ET20. The circles are the experimental data and the solid lines are calculated by adjusting them with Equation 6.1.

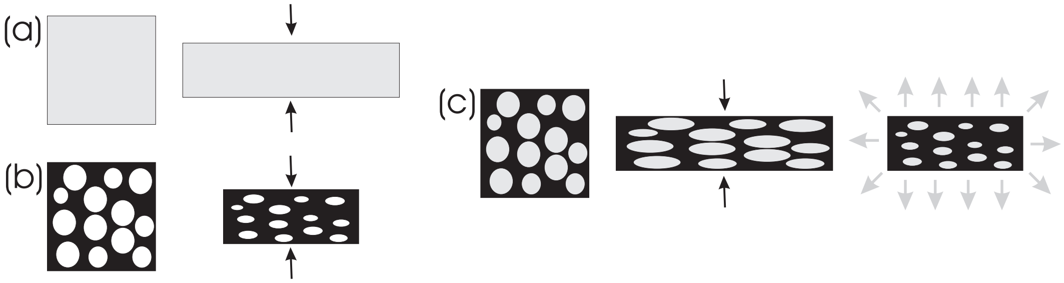

Figure 6.4: During a uniaxial compression, (a) a liquid expands laterally to keep its volume unchanged, and (b) a porous solid expands to a lesser extent and reduces its porosity. When a gel is compressed (c), it first keeps its volume unchanged and it afterwards shrinks by expelling its liquid.

skeleton requires the viscosity of the liquid that fills the porosity of the gel to be known precisely. The mother liquor of the gels is not pure ethanol as it contains a significant amount of water and might also contain some partially polymerized TEOS; its viscosity is poorly known. The gels are are therefore washed in a large excess of decanol, as explained in section 6.2.2, by which the porosity fills completely with a liquid of known viscosity. Furthermore, decanol being very viscous, this procedure increases the hydrodynamic relaxation time, which enables a more precise measurement. As exemplified in Figure 6.3b, the gels washed in decanol are slightly stiffer than those measured in ethanol, and their hydrodynamic relaxation is significantly slower, as expected.

### Data reduction

The hydrodynamic relaxation originates in the biphasic nature of the gels. They are made of a solid phase and of a liquid phase with different mechanical properties (Figure 6.4). During a uniaxial compression, the liquid phase expands laterally to keep its volume unchanged; the solid phase can expand to a lesser extent and reduce its porosity. The gel therefore first keeps its volume unchanged and afterwards shrinks by expelling its liquid. The global mechanical behaviour can be modelled by coupling the theory of elasticity [Landau & Lifshitz 1959] for the porous skeleton and Darcy's law [Adler 1992] for the flow of the liquid.

In the case of the bending of a gel beam with a circular cross section, the theory predicts that the time evolution of the force $W(t)$ needed to maintain a given deformation of the beam is [Scherer 1992; 1994b]

$$W(t) = W(0)\left[\frac{2(1+\nu)}{3} + \frac{(1-2\nu)}{3}S\left(\frac{t}{\tau_h}\right)\right]\exp\left[-\left(\frac{t}{\tau_{VE}}\right)^b\right] \tag{6.1}$$

where $W(0)$ is the initial load that immediately follows the deflection, $\nu$ is the Poisson ratio of the gel's skeleton, $S$ is the hydrodynamic relaxation function, $\tau_h$ is the hydrodynamic relaxation time, $\tau_{VE}$ is an average viscoelastic relaxation time and $b$ is a parameter related to the breadth of the distribution of viscoelastic relaxation times [Scherer 1994b;c].

The initial load $W(0)$ is related to the Young modulus $E$ of the gel's skeleton, to the moment of inertia $I$ and to the length $L$ of the beam, and to the deflection of the beam $\Delta$ through

$$W(0) = \frac{72EI}{(1+\nu)L^3}\Delta \tag{6.2}$$

The hydrodynamic relaxation time is given by

$$\tau_h = \frac{\eta}{D}\frac{a^2 2(1+\nu)(1-2\nu)}{E} \tag{6.3}$$

where $\eta$ is the viscosity of the liquid phase of the gel, $D$ is the permeability of the gel, and $a$ is the radius of the beam's section. The hydrodynamic relaxation function $S(t/\tau_h)$ is given by

$$S\left(\frac{t}{\tau_h}\right) = 8\sum_{n=1}^{\infty}\frac{1}{\beta_n^2}\exp\left(-\beta_n^2\frac{t}{\tau_h}\right) \tag{6.4}$$

where $\beta_n$ are the zeros of the Bessel function of the first kind of order 1, $J_1(\beta_n) = 0$.

The fitting of the experimental data with Equation 6.1 is performed in the Matlab® environment, as described in Appendix B. The values of the Poisson ratio $\nu$, Young modulus $E$, and of $D/\eta$ obtained from the fits are reported in Table 6.1. No clear trend is detected for the viscoelastic relaxation parameters $\tau_{VE}$ and $b$. As discussed in Appendix B, these parameters are also the ones that are affected by the largest uncertainty. They are not reported.

In order to compare the mechanical properties of the gels with those of the corresponding aerogels and xerogels (estimated from mercury porosimetry in the next section), they are expressed as the compression modulus $K$. For a linear elastic solid, the compression modulus is related to Young modulus and Poisson ratio by [Landau & Lifshitz 1959]

$$K = \frac{E}{3(1-2\nu)} \tag{6.5}$$

Table 6.1: Mechanical properties and permeability of the gels, measured for various ageing, in ethanol or in decanol.

| | Solvent | Ageing | $\nu$ (-) | $E$ (MPa) | $D/\eta$ (m$^{2}$/(Pa s)) |
|---|---|---|---|---|---|
| ET025 | ethanol | 24 h | $-^{a}$ | $-^{a}$ | $-^{a}$ |
| | ethanol | 1 week | 0.21 ± 0.03 | 0.14 ± 0.01 | 1.46 ± 0.32 $10^{-11}$ |
| | decanol | 2 weeks | 0.26 | 0.16 | 1.75 $10^{-12}$ |
| ET04 | ethanol | 24 h | $-^{a}$ | $-^{a}$ | $-^{a}$ |
| | ethanol | 1 week | 0.21 ± 0.006 | 0.29 ± 0.002 | 5.02 ± 0.41 $10^{-12}$ |
| | decanol | 2 weeks | 0.23 | 0.32 | 8.15 $10^{-13}$ |
| ET06 | ethanol | 24 h | 0.23 | 0.12 | 2.16 $10^{-12}$ |
| | ethanol | 1 week | 0.23 ± 0.001 | 0.45 ± 0.05 | 2.02 ± 0.33 $10^{-12}$ |
| | decanol | 2 weeks | 0.23 | 0.53 | 2.79 $10^{-13}$ |
| ET10 | ethanol | 24 h | 0.27 | 0.66 | 2.73 $10^{-13}$ |
| | ethanol | 1 week | 0.26 ± 0.007 | 0.92 ± 0.15 | 3.96 ± 1.36 $10^{-13}$ |
| | decanol | 2 weeks | 0.25 | 0.82 | 9.19 $10^{-14}$ |
| ET15 | ethanol | 24 h | 0.27 ± 0.001 | 0.61 ± 0.03 | 2.68 ± 0.15 $10^{-13}$ |
| | ethanol | 1 week | 0.26 ± 0.01 | 1.04 ± 0.01 | 2.98 ± 0.39 $10^{-13}$ |
| | decanol | 2 weeks | 0.24 | 1.01 | 5.17 $10^{-14}$ |
| ET20 | ethanol | 24 h | 0.28 | 0.89 | 1.74 $10^{-13}$ |
| | ethanol | 1 week | 0.28 ± 0.02 | 1.21 ± 0.11 | 1.52 ± 0.12 $10^{-13}$ |
| | decanol | 2 weeks | 0.29 | 1.54 | 2.19 $10^{-14}$ |
| AT05 | ethanol | 24 h | $-^{a}$ | $-^{a}$ | $-^{a}$ |
| | ethanol | 1 week | $-^{a}$ | $-^{a}$ | $-^{a}$ |
| | decanol | 2 weeks | $-^{a}$ | $-^{a}$ | $-^{a}$ |
| AT10 | ethanol | 24 h | $-^{a}$ | $-^{a}$ | $-^{a}$ |
| | ethanol | 1 week | 0.21 ± 0.003 | 0.034 ± 0.003 | 2.02 ± 0.03 $10^{-11}$ |
| | decanol | 2 weeks | 0.26 | 0.032 | 4.53 $10^{-12}$ |
| AT15 | ethanol | 24 h | $-^{a}$ | $-^{a}$ | $-^{a}$ |
| | ethanol | 1 week | 0.21 ± 0.004 | 0.062 ± 0.004 | 1.24 ± 0.06 $10^{-11}$ |
| | decanol | 2 weeks | 0.22 | 0.071 | 2.74 $10^{-12}$ |
| AT25 | ethanol | 24 h | $-^{a}$ | $-^{a}$ | $-^{a}$ |
| | ethanol | 1 week | 0.20 ± 0.034 | 0.105 ± 0.002 | 1.03 ± 0.17 $10^{-11}$ |
| | decanol | 2 weeks | 0.20 | 0.124 | 1.46 $10^{-12}$ |
| AT40 | ethanol | 24 h | $-^{a}$ | $-^{a}$ | $-^{a}$ |
| | ethanol | 1 week | 0.18 ± 0.075 | 0.128 ± 0.014 | 0.90 ± 0.13 $10^{-11}$ |
| | decanol | 2 weeks | 0.19 | 0.150 | 1.67 $10^{-12}$ |

[a] not measurable.

$\nu$ : Poisson ratio, $E$: Young modulus, $D/\eta$: permeability over viscosity. When an error is specified, the value is the mean of two independent measurements, and the error is the standard deviation.

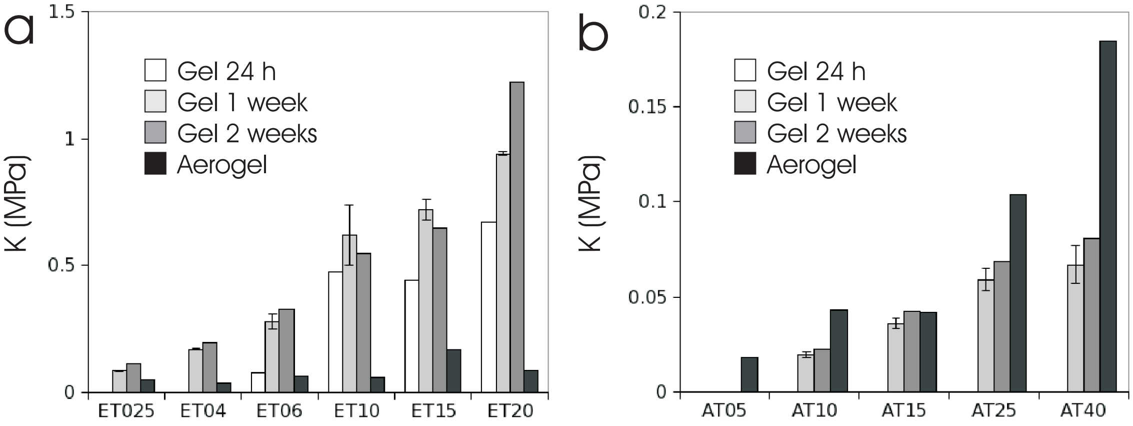

Figure 6.5: Compression moduli $K$ of (a) EDAS and of (b) AES gels and aerogels: 24 h old gels in ethanol, 1 week old gels in ethanol, 2 week old gels in decanol, and aerogels. Note the different scales in the two graphics.

The value of $K$ of the gels' skeleton, estimated from the values of $E$ and $\nu$ of Table 6.1 are plotted in Figure 6.5. The compression moduli of EDAS gels are globally larger than those of AES gels. For both EDAS and AES series, the values of $K$ increase when more co-reactant is used, as well as upon ageing. The values of the permeability are discussed below in terms of pore size.

### Pore size of the gels

If the viscosity $\eta$ of the liquid phase of the gel is known, the permeabilities $D$ can be estimated from the fitted values of $D/\eta$. A reasonable assumption is that the mother liquor of the gels has the same viscosity as ethanol, $\eta = 0.991\ 10^{-3}$ Pa.s at 30°C [Dean 1992]. For the gels washed in decanol, the value chosen for $\eta$ is the viscosity of decanol at 30°C, $\eta = 9.342\ 10^{-3}$ Pa.s [Pan *et al.* 2000].

The permeability of a monodisperse porous solid is related to its porosity $\epsilon$ and to the size of its pores $L_w$ through the Carman-Kozeny equation [Brinker & Scherer 1990]

$$D = \frac{\epsilon L_w^2}{16\kappa} \tag{6.6}$$

where the numerical value of the constant $\kappa$ depends on the detailed morphology of the solid. In the case of a material with a broad pore size distribution, the characteristic size $L_w$ that enters Equation 6.6 is the breakthrough diameter of the solid, *i.e.* the largest

Table 6.2: Estimated pore size of gels and of the xerogels.

| | $L_w^{liq/24}$ (nm) | $L_w^{liq}$ (nm) | $L_w^{dec}$ (nm) | $L_{pore}$ (nm) | $L_{cap}$ (nm) |
|---|---|---|---|---|---|
| ET025 | -[a] | 658 ± 144 | 701 | 240 | 20 |
| ET04 | -[a] | 387 ± 31 | 479 | 135 | 14 |
| ET06 | 254 | 246 ± 40 | 280 | 57 | 17 |
| ET10 | 90 | 109 ± 38 | 161 | 28 | 16 |
| ET15 | 89 | 94 ± 12 | 121 | 23 | 11 |
| ET20 | 72 | 67 ± 5 | 79 | 9 | 23 |
| AT05 | -[a] | -[a] | -[a] | 87 | 15 |
| AT10 | -[a] | 775 ± 12 | 1128 | 77 | 11 |
| AT15 | -[a] | 607 ± 30 | 878 | 76 | 23 |
| AT25 | -[a] | 554 ± 89 | 641 | 71 | 27 |
| AT40 | -[a] | 518 ± 77 | 685 | 64 | 17 |

$L_w^{liq/24}$ and $L_w^{liq}$: size of the pores determined from the permeability of the gels to their mother liquor after 24 h and 1 week, $L_w^{dec}$: size of the pores determined from the permeability of the gels to decanol after 2 weeks, $L_{pore}$: pore size of the xerogels determined from image analysis of TEM micrographs (see Table 5.2), $L_{cap}$: pore size determined from the estimated maximum capillary pressure.
[a]: not measurable.

size such that the set of all pores with a size larger than $L_w$ forms a percolating network through the macroscopic solid [Katz & Thompson 1986].

In the particular case of a monodisperse solid with a columnar morphology, and if $L_w$ is the width of the opening window between neighbouring columns, the following approximate relation holds [Scherer 1994a; Scherer *et al.* 1996]

$$\kappa = 1 + 6.05(1-\epsilon)^{1/2} - 8.60(1-\epsilon) + 6.56(1-\epsilon)^{3/2} \tag{6.7}$$

where $\epsilon$ is the porosity of the material. Assuming that the solid phase of the gel has the same density as dense silica, 2 $cm^3/g$, and that the volume of the gel is identical to that of its precursor solution, the specific volume of all EDAS and AES gels is estimated from their composition to be close to 15 $cm^3/g_{SiO2}$. Using this value, the porosity of all AES and EDAS gels is found to be approximately $\epsilon = 0.97$. The size of the pores of EDAS and AES gels, estimated from the permeability of the gels, using Equations 6.6 and 6.7 with $\epsilon = 0.97$ are reported in Table 6.2.

The pore sizes estimated from the permeability of the mother liquor $L_w^{liq}$ are system-

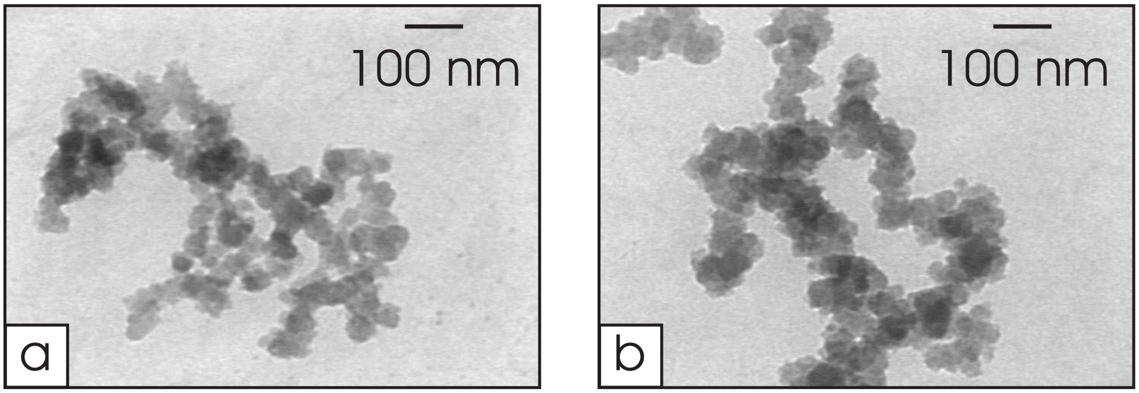

Figure 6.6: Transmission electron micrographs of fragments of EDAS sample ET025: (a) aerogel and (b) xerogel.

atically smaller than those estimated from the permeability of decanol $L_w^{dec}$. A possible explanation is that the viscosity of the mother liquor is slightly larger than that of ethanol. This could indeed be the case because partially condensed silica species are likely to be present in the mother liquor and contribute to increasing its viscosity above that of ethanol. The mean relative error observed on $L_w^{liq}$ is about 15%; the relative error on $L_w^{dec}$ is presumably the same.

### 6.3.2 Textural characterization of the aerogels

#### Electron microscopy

Figure 6.6a displays a transmission electron micrograph of sample ET025 dried in supercritical $CO_2$(aerogel). For comparison purposes, a micrograph obtained on the corresponding xerogel (see Chapter 5) is displayed in 6.6b.

The width of the filaments in the ET025 aerogel is smaller than in the ET025 xerogel. No clear difference is detected from microscopy between the other aerogels and corresponding xerogels. This could be due to the preparation of the samples for microscopy, that involves the evaporation of the ethanol in which the samples are dispersed, *i.e.* a subcritical drying.

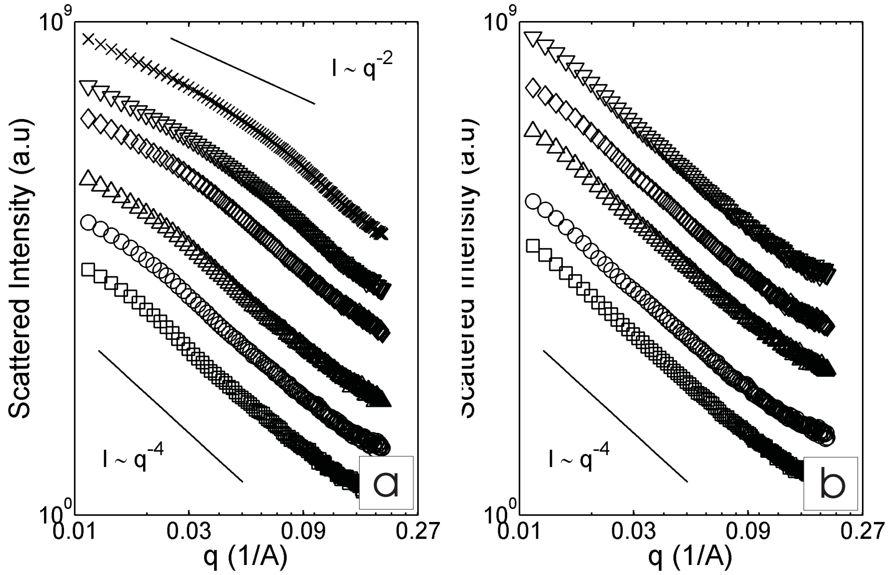

Figure 6.7: SAXS patterns of (a) EDAS aerogels ET025 (□), ET04 (◯), ET06 (△), ET10 (◊), ET15 (▽), and ET20 (×), and (b) AES aerogels AT05 (□), AT10 (◯), AT15 (△), AT25 (◊) and AT40 (▽). The curves are arbitrarily shifted vertically.

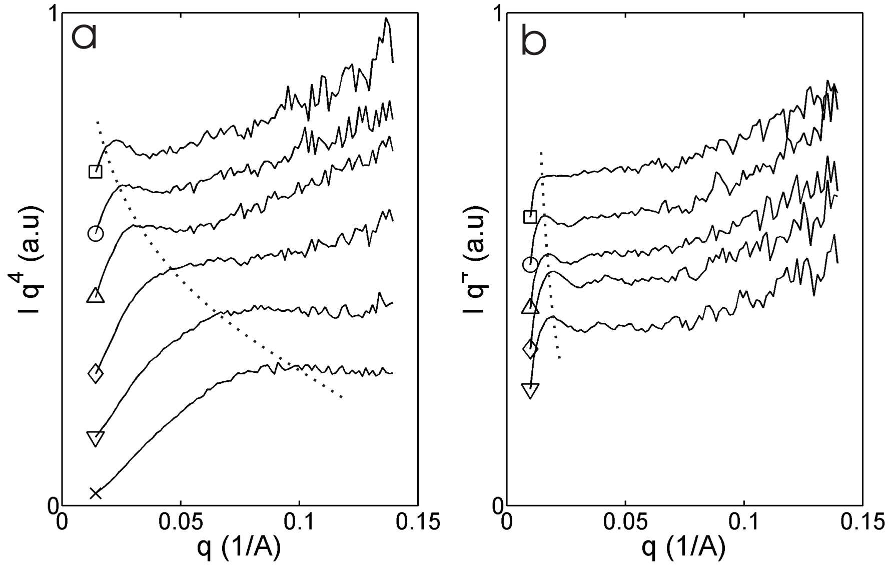

Figure 6.8: Kratky-Porod plots of the SAXS patterns of (a) EDAS aerogels ET025 (□), ET04 (◯), ET06 (△), ET10 (◊), ET15 (▽), and ET20 (×), and (b) AES aerogels AT05 (□), AT10 (◯), AT15 (△), AT25 (◊) and AT40 (▽). The curves are arbitrarily shifted vertically.

Table 6.3: Textural characteristics of EDAS and AES aerogels.

| | $L_{KP}$ (nm) | $C_{BET}$ (-) | $S_{BET}$ (m$^2$/g) | $V_0^a$ (cm$^3$/g) | $K_0^a$ (MPa) | $m$ (-) |
|---|---|---|---|---|---|---|
| ET025 | 27 | 240 | 287 | 14 | 0.03 | 4.9 |
| ET04 | 24 | 121 | 307 | 20 | 0.11 | 4.0 |
| ET06 | 20 | 145 | 245 | 15 | 0.08 | 3.9 |
| ET10 | -[a] | 97 | 298 | 13 | 0.10 | 3.4 |
| ET15 | 8 | 76 | 348 | 9 | 0.11 | 3.6 |
| ET20 | 6 | 56 | 386 | 9 | 0.17 | 3.0 |
| AT05 | -[a] | 226 | 183 | 11 | 0.01 | 5.0 |
| AT10 | 40 | 253 | 119 | 12 | 0.02 | 4.9 |
| AT15 | 37 | 87 | 127 | 10 | 0.02 | 4.3 |
| AT25 | 31 | 61 | 123 | 7 | 0.03 | 3.9 |
| AT40 | 31 | 56 | 122 | 8 | 0.05 | 3.8 |

$L_{KP}$: Kratky-Porod length, $C_{BET}$ and $S_{BET}$: BET constant and specific surface area, $V_0^a$: specific volume, $K_0^a$: elastic compression modulus, $m$: plastic hardening exponent.
[a]: not measurable.

### Small Angle X-ray Scattering

The SAXS patterns of EDAS and of AES aerogels are plotted in Figure 6.7. The patterns are qualitatively similar to those of the corresponding xerogels (Figure 5.5 on page 91), and their qualitative analysis follows the same lines as section 5.3.3.

At large angles, the patterns exhibit a power law scattering with exponent $-4$, characteristic of structures with a clear-cut surface [Schmidt 1991]. At low angles the patterns exhibit a convex curvature. It can be put in evidence by a Kratky-Porod plot, obtained by plotting $Iq^4$ against $q$ (Figure 6.8). The plots exhibit a local maximum at low angles, at a position $q_{max}$ that is converted to a characteristic length $L_{KP}$ through the relation $L_{KP} = 2\pi/q_{max}$. The values of $L_{KP}$ are reported in Table 6.3.

### Nitrogen adsorption

Nitrogen adsorption-desorption isotherms of the EDAS and AES aerogels are reported in Figure 6.9. Globally the isotherms resemble those measured on the xerogels (see Figure 5.4 on page 89); they are fitted with the BET model and the obtained values of $C_{BET}$ and of the specific surface area $S_{BET}$ are reported in Table 6.3.

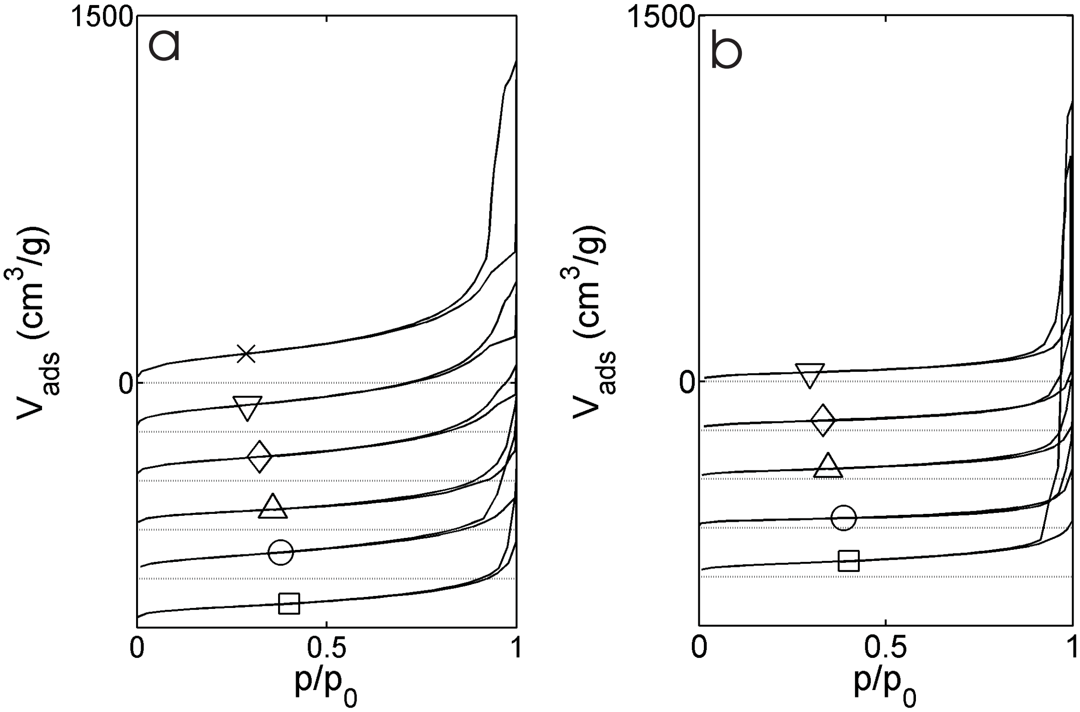

Figure 6.9: Nitrogen adsorption-desorption isotherms of (a) EDAS aerogels ET025 (□), ET04 (◯), ET06 (△), ET10 (◊), ET15 (▽), and ET20 (×), and (b) AES aerogels AT05 (□), AT10 (◯), AT15 (△), AT25 (◊) and AT40 (▽). The curves are arbitrarily shifted vertically.

The BET constant, representative of the energy of interaction between the nitrogen molecule and the adsorbent surface undergoes a marked decrease upon increasing the amount of any co-reactant. A similar trend was observed for the xerogel, and it was attributed to the covering of the surface by the organic moieties of the co-reactant molecules. The specific surface of the EDAS aerogels globally increase when more EDAS is used. For small amounts of EDAS, $S_{BET}$ is larger for the aerogels that for the xerogels (compare with Table 5.3 on page 88). For large amounts of EDAS, $S_{BET}$ of the aerogel and xerogel are similar. In the case of AES samples, the specific surface area of the aerogels undergo a marked decrease when passing from AT05 to AT10. For all AES samples, the values of $S_{BET}$ measured on the xerogels and on the aerogels are almost identical.

### Mercury Porosimetry

When mercury porosimetry is applied to aerogels, the samples are generally compressed rather than intruded by the mercury [Pirard *et al.* 1995; Scherer *et al.* 1995]. For EDAS and AES xerogels and aerogels, a two stage phenomenon is observed: the samples are first compressed at low pressure, and then intruded at higher pressure. This has already been reported in the case of AES and EDAS xerogels [Alié *et al.* 1999; 2001]; to our knowledge it is the first time that a two-stage compression-intrusion mechanism is reported for aerogels, for which pure compression is expected [Scherer *et al.* 1997]. Only the low pressure part of the mercury porosimetry curves, in which pure compression occurs, is used in the present study. The data provide information about the way in which the material's porosity resists a given pressure.

The data are reported in Figure 6.10 as the specific volume of the sample $V(P)$ submitted to a pressure $P$. The curves are obtained by subtracting the mercury volume variation $V_{Hg}(P)$ -measured by the mercury porosimeter, and normalized by the mass of the sample- from the specific volume of the sample $V_0$, when no pressure is exerted:

$$V(P) = V_0 - V_{Hg}(P) \tag{6.8}$$

In the case of the xerogels, $V_0$ is measured by mercury pycnometry; the values are reported as $\rho_b = 1/V_0$ in Table 5.3 on page 88. The aerogels are so soft and fragile that pycnometry is not reproducible. The specific volume $V_0^a$ of the aerogels is therefore estimated by

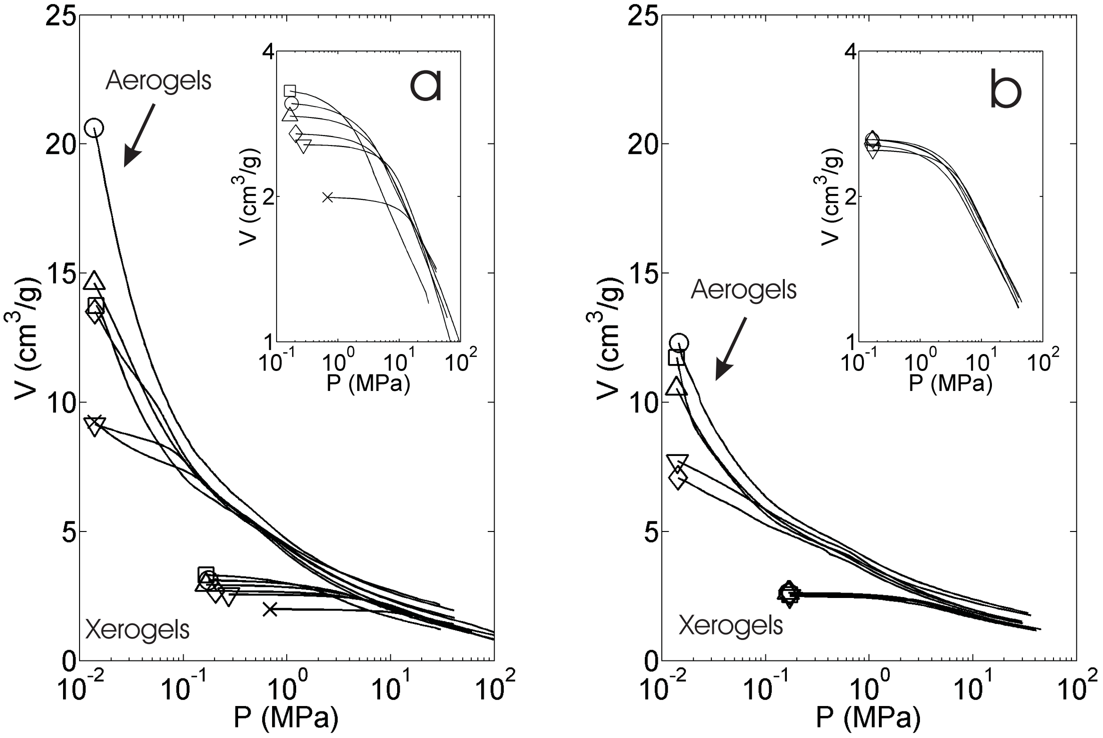

Figure 6.10: Volume-Pressure curves of (a) EDAS aerogels and xerogels ET025 (□), ET04 (◯), ET06 (△), ET10 (◊), ET15 (▽), and ET20 (×), and (b) AES aerogels and xerogels AT05 (□), AT10 (◯), AT15 (△), AT25 (◊) and AT40 (▽), measured by mercury porosimery. The insets are magnified views of the xerogels' compression curves.

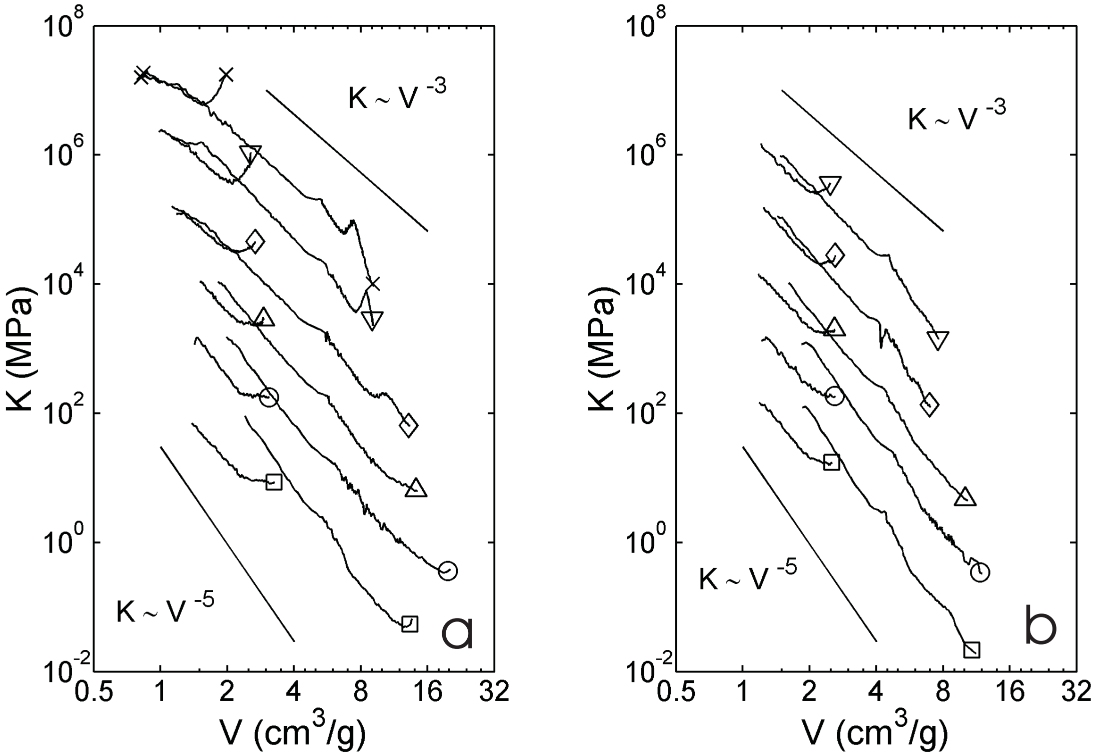

Figure 6.11: Compression modulus versus specific volume for the aerogels and xerogels: (a) EDAS samples ET025 (□), ET04 (○), ET06 (△), ET10 (◊), ET15 (▽), and ET20 (×), and (b) AES samples AT05 (□), AT10 (○), AT15 (△), AT25 (◊) and AT40 (▽), obtained from mercury porosimery. The curves of ET025 and AT05 aerogels and xerogels are not shifted vertically; the curves of the other samples are shifted vertically by successive powers of 10.

assuming that the aerogels reach the same density as the corresponding xerogels when they are compressed to the highest pressure reached in the porosimeter (200 MPa). This is equivalent to matching the end points of the $V(P)$ curves of the corresponding aerogels and xerogels. The values of $V_0^a$ are reported in Table 6.3.

Globally, for both EDAS and AES aerogels, the $V(P)$ curves exhibit a continuous decay over the entire pressure range. On the contrary, the $V(P)$ curves of the xerogels exhibit first a plateau on which the samples volume is but slightly affected by the pressure, followed by a progressive compression when a yield pressure is exceeded, as clearly visible in the insets of Figure 6.10. Beyond that pressure, the compression curves of the aerogels and of the xerogels run almost parallel to each other.

To compare the results of mercury porosimetry with beam bending measurements, the compression curves are expressed through the compression modulus, $K$, defined as

$$K(P) = -V(P)\frac{dP}{dV} \tag{6.9}$$

where $V(P)$ is obtained by Equation 6.8. In the case of the EDAS and AES aerogels (Figure 6.11), a hardening occurs upon compression, by which $K$ increases when $V$ decreases. The compression moduli of the xerogels are globally close to those of the corresponding aerogels, when they are compressed to the same volume. The xerogels synthesized with a small amount of co-reactant are, however, less stiff than the corresponding aerogels at the same volume. For instance, at $V \simeq 3$ cm$^3$/g, the value of $K$ of the ET025 xerogel is lower than that of the ET025 aerogel (Figure 6.11a).

The experimental curves of $K$ *vs.* $V$ are fitted with the following function [Scherer *et al.* 1995]

$$K = \begin{cases} K_0 & \text{for } V > V_y \\ K_0\,(V_y/V)^m & \text{for } V < V_y \end{cases} \tag{6.10}$$

where $V_y$ is the yield volume, above which the deformation is elastic, and below which the material undergoes a plastic deformation with a progressive hardening of the material. The fit of the data is illustrated by the solid lines in Figure 6.12, on the first and last samples of EDAS and AES series. As no elastic region is seen in the compression curves of the aerogels (Figure 6.11), the following empirical relation [Smith *et al.* 1995] is used to determine $V_y$

$$V_y = V_0/\exp\left(\frac{1}{m}\right) \tag{6.11}$$

where $V_0$ is the specific volume of the uncompressed sample, set to be identical to that of the gel, *i.e.* $V_0 = 15$ cm$^3$/g. The fitted values of $m$ and of $K_0$ are reported in Table 6.3, the latter parameter is labelled $K_0^a$. It is also plotted in Figure 6.5 together with the beam bending results. The initial compression moduli $K_0^a$ of AES aerogels are globally close to those of the corresponding gels. On the contrary, in the case of EDAS samples, the gels seem to be significantly stiffer than the corresponding aerogels.

Solving Equation 6.9 as a differential equation, with Equation 6.10, leads to [Scherer 1997]

$$P = K_0 \log\left(\frac{V_0}{V_y}\right) + \frac{K_0}{m}\left[\left(\frac{V_y}{V}\right)^m - 1\right] \tag{6.12}$$

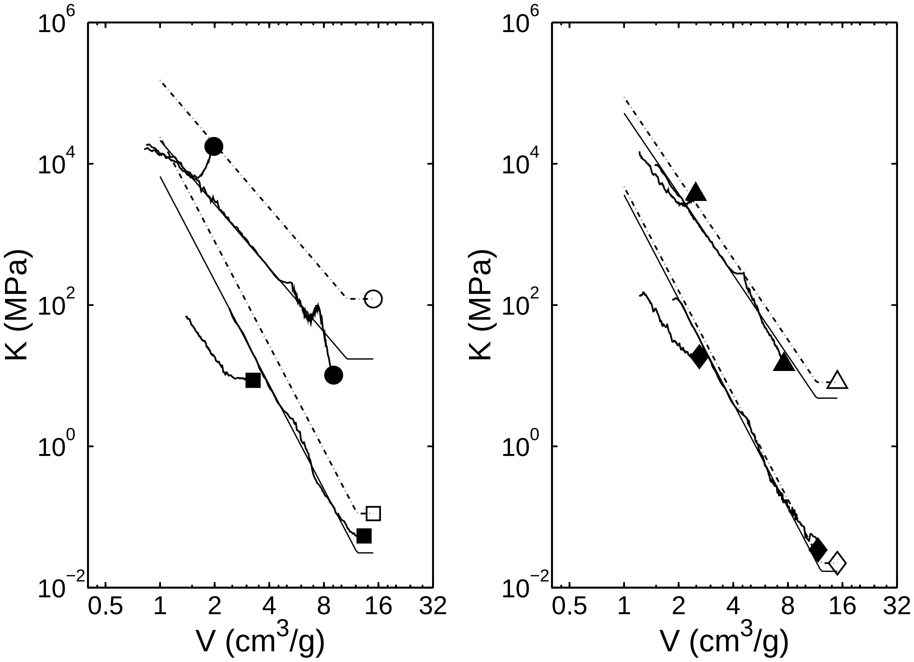

(a) EDAS (b) AES

Figure 6.12: Modelling of the compression curves of the samples: (a) EDAS samples ET025 (■) and ET20 (●), and (b) AES samples AT10 (♦) and AT40 (▲). Full symbols are the compression curves measured by mercury porosimetry on the aerogels and xerogels; open symbols are the compression moduli derived from the beam-bending of the gels. The dotted line corresponds to Equations 6.10 and 6.11 with the value of $K_0$ of the gels; the solid line is a fit of the compression curves of the aerogels with Equations 6.10 and 6.11. The curves of the second sample in each series are shifted vertically by a factor 100.

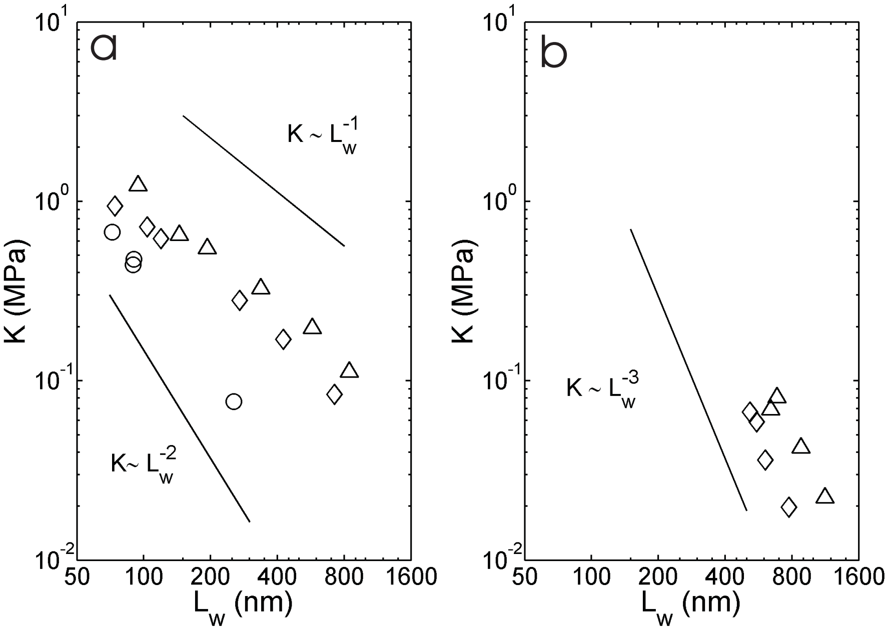

Figure 6.13: Compression modulus of the gels $K$ against pore size $L_w$, for (a) EDAS and (b) AES samples: (○) 24 h old gels in ethanol, (◇) 1 week old gels in ethanol and (△) 2 week old gels in decanol.

for $V < V_y$. This equation is used in the discussion to estimate the pressure that has to be applied to a sample to compress it to any given specific volume $V$.

## 6.4 Discussion

### 6.4.1 General observations about the mechanical properties of the gels

Assuming that the skeleton of the gels is made of dense $SiO_2$, all EDAS and AES gels have the same solid fraction, close to 3%. Nevertheless, their Young moduli $E$ increase by a factor 50 from AT10 to ET20 (see Table 6.1), and the pore sizes $L_w^{dec}$ decrease by more than a factor 10 between the same samples (see Table 6.2). The relation between compression modulus and pore size for EDAS and AES gels is plotted in Figure 6.13.

It can be be shown that for a material with a given microstructure, only the density has an influence on the macroscopic mechanical properties such as $K$, and not the pore size [Gibson & Ashby 1988; Roberts & Garboczi 2000]. As all EDAS and AES gels have the same density, the variation of $K$ with $L_w$ (Figure 6.13) points at a qualitatively different microstructure of the gels when more co-reactant is used. Low values of $K$ could be associated with a low connectivity of the struts that form the gel's skeleton. A similar relation exists between loss of connectivity and loss of elastic modulus for trabecular[1] bones [Kinney & Ladd 1998]. Under this hypothesis, when passing from ET20 to ET025, and from AT40 to AT10, the connectivity of the struts becomes lower. For even lower amount of AES the struts exist but they are completely disconnected (sample AT025, Figure 5.3 on page 85), and the sample is indeed liquid.

The different connectivity of the struts in the various samples is also supported by the values of the hardening exponent $m$ (Table 6.3). Perfectly connected cellular materials are characterized by $m = 2$ [Gibson & Ashby 1988]. A larger value of $m$ is obtained when the connectivity of the struts increases when the material is compressed. Typical values for gels and aerogels are $3 < m < 4$, as reviewed by Ma *et al.* [2000]. The latter values can be reproduced from finite element modelling of various geometrical models of gels, such as aggregates of particles [Ma *et al.* 2002b] or Gaussian random fields [Roberts & Garboczi 2000]. Values of $m$ larger than 4 generally hint at the presence of dead branches that contribute to the density but not to the mechanical stiffness of the material [Ma *et al.* 2000]. The values of $m$ obtained for EDAS and AES aerogels evolve from *ca* 3 to 5 when decreasing the amount of co-reactant (Table 6.3). This trend is compatible with a lower connectivity of the struts when less co-reactant is used.

### 6.4.2 Macroscopic shrinkage during the drying of the gels

The shrinkage that a gel undergoes during its evaporative drying results from a balance between the capillary forces that put the gel's skeleton in compression, and the mechanical stiffness of the skeleton that more or less prevents its collapse [Brinker & Scherer 1990; Smith *et al.* 1995] (see Figure 1.2 on page 6).

A quantitative theory for the shrinkage of a gel during its desiccation has been developed for the case where (i) the hardening of the gels obey Equation 6.10, and (ii) the pore size decreases proportionally to the pore volume [Smith *et al.* 1995]. The latter relation is supported by experimental evidence for a large variety of gels, including silica gels [Smith *et al.* 1995] and resorcinol-formaldehyde organic gels [Scherer *et al.* 1996]. Expressing the pore volume as $V - 1/\rho_s$, where $V$ is the specific volume of the gel and $\rho_s$ is the density of its solid phase, the relation between pore size and volume is written

---

[1] In biology, a trabecula is a synonymous for what is called a strut throughout this thesis: it is rod-like structure that generally has a mechanical function.

$$L_w(V) = L_w^0 \frac{V - 1/\rho_s}{V_0 - 1/\rho_s} \tag{6.13}$$

where $L_w^0$ is the pore size of the uncompressed gel, for $V = V_0$. The final specific volume of the gel $V$ after evaporative drying is predicted to be [Smith *et al.* 1995]:

$$V = V_y/\mathcal{P}^{1/(m-1)} \tag{6.14}$$

where $m$ is the plastic hardening exponent $m$, and $\mathcal{P}$ is a dimensionless number, defined as the ratio of the capillary pressure to the mechanical stiffness of the gel's skeleton. Namely,

$$\mathcal{P} = \frac{4\gamma\cos(\theta)m}{L_w^0 K_0} \frac{V_0 - 1/\rho_s}{V_y} \tag{6.15}$$

where $\gamma$ is the surface tension of the liquid that fills the pores of the gel, and $\theta$ is its contact angle with the solid phase of the gel.

The values of $\mathcal{P}$ of EDAS and AES gels are estimated with the following values: $\gamma = 19$ mN/m, typical of ethanol at 60°C [Dean 1992], $\theta = 0$, $m$ taken from Table 6.3, $L_w^0 = L_w^{dec}$ from Table 6.2, $V_0 = 15$ cm$^3$/g, $\rho_s = 2$g/cm$^3$, $V_y$ estimated from Equation 6.11, and $K_0$ determined from beam-bending of the gels using Equation 6.5. This particular choice of $K_0$ leads to a modelling of the compression modulus of the gels that extrapolates the beam-bending measurements to lower specific volumes $V$, by assuming a power law dependence with the same exponent as the aerogels' (dashed lines in Figure 6.12). For EDAS gels, $2.5 < \mathcal{P} < 4.5$, and for AES gels, $5 < \mathcal{P} < 14.5$. The final specific volumes of the xerogels estimated from Equation 6.14 are plotted in Figure 6.14 against their actual specific volumes. The analysis leads to a severe overestimation, by a factor 2, of the specific volumes of the EDAS and AES xerogels.

A possible origin for the underestimation of the shrinkage of the gels during desiccation could be an overestimation of their mechanical stiffness. This would not be surprising from Figure 6.5: the compression modulus of EDAS gels is larger than that of the corresponding aerogels. Furthermore, for the samples with a large amount of EDAS, the compression

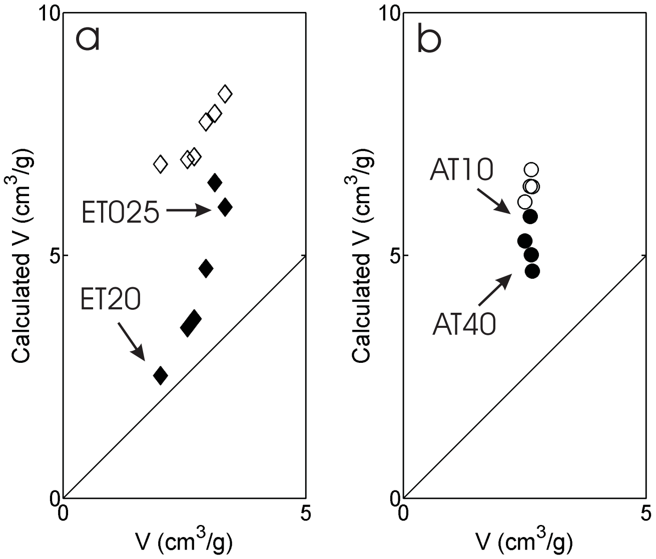

Figure 6.14: Specific volumes of the xerogels calculated from Equation 6.14 against actual specific volumes of the xerogels: (a) EDAS samples and (b) AES samples. The open symbols are calculated from the extrapolation of the compression moduli of the gels (dashed lines in Figure 6.12); the full symbols are calculated from the compression moduli of the aerogels (solid lines in Figure 6.12).

modulus of the xerogels undergo a significant decrease at the beginning of the compression (see *e.g.* samples ET15 and ET20 in Figure 6.11a). A similar decrease in stiffness upon compression has been reported for a large variety of xerogels and aerogels [Gross & Fricke 1992; Perin *et al.* 2004]. If the gels' skeleton itself underwent a similar initial decrease in stiffness, the effect could have occurred at a pressure too low to be evidenced by mercury porosimetry on the aerogels. To test this hypothesis, the compaction of the gels during the drying is estimated using Equations 6.15 and 6.14, with the compression curves of the aerogels (solid lines in Figure 6.12). As plotted in Figure 6.14, the agreement with the theory is now reasonable for the samples synthesized with a large amount of EDAS.

The samples with a small amount of EDAS and all AES samples undergo an abnormally large compaction compared to the prediction of Equation 6.14. For these samples, it must therefore be admitted that the pore size determined by Equation 6.13 leads to an underestimation of the capillary pressure. To get an insight into this issue, the pore size determined from the permeability data $L_w^{dec}$ is compared in Figure 6.15 with: (i) the size

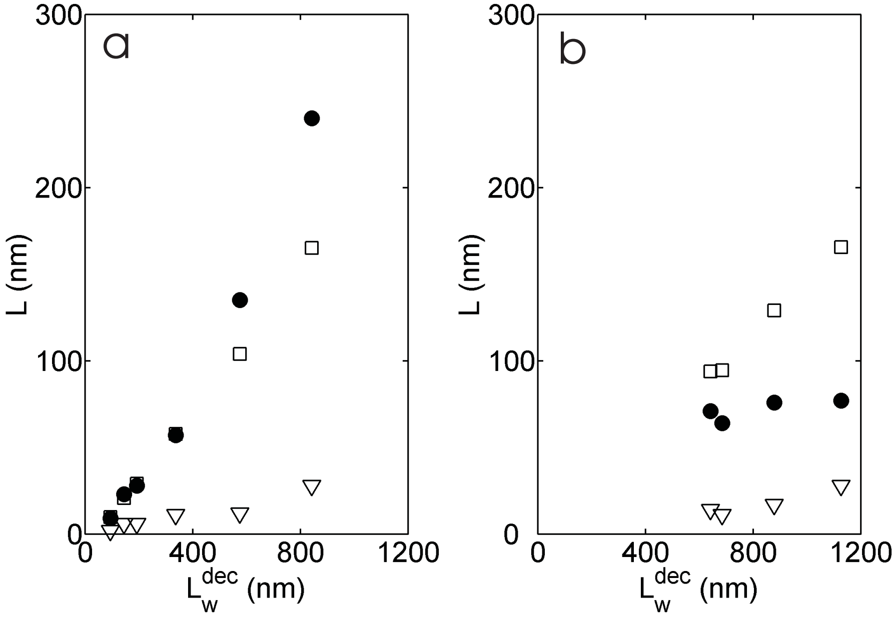

Figure 6.15: Comparison of the size of largest pores in the xerogels $L$ and in the gels $L_w^{dec}$ for (a) EDAS samples and (b) AES samples: (●) $L_{pore}$ measured from TEM (Table 5.2), (□) $L_w$ estimated from Equation 6.13 with $L_w^0 = L_w^{dec}$, and (▽) $L_{cap}$.

of the macropores of the xerogels $L_{pore}$ (Table 6.2), (ii) the size $L_w$ estimated by correcting $L_w^{dec}$ with Equation 6.13, and (iii) the size $L_{cap}$ of the pores that would lead to a capillary pressure sufficient to compress the gels to the actual density of the xerogels. To estimate $L_{cap}$, the capillary pressure $P_c$ is estimated by setting $V$ equal to the measured specific volume of the xerogels in Equation 6.12. The corresponding pore size is estimated as $L_{cap} = 4\gamma/P_c$, which results from Laplace's equation (Equation 1.2) with $\theta = 0$; it is reported in table 6.2.

A striking difference between EDAS and AES gels is that $L_w^{dec}$ and $L_{pore}$ are strongly correlated for EDAS samples but not for AES samples (Figure 6.15). This means that the largest pores of EDAS gels shrink proportionally to their volume, while the pores of AES gels collapse during the drying until they reach a size of *ca* 70 nm, independently of their initial size. The proportional shrinkage of EDAS gels is agreement with $L_{pore}$ being close to $L_w$ (Figure 6.15a). For the EDAS samples with the largest pores $L_w < L_{pore}$, which is expected because $L_w$ is a breakthrough size that depends on the connectivity of the pores (see the discussion of Equation 6.6). On the contrary, for AES samples $L_{pore}$ is systematically smaller than $L_w$. As this is not physically possible, Equation 6.13 clearly does not apply to AES gels.

For most samples $L_{pore}$ and $L_w$ are significantly larger than $L_{cap}$ (see Figure 6.15). This means that, in addition to the shrinkage of the pores, the drying process lowers the connectivity of the porous network. Indeed, at the critical point of drying (see Figure 1.2 on page 6), the size of the pores through which the drying front has to pass to invade the material porosity is of the order of $L_{cap}$, and it is smaller than $L_{pore}$ (Table 6.2). In theory, an alternative estimation of $L_{cap}$ could be obtained through the analysis of the desorption branch of the nitrogen adsorption isotherms of the xerogels [Smith *et al.* 1995]. In practice, however, owing to the large pore size in the xerogels, the samples' porosity does not fill with liquid nitrogen, even close to the saturation pressure, and no hysteresis is detected (see section 5.4.1 on page 92).

### 6.4.3 Effect of drying on the gels' nanostructure

When the gels stop shrinking macroscopically, the drying front enters the materials' largest pores that form a percolating network through the macroscopic material. The shrinkage can continue at a smaller scale.

Evidence of shrinkage of the materials' nanostructure is found by comparing the specific surfaces $S_{BET}$ of the aerogels (Table 6.3) and corresponding xerogels (Table 5.3 on page 88). For samples with low amounts of EDAS, $S_{BET}$ is significantly smaller for the xerogel than for the aerogel. This points at a small scale compaction of the material during its evaporative drying, by which the smallest structures that most contribute to $S_{BET}$ come in contact. In the case of ET025, for which the differences in $S_{BET}$ are the most marked, the idea of such a compaction is in agreement with microscopy (Figure 6.6). SAXS also confirms that $L_{KP}$ is smaller for the aerogel than for the xerogel, for samples with a low amount of EDAS (Table 6.3 and Table 5.2 on page 87).

Globally, the findings for EDAS aerogels are in agreement with the idea proposed in section 5.4.1 on page 92, according to which the filaments of the xerogels can be though of as condensates of smaller structures. Increasing the amount of EDAS results in their progressive merger. This view is confirmed by the observation that the differences in $L_{KP}$

and in $S_{BET}$ between aerogels and xerogels become smaller when more EDAS is used (Table 6.3, Table 5.2 on page 87, and Table 5.3 on page 88). For AES samples the differences in $L_{KP}$ and $S_{BET}$ between aerogels and xerogels are far less marked. This tends to prove that the structure of the filaments is less affected by desiccation in AES gels than in EDAS gels.

The effect of desiccation on the small-scale structure of the gels could account for the different values of $K$ for the xerogels and aerogels (Figure 6.11). The $K$ *vs.* $V$ curves of the xerogels with low amounts of EDAS are below the corresponding curves of the aerogels. This means that the xerogels are less stiff than the aerogels when they are compressed to the same macroscopic density. This is not the case for the samples with large amounts of EDAS, for which the $K(V)$ curves of the aerogels and xerogels coincide at low volumes. The same trend exists for AES samples. The reason why the shrinkage of the filaments should lead to a lower mechanical stiffness of the macroscopic solid is understandable from the fact the main mechanism of deformation of the filaments is presumably their bending [Ma *et al.* 2002b]. The bending rigidity of a filament depends on the moment of inertia of its cross section [Landau & Lifshitz 1959], that necessarily decreases when its shrinks[2].

## 6.5 Conclusion

Beam bending measurements performed on both EDAS and AES gels reveal the presence of very large pores, the size of which depends on the amount of EDAS and of AES. In both series of samples, a larger amount of co-reactant results in smaller pores. The findings are in qualitative agreement with the observations done on EDAS xerogels; they are in contradiction with observations done on AES xerogels, in which the largest pores all have a size close to 70 nm, independently of the amount of AES. This suggests a qualitatively different behaviour of EDAS and of AES gels during desiccation. The largest pores of the former simply shrink, but the largest pores of the latter collapse during the evaporative drying.

At the nanometer scale, the gels skeleton also undergoes a compaction during desiccation that is more pronounced for the samples with a low amount of co-reactant. This results from the comparison of all the characterization data obtained on xerogels and aerogels. It is also compatible with the different mechanical stiffness of the xerogels and aerogels when they are compressed to the same density.

---

[2] This effect is rationalized by civil engineers; the bending rigidity of the Eiffel tower seen as a beam would be lower if all its constitutive elements were assembled into a single beam with a dense cross-section.

# Chapter 7

# General findings of the thesis

## 7.1 Introduction

The present work was aimed at analysing the physicochemical phenomena responsible for the microstructure of xerogel catalysts and of metal-free xerogels synthesized by the cogelation method (Chapter 1). This requires a thorough characterization of the final xerogel materials, an understanding of the structural development of the gels as well as the assessment of the way in which the structure of the gels is modified by desiccation.

The question of the dispersion of metallic particles in Pd/$SiO_2$ catalysts synthesized by co-reacting a complex of palladium with 3-(2-aminoethylamino)propyltriethoxysilane (EDAS-Pd) with TEOS, was addressed in Chapter 2. Electron tomography coupled with digital image analysis shows that the metal particles are dispersed in the middle of the struts that form the silica skeleton, the distances between them being comparable to the width of the struts. The almost regular dispersion of the metal is reminiscent of the nucleation-growth-aggregation model initially proposed by Heinrichs *et al.* [1997b] to explain the formation of cogelled samples[1].

Chapter 3 investigated *in situ* the formation for the nanometer structure of the Pd/$SiO_2$ cogelled samples using time-resolved SAXS. It appears from the reported measurements that the nanostructure of Pd/$SiO_2$ gels forms *via* a reaction-induced phase separation: the hydrolysis and condensation of the silica precursors bring them into a state where they are no longer miscible with the solvent. This triggers a demixing process at the nanometer scale.

---

[1] See Figure 1.5 on page 11.

In Chapter 4, time-resolved SAXS was used to analyse the formation of metal-free cogelled samples synthesized with TEOS and two different co-reactants, namely EDAS and 3-aminopropyltriethoxysilane (AES). The same reaction-induced phase separation is observed as described in Chapter 3. For comparison purposes, the formation of pure silica gels synthesized by the Acid/Base method was also investigated, and the well documented aggregation process is observed by time-resolved SAXS.

In order to understand the impact of phase separation on the structure of the gels, the microstructure of EDAS and AES cogelled xerogels was analysed in Chapter 5. From the characterization of the xerogels, the general mechanism that we propose for the development of EDAS and AES gels is a double reaction-induced phase separation. In agreement with a scenario of visco-elastic phase separation [Tanaka 1996], a primary phase separation occurs *via* the nucleation and growth of vacuole-like solvent-rich domains, that concentrates the silica in a phase with the morphology of a network of struts. The phase separation evidenced by *in situ* SAXS in Chapter 4 is a secondary phase separation that is responsible for the substructure of the struts.

Chapter 6 deals with the large scale structure of the EDAS and AES gels, and with the impact of dessication of the gels' microstructure. Beam-bending measurements were performed that enable one to determine the elastic properties of the gels's skeleton, and the size of their largest pores. The gels were also dried in supercritical $CO_2$, and the obtained aerogels were characterized. The behaviour of AES gels during desiccation differs qualitatively from that of EDAS gels: the largest pores of EDAS gels shrink proportionally to their volume, and the largest pores of AES collapse until they reach the size of 70 nm, independently of their initial size. At a smaller scale, the struts of both EDAS and AES gels shrink during desiccation, more marked so for the gels with low amounts of co-reactant.

The present chapter summarizes some important findings about the gels, aerogels and xerogels investigated in this thesis, and attempts to analyse them coherently in terms of their microstructure and formation mechanism.

## 7.2 Microstructure of the gels

At small scale, from 3 nm to 60 nm[2], the characterization of the gels was done using SAXS. The position of the maximum in the SAXS patterns provides the characteristic size of the scattering structure, that is found to be close to 40 nm for all investigated gels[3]; the asymptotic exponents provide qualitative information about the inner structure of the objects, either loose as expected for polymers in solution, or dense.

As assessed by electron microscopy of both xerogels[4] and aerogels[5], EDAS gels are made of a network of struts. The large scale characterization of the gels was conducted using beam bending. The permeability measurements[6] probe the largest pores that form a percolating network through the macroscopic materials. Increasing the amount of EDAS results in smaller pores in the gel[7]. Moreover, the different values of the elastic moduli of the gels, despite their having the same density, hint at a different connectivity of the struts[8]. The struts seem to progressively disconnect when less EDAS is used.

Figure 7.1a sketches the large-scale microstructure of EDAS gels. The network of struts in gels with large amounts of EDAS is represented in the figure as a cellular structure. The image was generated by dropping seeds randomly according to a Poisson process [Serra 1982], and by calculating their Voronoi cells. The latter correspond to the locus of all points closer to a given Poisson seed than to any other [Ohser & Mücklich 2000]. Each strut in Figure 7.1a2 is the boundary between two neighboring Voronoi cells. To obtain larger pores, Figure 7.1a1 was obtained by dropping less Poisson seeds; to lower the connectivity of the struts, one strut out of three was removed randomly.

As the density of all EDAS samples is the same, there should exist a relation between the length of struts and their width. In the case of a cubic array of cylindrical filaments [Smith *et al.* 1995], the following approximate relation holds between the width $a$ of the

---

[2] See Section 4.2.2 on page 60.

[3] See Table 3.1 on page 38, and Table 4.1 on page 59.

[4] See Figure 5.2 on page 84.

[5] See Figure 6.6 on page 112.

[6] See Section 6.3.1 on page 104.

[7] See Table 6.2on page 111.

[8] See Section 6.4.1 on page 121.

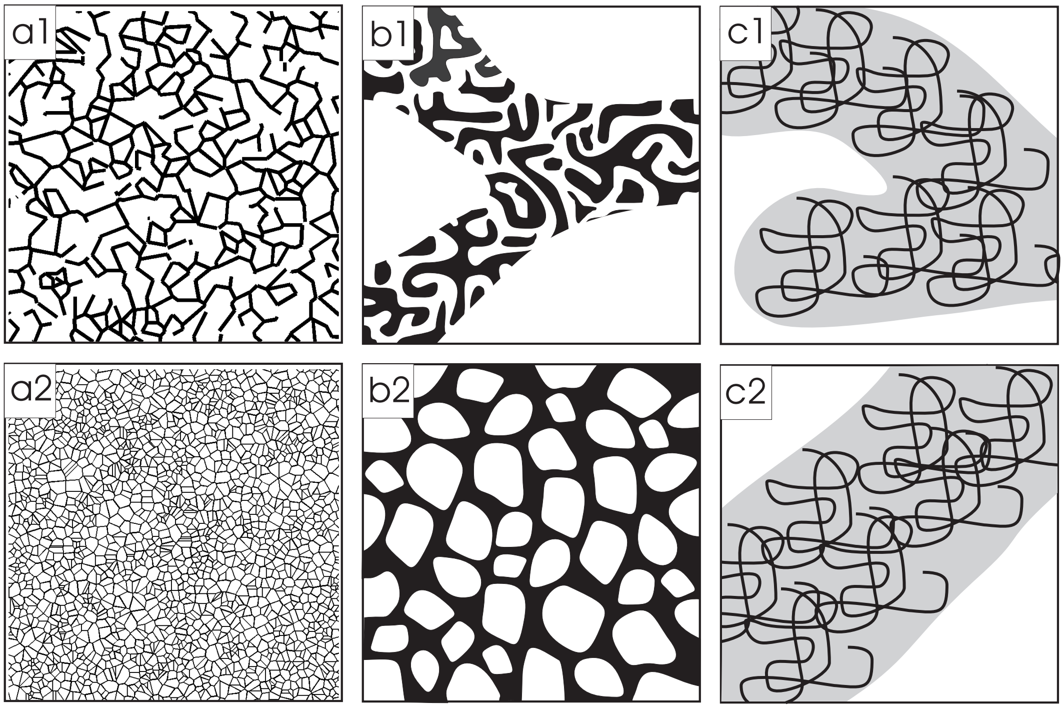

Figure 7.1: Sketch of (a) large scale, (b) intermediate scale and (c) small scale structure of the gels synthesized with small amounts (top) and large amounts (bottom) of EDAS.

filaments and their lengths $l$

$$\frac{a}{l} \simeq \frac{0.925}{3/\sqrt{1-\epsilon}-1} \tag{7.1}$$

where $\epsilon$ is the porosity of the network. To compare the microstructure of EDAS gels with Equation 7.1, the following values were used: the length $l$ of the struts is assimilated to the pore size $L_w^{dec}$ determined from permeability in decanol[9], and the width of the struts $2a$ is assimilated to $L_F$ determined from image analysis of the xerogels[10]. The latter choice is justified by the fact that the amount of silica per unit length of filament is presumably not modified by desiccation. Using $\epsilon = 0.97$ for the porosity of the gels[11], Equation 7.1 predicts $L_w^{dec} \simeq 18\ L_F$; Figure 7.2 shows that this relation is reasonably satisfied for EDAS samples.

At intermediate scale, the combination of microscopy and chord length analysis of

---

[9] See Table 6.2 on page 111.

[10] See Table 5.2 on page 87.

[11] The same value was used in Equation 6.7 on page 111.

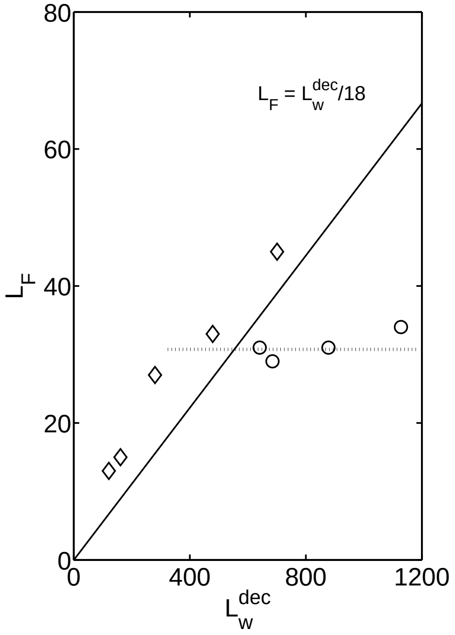

Figure 7.2: Relation between width of the struts $L_F$ and size of the largest pores $L_w^{dec}$ in (◇) EDAS samples and (○) AES samples. The solid line is Equation 7.1 with $\epsilon = 0.97$.

nitrogen adsorption[12] shows that the struts of the gels with large amounts of EDAS are non-porous (Figure 7.1b2), whereas those of samples with a low amount of EDAS have a substructure (Figure 7.1b1). The substructure of the struts in gels with low amounts of EDAS has been analyzed by SAXS; it has a well defined characteristic length[13] $l_C^{(e)} \simeq 40$ nm and it is presumably spinodal-like.[14]

At the smallest investigated length scale, the SAXS patterns of EDAS gels exhibit a power law scattering, with exponents[15] close to 2. Such a low value is reminiscent of a polymeric structure in solution (Figures 7.1c1 and 7.1c2).

In many respects, the gels synthesized with large amounts of AES resemble those synthesized with low amounts of EDAS: their mechanical stiffness[16], pore size[17], width of the struts[18], are similar. Therefore, the large scale structure of gels with a large amount of

---

[12] See Section 5.4.1 on page 92.

[13] See Table 4.1 on page 59.

[14] See *e.g.* Figure 3.10 on page 51.

[15] See Table 4.1 on page 59.

[16] See *e.g.* Figure 6.5 on page 110.

[17] See Table 6.2 on page 111.

[18] See Table 5.2 on page 87.

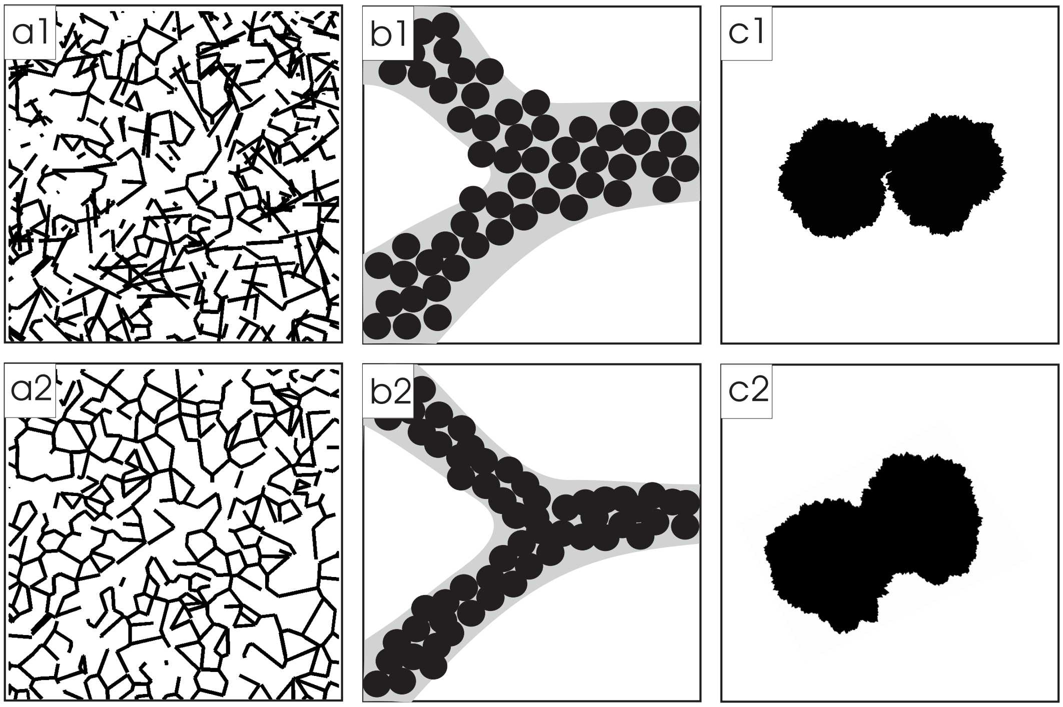

Figure 7.3: Sketch of (a) large scale, (b) intermediate scale and (c) small scale structure of the gels synthesized with small amounts (top) and large amounts (bottom) of AES.

AES is represented in Figure 7.3a2 as in Figure 7.1a1. For lower amounts of AES, the pores are larger as assessed by a larger permeability[19]; the connectivity of the struts is lower, as assessed by the lower mechanical stiffness of the gels[20]. As all gels have the same density, the Poisson-Voronoi modelling imply that the width of the struts increases with pore size, in agreement with Equation 7.1. This is not observed for AES gels (Figure 7.2). Therefore, the structure of gels with low amounts of AES was modelled in Figure 7.3a1 by removing randomly struts from Figure 7.3a2, and dropping them randomly in the figure.

At intermediate scale, the struts of AES gels also have a substructure. In the case of sample AT025 the substructure could be particulate[21]. Therefore, particles are drawn in Figure 7.3b1. When using more AES, the struts are less porous[22]. This is sketched in Figure 7.3b2 by letting the particles inter-penetrate. The qualitatively different substructure of the struts in AES gels (particulate) and in EDAS gels (spinodal) could be related with the observation that the struts of AES gels are less modified by desiccation than the struts of EDAS gels[23].

---

[19] See Table 6.2 on page 111.

[20] See Section 6.4.1 on page 121.

[21] See Figure 5.3 on page 85.

[22] See Section 5.4.1 on page 92.

At the smallest investigated length scale, AES gels seem to be dense, with a rough interface between silica and pore space (Figure 7.3c1 and c2). This results from the asymptotic SAXS exponent close to 3.5, which is typical of surface fractals[24].

## 7.3 Mechanism of gel formation

The microstructure of the gels seems to form *via* a reaction-induced double phase separation mechanism. This conclusion results from the *in situ* SAXS of Chapter 4 and from the structural analysis of Chapter 5. The succession of events leading to the gel formation could be the following. As the hydrolysis and condensation of the precursors proceed, the solubility of molecules in the solvent decreases, which triggers the demixing of the species. In agreement with the theory of viscoeslatic phase separation [Tanaka 2000], a primary phase separation occurs through the nucleation, growth and (possibly) coalescence of vacuole-like solvent-rich domains. During this process, the silica molecules become concentrated is a phase with the morphology of a continuous network of struts. As a consequence of the ongoing polymerization reactions, a secondary phase separation occurs at a smaller scale (Chapter 4), within the struts. The polymerization eventually freezes the evolution of the morphology.

In similar phase-separating silica systems, the final structure of the gels results from the competition between the gelation reactions and phase separation [Nakanishi 1997]. In the present context, if gelation occurs early during the primary phase separation, a structure with small pores supported by short and thin struts is obtained. On the contrary, if gelation occurs later, the phase separation can proceed to a state with larger pores supported by longer and thicker struts. This seems to be the case for EDAS and AES gels. Indeed, taking the time for turbidity $t_{turbidity}$ as the time of occurrence of the primary phase separation, one sees that $t_{turbidity}$ is much shorter than $t_{gel}$ for the gels with the largest pores [25]. On the contrary, $t_{turbidity}$ is close to $t_{gel}$ for the gels with the smallest pores[26].

---

[23] See Section 6.4.1 on page 121.

[24] See Table 4.1 on page 59.

[25] ET025 and AT05 in Table 5.1 on page 82.

The same analysis can be used for the small scale phase separation, evidenced by SAXS in Chapter 4 for EDAS and AES gels, and in Chapter 3 for EDAS-Pd gels. For gels with low amounts of AES[27], gelation occurs much later than the secondary phase separation; for gels with large amounts of AES gelation occurs earlier. This can be the reason why the substructure of the struts is more developed for samples with low amounts of AES[28]. The existence of particle-like objects in AES gels[29] could result from a Rayleigh instability of the spinodal structures, by which a liquid column spontaneously decomposes into droplets [Molares *et al.* 2004; Yang *et al.* 1998]. Such a decomposition of the spinodal structure into particles could also be responsible for the lowering of the connectivity of the struts in samples with little AES[30].

The case of EDAS gels is more complex. For the gel with the largest amount of EDAS, it is not clear whether a double phase separation actually takes place. For that sample, the struts are indeed dense[31]. It therefore seems that the phase separation detected by SAXS could be responsible for the formation of the largest pores in the sample with the largest amount of EDAS. The difference between the characteristic sizes estimated by SAXS[32] and by beam-bending[33] for gel ET20 could result from structural polydispersity rather than from the occurrence of two distinct phase separation processes. Nevertheless, the gross trend throughout EDAS series, is that gelation occurs earlier during the secondary phase separation when more EDAS is used. This observation could account for the more developed substructure of the struts when less EDAS is used[34].

Figure 7.2 is reminiscent of Figure 1.6 on page 12. Both figures analyse the impact of the co-reactant on the characteristic size of the xerogels using a mass-balance equation. Both figures evidence a qualitatively different behaviour of EDAS and AES gels. In the context of the nucleation model, Figure 1.6 suggests that the physicochemical mechanisms governing the formation of EDAS and of AES gels are different. Figure 7.2, on the other hand, suggests that the same phase separation phenomenon occurs with both co-reactants; the mechanism by which the vacuole-like pores grow is different.

---

[26] For instance, sample ET10 in Table 5.1 on page 82.

[27] AT05 in Figure 4.8 on page 67.

[28] See Section 5.4.1 on page 92.

[29] See Figure 5.3 on page 85.

[30] See Section 6.4.1 on page 121.

[31] See Section 5.4.1 on page 5.4.1.

[32] See Table 4.1 on page 59.

[33] See Table 6.2 on page 111.

[34] See Section 5.4.1 on page 92.

## 7.4 Samples with metal

Time-resolved SAXS shows that the formation of the gels with EDAS-Pd is governed by the same phase separation mechanism as the gels synthesized with EDAS alone (Chapters 3 and 4). As the large scale structure of EDAS-Pd xerogel catalysts is qualitatively similar to that of EDAS xerogels [Heinrichs *et al.* 1997b], the same double phase separation process presumably governs the formation of both systems.

One important characteristic of EDAS-Pd xerogel catalysts is that the metal particles are buried inside the silica for low metal loadings (Chapter 2). This could find an explanation in the frame of a reaction-induced phase separation process. For a system with a broad distribution of molecular weights, the reaction-induced phase separation is a progressive process during which the species with a large molecular weight precipitate preferentially [Billmeyer 1984]. As reported in Chapter 1, EDAS is more reactive than TEOS. During the polymerization of the precursors, the EDAS-Pd monomers are therefore likely to be present is the molecules with the largest molecular weight. The regularity of the the metal particles dispersion revealed by electron tomography[35] corresponds to a kind of periodicity; it could therefore be related to the very occurrence of phase separation with a well defined characteristic length.

As loading increases, larger and larger amounts of metal are found outside the silica[36]. A similar observation was made for metal-free samples. Larger amounts of EDAS or of AES are found on the silica surface when more co-reactant is used[37].

---

[35] See Section 2.4 on page 34.

[36] See Section 2.4 on page 34.

[37] See Section 5.4.2 on page 94.

## 7.5 Conclusion

Some insight obtained in the present thesis about the silica gels synthesized with organically modified co-reactants is based on the use of experimental techniques never applied before on these materials. In particular: electron tomography reveals the regularity in the dispersion of the metal nanoparticles, *in situ* SAXS shows that a reaction-induced phase separation occurs, and beam-bending demonstrates that the impact of desiccation on the nanostructure of the analysed gels depends on the amount and nature of co-reactant. The use of these techniques enables the more classical characterisation data to be analysed in a new light.

The conclusions reached in this thesis are mainly phenomenological. They hint at the important role of physical phenomena during the successive steps of the material's formation, from the initial reacting solution to the xerogel, *via* phase separation and drying.

# Appendix A

# Opening Granulometry

Opening granulometry is a general tool developed in the frame of mathematical morphology to analyze both binary and grey level images. In this appendix, we shall only recall in an intuitive way its principle, and the interested reader should consult Serra [1982] for a thorough mathematical presentation.

An image is an intensity function of one, two or three spatial variables $I(x, y, z)$. Any morphological filter uses a geometrical object called a structuring element (SE) with which the image is compared. Typically, for a 1D image the SEs can be segments of various lengths, for a 2D image they can be disks of various diameters, squares, *etc.* To understand how an opening filter modifies an image, it is convenient to visualize it as a topographic surface, where the gray level is converted to an altitude.

The case of a 1D image, $I(x)$, scanned with a segment as SE is illustrated in Figure A.1a. For each position of the segment, it is pushed upward from beneath until it touches the $I(x)$ curve. The opening of $I(x)$ by the segment is defined as the upper envelope of all the positions reached by the segment. If the size of SE is smaller than the features of $I(x)$, it can be pushed everywhere very close to the curve and the opening has almost no effect on $I(x)$. On the contrary, if the size of SE is larger than, say, the width of the humps in $I(x)$, these will be removed by the opening, but the larger features of $I(x)$ will still be preserved. In Figure A.1a, the opening of a given function by segments of increasing lengths is considered. SE$_1$ is small enough to enter the humps of $I(x)$, SE$_2$ is larger than the humps but it can still enter the larger features resulting from the superposition of two humps (at $x \simeq 5$), SE$_3$ can only enter the objects resulting from the superposition of three

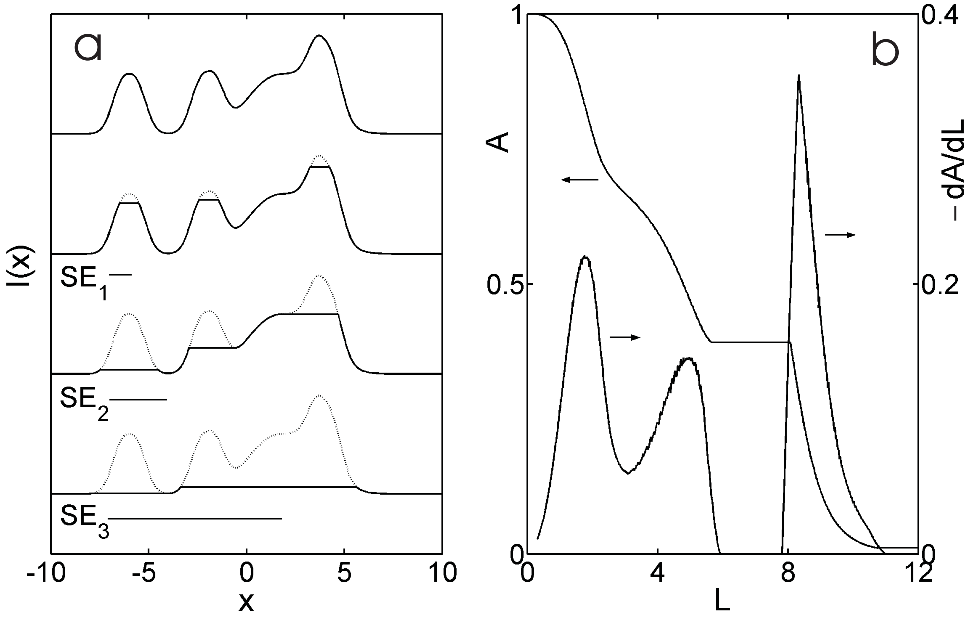

Figure A.1: Principle of opening granulometry: (a) applying an opening filter to a given function $I(x)$ is equivalent to trying to push a Structuring Element (SE) into the details of it from beneath; (b) the characteristic sizes are obtained by considering the remaining area $A(L)$ under the curves of $I(x)$ after opening it with a SE of size $L$. The characteristic sizes are the maxima of the derivative $-dA/dL$.

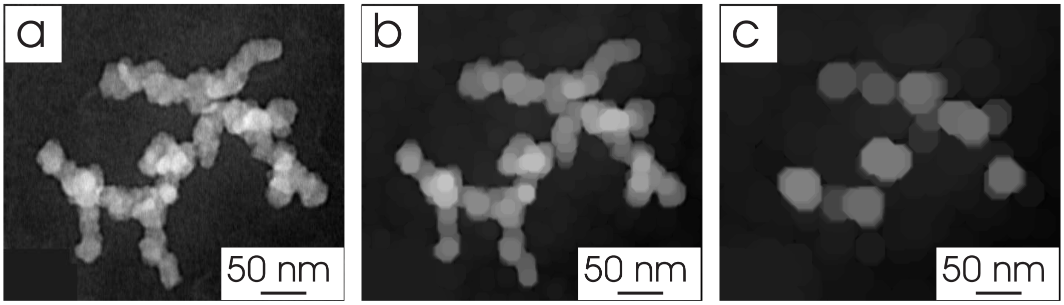

Figure A.2: (a) Example of a type B micrograph of xerogel AT10 (see Chapter 5), inverted so as to make the silica appear bright, and the same image after opening with a disk of diameter (b) $L = 16$ nm, and (c) $L = 32$ nm.

humps.

The total area under the curve of $I(x)$ after opening with a segment of length $L$, $A(L)$, is a decreasing function of $L$. If only features of size $L_0$ were present in $I(x)$, then $A(L)$ would decrease markedly only near $L = L_0$, and the derivative $-dA/dL$ would exhibit a peak at that position. The granulometry curves of Figure A.1a, $A(L)$ and $-dA/dL$ are plotted in Figure A.1b. The $-dA/dL$ curve exhibits three peaks at $L = 2$, at $L = 5$ and at $L = 8$. These values correspond to the three characteristic lengths of $I(x)$, resulting (i) from the individual humps, (ii) from the superposition of two humps, and (iii) from the superposition of three humps.

The same procedure can be applied to analyze a 2D gray level image, using a 2D structuring element. This is illustrated in Figure A.2, where a given image is opened with disks of increasing diameters. The original image (Figure A.2a) is a type B micrograph (see Section 5.2.3 on page 83), that has been inverted so as to make the silica appear bright. The *volume* of this image, $V$, is defined as the volume under its topographic equivalent surface, equivalent to the mean gray level of all the pixels in the image. Opening the image with a disk of diameter 16 nm only results in a smoothing of the silica skeleton (Figure A.2b), and $V$ does not decrease significantly. On the contrary, a significant fraction of the silica skeleton is removed by an opening with a disk of diameter 32 nm (Figure A.2c). Figure A.3 plots the volume $V(L)$ of the image of Figure A.2a after opening with disks of increasing diameters $L$. The derivative $-dV/dL$ exhibits a maximum at $L \simeq 30$ nm, corresponding to characteristic size of the silica skeleton.

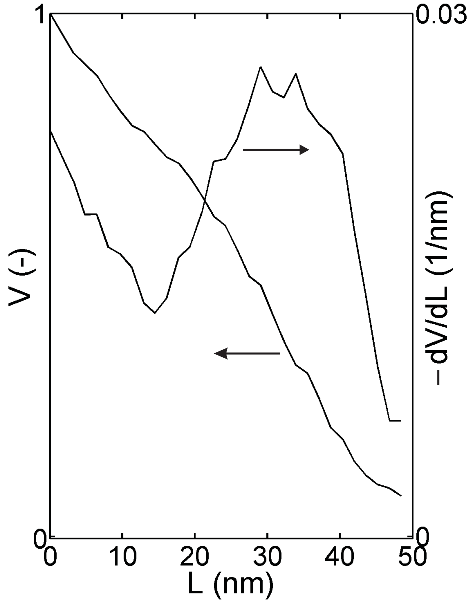

Figure A.3: Cumulative opening granulometry curve $V(L)$, obtained from the image in Figure A.2a, and its derivative $-dV/dL$.

# Appendix B

# Fitting procedure of the beam bending relaxation data

The equation used to analyze the beam bending experiments on wet gels in Chapter 6 is the following that accounts for both hydrodynamic and viscoelastic relaxations [Scherer 1992; 1994b]

$$W(t) = W(0) \underbrace{\left[ \frac{2(1+\nu)}{3} + \frac{(1-2\nu)}{3} S\left(\frac{t}{\tau_h}\right) \right]}_{hydrodynamic} \underbrace{\exp\left[ -\left(\frac{t}{\tau_{VE}}\right)^{b} \right]}_{viscoelastic} \tag{B.1}$$

where $W(0)$ is the initial load that follows immediately the deflection, $\nu$ is the Poisson ratio of the gel's skeleton, $\tau_h$ is the hydrodynamic relaxation time, $\tau_{VE}$ is an average viscoelastic relaxation time, and $b$ is related to the breadth of the distribution of viscoelastic relaxation times.

The hydrodynamic relaxation function $S(t/\tau_h)$ in Equation B.1 is defined by a series, as in Equation 6.4 on page 108. For the sake of simplifying the fitting procedure, the series is approximated by the following function

$$S\left(\frac{t}{\tau_h}\right) \simeq \exp\left[ -4.54 \left(\frac{t}{\tau_h}\right)^{1/2} - 3.50 \left(\frac{t}{\tau_h}\right) - 8.93 \left(\frac{t}{\tau_h}\right)^{3/2} \right] \tag{B.2}$$

As illustrated in Figure B.1, this expression is a very accurate approximation of $S(t/\tau_h)$.

The fitting of the experimental data is performed in the Matlab® environment. As Equation B.1 is not linear in the parameters to be optimized, $\tau_{VE}$, $b$, $W(0)$, $\nu$ and $\tau_h$, the fitting procedure requires some initial values that have to be determined with some

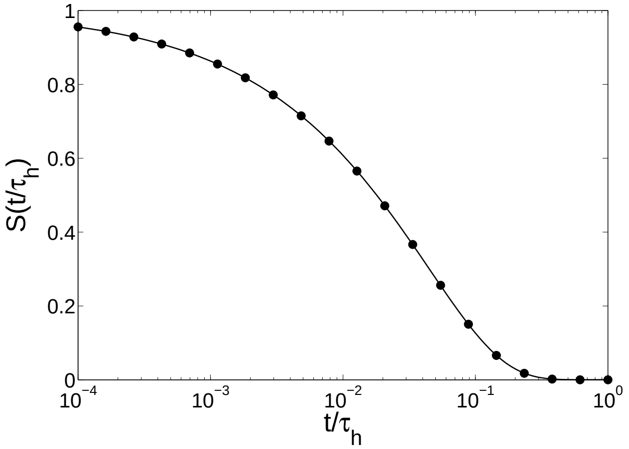

Figure B.1: Hydrodynamic relaxation function $S(t/\tau_h)$. The dots are the values estimated from Equation 6.4 with 500 terms, and the solid line is the approximate value from Equation B.2.

caution. This is done as follows. First, the time limit, $t_{lim}$, between the hydrodynamic and the viscoelastic relaxation regimes is determined manually as the approximate position of the bend in the relaxation curve (see Figure B.2a). A purely viscoelastic model of the form

$$W'(t) = W'(0) \exp\left[-\left(\frac{t}{\tau_{VE}}\right)^b\right] \tag{B.3}$$

is adjusted on the data for $t > t_{lim}$. This expression is an approximation of Equation B.1 for $t \gg \tau_h$, for which $S(t/\tau_h) \simeq 0$. Comparing Equations B.1 and B.3, one finds

$$W'(0) = W(0)\frac{2(1+\nu)}{3} \tag{B.4}$$

To fit Equation B.3, a few tens of values of $W'(0)$ ranging from $W(t_{lim})$ to $2W(t_{lim})$ are systematically tested, and for each value Equation B.3 is adjusted to the data under the form

$$\ln\left(\frac{W'(t)}{W'(0)}\right) = b\ln(t) - \ln(\tau_{VE}) \tag{B.5}$$

The fact that the latter expression is linear in $b$ and $\tau_{VE}$ ensures that, for any value of $W'(0)$, the optimal values of $b$ and of $\tau_{VE}$ are unique. The chosen values of $W'(0)$, $\tau_{VE}$ and $b$ are those that minimize the fitting error. Figure B.2b compares the relaxation data with expression B.3, with the values of the parameters being optimized.

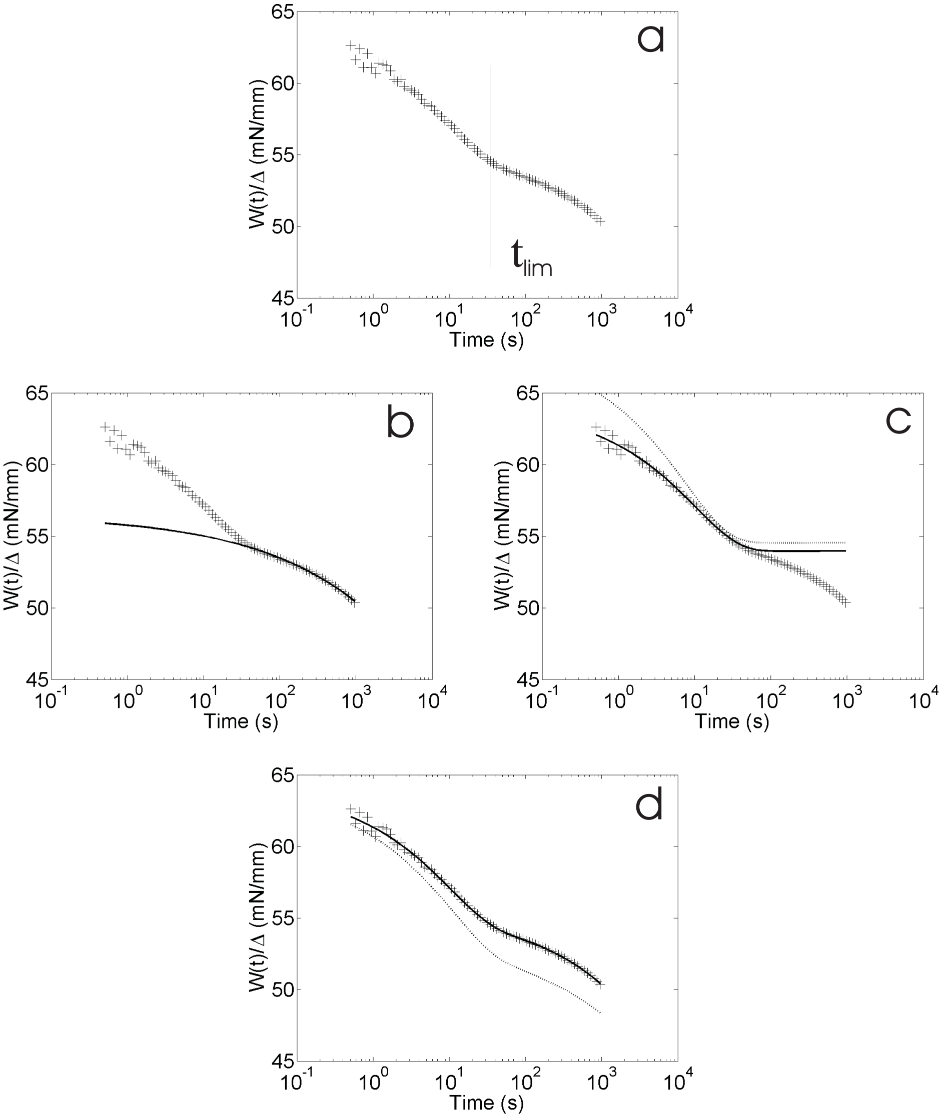

Figure B.2: Fitting of an experimental relaxation curve with Equation B.1. (a) The time limit $t_{lim}$ between hydrodynamic and viscoelastic relaxation is determined manually as the position on the bend in the curve. (b) The relaxation for $t > t_{lim}$ is fitted with the purely viscoelastic model (Equation B.3). (c) The relaxation for $t < t_{lim}$ is fitted with the purely hydrodynamic relaxation model (Equation B.6). (d) The complete model is then fitted over the entire time range. The dotted lines are the theoretical expressions with the initial value of the parameters and the solid lines correspond to the optimal value of the parameters.

Once this is done, the data for $t < t_{lim}$ are adjusted with a purely hydrodynamic relaxation model:

$$W(t) = W(0)\left[\frac{2(1+\nu)}{3} + \frac{(1-2\nu)}{3}S\left(\frac{t}{\tau_h}\right)\right] \tag{B.6}$$

The initial value of $\nu$ is chosen to be $\nu = 0.2$, which is typical of highly porous materials [Roberts & Garboczi 2000] and of gels in particular [Scherer 1996]. The initial value of $W(0)$ is obtained from the value of $W'(0)$, optimized previously, as

$$W(0) = \frac{3W'(0)}{2(1+\nu)} \tag{B.7}$$

which simply results from B.4. The initial value of $\tau_h$ is chosen to be $5 \times t_{lim}$, which comes from the observation that the hydrodynamic relaxation is almost finished at $t/\tau_h = 1/5$ (see Figure B.1). Figure B.2c compares the data with Equation B.6, with the initial values of the parameters as well as with the optimized values.

Finally, the relaxation data are fitted over the entire time range, with the complete model of Equation B.1, using the parameters already obtained as initial values to be optimized. Figure B.2d compares the data with Equation B.1, with the initial values of the parameters as well as with the optimized values.

Table B.1 reports the values of the parameters obtained from the data in Figure B.2. The error reported in this table quantifies the uncertainty in the fit resulting from the initial choice of $t_{lim}$. Apart from the viscoelastic relaxation parameters $\tau_{VE}$ and $b$, for which the uncertainty is quite large, the value of all other parameters are not very sensitive to the initial value of $t_{lim}$. For instance, the uncertainty on $W(0)$, $\tau_h$ and $\nu$, from which the permeability can be estimated, does not exceed a few percent.

Table B.1: Parameters obtained by fitting the experimental relaxation curve in Figure B.2 with the viscoelastic, the hydrodynamic, and the complete model (Equations B.3, B.6, and B.1, respectively), over the appropriate time range. The same curve was fitted 5 times independently; the error is the standard deviation that results from a slightly different choice of $t_{lim}$ each time.

| Model | $W'(0)$ (mN/mm) | $\tau_{VE}$ ($10^3$s) | $b$ (-) | $W(0)$ (mN/mm) | $\tau_h$ (s) | $\nu$ (-) |
|---|---|---|---|---|---|---|
| Eq B.3 | 55.9 ± 0.4 | 520 ± 305 | 0.37 ± 0.04 | -[a] | -[a] | -[a] |
| Eq B.6 | -[a] | -[a] | -[a] | 64.0 ± 0.1 | 243 ± 10 | 0.262 ± 0.004 |
| Eq B.1 | -[a] | 207 ± 47 | 0.45 ± 0.03 | 64.1 ± 0.1 | 216 ± 6 | 0.292 ± 0.003 |

[a] not applicable.

# Bibliography

Adler, P.M. 1992. *Porous Media, Geometry and Transports.* Boston: Butterworth-Heinemann.

Al-Muhtaseb, S.A., & Ritter, J.A. 2003. Preparation and properties of resorcinol-formaldehyde organic and carbon gels. *Advanced Materials*, **15**, 101–114.

Alié, C. 2002. *Synthesis of silica with tailored morphology by sol-gel process.* Ph.D. thesis, University of Liège.

Alié, C., Pirard, R., Lecloux, A.J., & Pirard, J.-P. 1999. Preparation of low-density xerogels through additives to TEOS-based alcogels. *Journal of Non-Crystalline Solids*, **246**, 216–228.

Alié, C., Ferauche, F., Pirard, R., Lecloux, A. J., & Pirard, J.-P. 2001. Preparation of low-density xerogels by incorporation of additives during synthesis. *Journal of Non-Crystalline Solids*, **289**, 88–96.

Aubert, J.H. 1988. Isotactic polystyrene phase diagrams and physical gelation. *Macromolecules*, **21**, 3468–3473.

Avnir, D., Klein, L.C., Levy, D., Schubert, U., & Wojcik, A.B. 1998. Organo-silica sol-gel materials. *Pages 2317–2362 of:* Rappoport, Z., & Apeloig, Y. (eds), *The Chemistry of Organic Silicon Compounds*, vol. 2. Chichester: Wiley.

Bates, F.S., & Wiltzius, P.J. 1989. Spinodal decomposition of a symmetric critical mixture of deuterated and protonated polymer. *Journal of Chemical Physics*, **91**, 3258–3274.

Beelen, T.P.M., Dokter, W.H., Garderen, H.F., & VanSanten, R.A. 1994. Aggregation, gelation and aging in silica. *Advances in Colloid and Interface Science*, **50**, 23–27.

Benoît, H., Joanny, J.F., Hadziioannou, G., & Hammouda, B. 1993. Scattering by linear, branched, and copolymer chain molecules for large scattering vectors. *Macromolecules*, **26**, 5790–5795.

Berk, N.F. 1987. Scattering properties of a model bicontinuous structure with a well defined length scale. *Physical Review Letters*, **58**, 2718–2721.

Bibette, J., Mason, T.G., Gang, H., & Weitz, D.A. 1992. Kinetically induced ordering in gelation of emulsions. *Physical Review Letters*, **69**, 981–984.

Billmeyer, F.W. 1984. *Textbook of Polymer Science*. 3rd edn. New York: Wiley.

Blanco, E., del Solar, M. Ramirez, de la Rosa-Fox, N., & Craievich, A.F. 1992. SAXS study of growth kinetics of fractal aggregates in TEOS-water-alcohol solutions with formamide. *Journal of Non-Crystalline Solids*, **147 and 148**, 238–244.

Boukari, H., Lin, J.S., & Harris, M.T. 1997. Probing the dynamics of the silica nanostructure formation and growth by SAXS. *Chemistry of Materials*, **9**, 2376–2384.

Brand, M., Frings, A., Jenkner, P., Lehnert, R., Metternich, H.J., Monkiewicz, J., & Schram, J.Z. 1999. *Naturforshung*, **54b**, 155–64.

Breitscheidel, B., Zieder, J., & Schubert, U. 1991. Metal complexes in inorganic matrices. 7. Nanometer-sized, uniform metal particles in a silica matrix by sol-gel processing of metal complexes. *Chemistry of Materials*, **3**, 559–566.

Brinker, C.J., & Scherer, G.W. 1985. Sol, gel, glass: I. Gelation and gel structure. *Journal of Non-Crystalline Solids*, **70**, 301–322.

Brinker, C.J., & Scherer, G.W. 1990. *Sol-Gel Science: the Physics and Chemistry of Sol-Gel Processing*. San Diego: Academic Press.

Brochard, F., & de Gennes, P.-G. 1977. Dynamical scaling for polymers in theta solvents. *Macromolecules*, **10**, 1157–1161.

Burchard, W. 1977. Particle scattering factors of some branched polymers. *Macromolecules*, **10**, 919–927.

Carpineti, M., Giglio, M., & Degiorgio, V. 1995. Mass conservation and anticorrelation effects in the colloidal aggregation of dense solutions. *Physical Review E*, **51**, 590–596.

Chaumont, D., Craievich, A., & Zarzycki, J. 1992. A SAXS study of the formation of zirconia sols and gels. *Journal of Non-Crystalline Solids*, **147 and 148**, 127–134.

Clarke, N., McLeish, T.C.B., & Jenkins, S.D. 1995. Phase behavior of linear/branched polymer blends. *Macromolecules*, **28**, 4650–4659.

Collison, D., Garner, C.D., McGrath, C.M., Mosselmans, J.F., Pidcock, E., Roper, M.D., Searle, B.G., Seddon, J.M.W., & Sinn, E. 1998. A study of the soft X-ray photoreduction of [NiIV(S2CNEt2)3][BF4] and soft X-ray photoisomerisation of [PPh4][NiII(S2COEt)3] at the Ni L-edge. *Journal of the Chemical Society, Dalton Transactions: Inorganic Chemistry*, **24**, 4179–4186.

Daoud, M., & Martin, J.E. 1989. Fractal properties of polymers. *In:* Avnir, D. (ed), *The Fractal Approach to Heterogeneous Chemistry.* New York: Wiley.

Dean, J.A. 1992. *Lange's Handbook of Chemistry.* New York: Mc Graw-Hill.

deGennes, P.-G. 1979a. Effect of cross-links on a mixture of polymers. *Journal de Physique Letters*, **40**, 69–72.

deGennes, P.-G. 1979b. *Scaling Concepts in Polymer Physics.* Ithaca and London: Cornell University Press.

Devreux, F., Boilot, J.F., Chaput, F., & Lecomte, A. 1990. Sol-gel condensation of rapidly hydrolyzed silicon alkoxides: A joint $^{29}$Si NMR and small-angle X-ray scattering study. *Physical Review A*, **41**, 6901–6909.

Dietler, G., Aubert, C., Cannel, D.S., & Wiltzius, P. 1986. Gelation of colloidal silica. *Physical Review Letters*, **57**, 3117–3120.

Elwell, M.J., Ryan, A.J., Grnbauer, H.J.M., & VanLieshout, H.C. 1996. In-Situ studies of structure development during the reactive processing of model flexible polyurethane foam systems using FT-IR spectroscopy, synchrotron SAXS, and rheology. *Macromolecules*, **29**, 2960–2968.

Fermigier, M. 1999. *Hydrodynamique Physique*. Paris: Dunod.

Fidalgo, A., Rosa, M.E., & Ilharco, L.M. 2003. Chemical control of highly porous silica xerogels: physical properties and morphology. *Chemistry of Materials*, **15**, 2186–2192.

Flory, P. 1971. *Principles of Polymer Chemistry*. Ithaca: Cornell University Press.

Frank, J. (ed). 1992. *Electron Tomography: Three-Dimensional Imaging with Transmission Electron Microscope*. Kluwer Academic.

Fujita, K., Konishi, J., Nakanishi, K., & Hirao, K. 2004. Strong light scattering in macroporous $TiO_2$ monoliths induced by phase separation. *Applied Physics Letters*, **85**, 5595–5597.

Gibson, L.J., & Ashby, M.F. 1988. *Cellular Solids, Structure and Properties*. Oxford: Pergamon Press.

Glatter, O., & Kratky, O. 1982. *Small Angle X-ray Scattering*. New York: Academic Press.

Gommes, C.J., Blacher, S., & Pirard, J.-P. 2005. Nitrogen adsorption on silica xerogels or the odd look of a t-plot. *Langmuir*, **21**, 1703–1705.

Gonzalez, R.D., Lopez, T., & Gomez, R. 1997. Sol-gel preparation of supported metal catalysts. *Catalysis Today*, **35**, 293–317.

Gross, J., & Fricke, J. 1992. Ultrasonic velocity measurements in silica, carbon and organic aerogels. *Journal of Non-Crystalline Solids*, **145**, 217–222.

Guenoun, P., Gastaud, R., Perrot, F., & Beysens, D. 1987. Spinodal decomposition patterns in an isodensity critical binary fluid: direct-visualization and light-scattering analyses. *Physical Review A*, **36**, 4876–4890.

Hasmy, A., & Jullien, R. 1995. Sol-gel process simulation by cluster-cluster aggregation. *Journal of Non-Crystalline Solids*, **186**, 342–348.

Haumann, M., Grabolle, M., Neisius, T., & Dau, H. 2002. The first room-temperature X-ray absorption spectra of higher oxidation states of the tetra-manganese complex of photosystem II. *FEBS Letters*, **512**, 116–120.

Heinrichs, B., Delhez, P., Schoebrechts, J.-P., & Pirard, J.-P. 1997a. Palladium-silver sol-gel catalysts for selective hydrodechlorination of 1,2-dichloroethane into ethylene. I. Synthesis and characterization. *Journal of Catalysis*, **172**, 322–335.

Heinrichs, B., Noville, F., & Pirard, J.-P. 1997b. Pd/$SiO_2$-cogelled aerogel catalysts and impregnated aerogel and xerogel catalysts: synthesis and characterization. *Journal of Catalysis*, **170**, 366–376.

Heinrichs, B., Pirard, J.-P., & Schoebrechts, J.-P. 2001. Mass transfer in low density xerogel catalysts. *AIChE Journal*, **47**, 1866–1873.

Heinrichs, B., Lambert, S., Alié, C., Pirard, J.-P., Beketov, G., Nehasil, V., & Kruse, N. 2002. Cogelation: an effective sol-gel method to produce sinter-proof finely dispersed metal catalysts supported on highly porous oxides. *Studies in Surface Science and Catalysis*, **143**, 25–33.

Heinrichs, B., Noville, F., Schoebrechts, J.-P., & Pirard, J.-P. 2003. Palladium-silver sol-gel catalysts for selective hydrodechlorination of 1,2-dichloroethane into ethylene. IV Deactivation mechanism and regeneration. *Journal of Catalysis*, **220**, 215–225.

Himmel, B., Burger, H., Gerber, Th., & Olbertz, A. 1995. Structural characterization of $SiO_2$ aerogels. *Journal of Non-Crystalline Solids*, **185**, 56–66.

Hrubesh, L.W. 1998. Aerogel applications. *Journal of Non-Crystalline Solids*, **225**, 335–342.

Hüsing, N., Schubert, U., Misof, K., & Fratzl, P. 1998. Formation and structure of porous gel networks from $Si(OMe)_4$ in the presence of $A(CH_2)_nSi(OR)_3$(A = functional group). *Chemistry of Materials*, **10**, 3024–3032.

Hüsing, N., Schubert, U., Mezei, R., Fratzl, P., Riegel, B., Kiefer, W., Kohler, D., & Mader, W. 1999. Formation and structure of gel networks from $Si(OEt)_4/(MeO)_3Si(CH_2)_3NR'_2$ mixtures ($NR'_2 = NH_2$ or $NHCH_2CH_2NH_2$). *Chemistry of Materials*, **11**, 421–457.

Iler, R.K. 1979. *The Chemistry of Silica: Solubility, Polymerization, Colloid and Surface Properties, and Biochemistry.* New York: Wiley.

Ishii, Y., & Ryan, A.J. 2000. Processing of poly(2,6-dimethyl-1,4-phenylene ether) with epoxy resin. 1. reaction-induced phase separation. *Macromolecules*, **33**, 158–166.

Jackson, C.L., & Shaw, M.T. 1990. The phase behaviour and gelation of a rod-like polymer in solution and implications for microcellular foam morphology. *Polymer*, **31**, 1070–1084.

Janssen, A.H., Yang, C.-M., Wang, Y., Schuth, F., Koster, A.J., & deJong, K.P. 2003. Localization of small metal (oxide) particles in SBA-15 using bright-field electron tomography. *Journal of Physical Chemistry B*, **107**, 10552–10556.

Jullien, R., & Hasmy, A. 2005. Fluctuating bond aggregation: a model for chemical gel formation. *Physical Review Letters*, **20**, 4003–4006.

Kaji, H., Nakanishi, K., Soga, N., Inoue, T., & Nemoto, N. 1994. In situ observation of phase separation processes in gelling alkoxy-derived silica system by light scattering method. *Journal of Sol-Gel Science and Technology*, **3**, 169–188.

Kaji, H., Nakanishi, K., & Soga, N. 1995. Formation of porous gel morphology by phase separation in gelling alkoxy-derived silica. Phenomenological study. *Journal of Non-Crystalline Solids*, **185**, 18–30.

Kallala, M., Sanchez, C., & Cabane, B. 1993. Structures of inorganic polymers in sol-gel processes based on titanium oxide. *Physical Review E*, **48**, 3692–3704.

Kaneko, K. 1994. Determination of pore size and pore size distribution : 1. Adsorbents and catalysts. *Journal of Membrane Science*, **96**, 58–89.

Katz, A.J., & Thompson, A.H. 1986. Quantitative prediction of permeability in porous rocks. *Physical Review B*, **34**, 8179–8181.

Kinney, J.H., & Ladd, A.J.C. 1998. The relationship between three-dimensional connectivity and the elastic properties of trabecular bone. *Journal of Bone and Mineral Research*, **13**, 839–845.

Klein, L.C. (ed). 1988. *Sol-gel technology for thin films, fibers, preforms, electronics and specialty shapes.* Park Ridge, USA: Noyes Publications.

Kolb, M., Botet, R., & Jullien, R. 1983. Scaling of kinetically growing clusters. *Physical Review Letters*, **51**, 1123–11269.

Koster, A.J., Ziese, U., Verkeleij, A.J., Janssen, A.H., & deJong, K.P. 2000. Three-dimensional transmission electron microscopy: a novel imaging and characterization technique with nanometer scale resolution for materials science. *Journal of Physical Chemistry B*, **104**, 9368–9370.

Kotlarchyk, M., & Chen, S.-H. 1983. Analysis of small angle neutron scattering spectra from polydisperse interacting colloids. *Journal of Chemical Physics*, **79**, 2461–2469.

Lambert, S., Polard, J.-F., Pirard, J.-P., & Heinrichs, B. 2004a. Improvement of metal dispersion in Pd/$SiO_2$ cogelled xerogel catalysts for 1,2-dichloroethane hydrodechlorination. *Applied Catalysis B*, **50**, 127–140.

Lambert, S., Alié, C., Pirard, J.-P., & Heinrichs, B. 2004b. Study of textural properties and nucleation phenomenon in Pd/$SiO_2$, Ag/$SiO_2$ and Cu/$SiO_2$ cogelled xerogel catalysts. *Journal of Non-Crystalline Solids*, **342**, 70–81.

Lambert, S., Sacco, L., Heinrichs, B., Noels, A., & Pirard, J.-P. 2004c. Synthesis of $SiO_2$ xerogels and Pd/$SiO_2$ cogelled xerogel catalysts from silylated acetylacetonate ligand. *Journal of Non-Crystalline Solids*, **343**, 109–120.

Lambert, S., Cellier, C., Grange, P., Pirard, J.-P., & Heinrichs, B. 2004d. Synthesis of Pd/$SiO_2$, Ag/$SiO_2$, and Cu/$SiO_2$ cogelled xerogel catalysts: study of metal dispersion and catalytic activity. *Journal of Catalysis*, **221**, 335–346.

Lambert, S., Ferauche, F., Brasseur, A., Pirard, J.-P., & Heinrichs, B. 2005. Pd-Ag/$SiO_2$ and Pd-Cu/$SiO_2$ cogelled xerogel catalysts for selective hydrodechlorination of 1,2-dichloroethane into ethylene. *Catalysis Today*, **100**, 283–289.

Landau, L., & Lifshitz, E. 1959. *Theory of Elasticity*. London: Pergamon.

Lebon, S., Marignan, J., & Appel, J. 1992. Titania gels: aggregation and gelation kinetics. *Journal of Non-Crystalline Solids*, **147-148**, 92–96.

Lecloux, A.J. 1981. Texture of Catalysts. *Pages 171–230 of:* Anderson, J.R., & Boudart, M. (eds), *Catalysis: Science and Technology*, vol. 2. Berlin: Springer.

Lecloux, A.J., & Pirard, J.-P. 1998. High-temperature catalysts through sol-gel synthesis. *Journal of Non-Crystalline Solids*, **225**, 146–152.

Lecomte, A., Dauger, A., & Lenormand, P. 2000. Dynamical scaling property of colloidal aggregation in a zirconia-based precursor sol during gelation. *Journal of Applied Crystallography*, **33**, 496–99.

Lee, K., Look, J.L., Harris, M.T., & McCormick, A.V. 1997. Assessing extreme models of the Stöber synthesis using transients under a range of initial composition. *Journal of Colloid and Interface Science*, **194**, 78–88.

Ma, H.-S., Roberts, A.P., Prévost, J.-H., Jullien, R., & Scherer, G.W. 2000. Mechanical structure-property relationship of aerogels. *Journal of Non-Crystalline Solids*, **277**, 127–141.

Ma, H.-S., Jullien, R., & Scherer, G.W. 2002a. Dangling bond deflection model: growth of gel network with loop structure. *Physical Review E*, **65**, 041403.

Ma, H.-S., Prévost, J.-H., & Scherer, G.W. 2002b. Elasticity of DLCA model gels with loops. *International Journal of Solids and Structures*, **39**, 4605–4614.

Martin, J.E., & Odinek, J. 1990. Effect of swelling on the fractal dimension of branched silica polymers formed near the sol-gel transition. *Macromolecules*, **23**, 3362–3367.

Mastronarde, D.N. 1997. Dual-axis tomography: an approach with alignment methods that preserve resolution. *Journal of Structural Biology*, **120**, 343–352.

Meakin, P. 1983. Formation of fractal clusters and networks by irreversible diffusion-limited aggregation. *Physical Review Letters*, **51**, 1119–1122.

Molares, M.E.T., Balogh, A.G., Cornelius, T.W., Neumann, R., & and, C. Trautman. 2004. Fragmentation of nanowires driven by Rayleigh instability. *Applied Physics Letters*, **85**, 5337–5339.

Mörke, W., Lamber, R., Schubert, U., & Breitscheidel, B. 1994. Metal complexes in inorganic matrixes. 11. composition of highly dispersed bimetallic Ni, Pd alloy particles prepared by Sol-Gel processing: electron microscopy and FMR study. *Chemistry of Materials*, **6**, 1659–1666.

Mortensen, K., & Pedersen, J.S. 2001. Structural studies of polymer systems using small-angle neutron scattering. *Page 223 of:* Nalwa, H.S. (ed), *Advanced Functional Molecules and Polymers.* Amsterdam: Overseas Publishers Association.

Nakanishi, K. 1997. Pore structure control of silica gels based on phase separation. *Journal of Porous Materials*, **4**, 67–112.

Ohser, J., & Mücklich, F. 2000. *Statistical Analysis of Microstructures in Materials Science.* Chichester: Wiley.

Olabisi, O., Robeson, L.M., & Shaw, M.T. 1979. *Polymer-Polymer Miscibility.* New York: Academic Press.

Osada, Y., & Gong, J.-P. 1998. Soft and wet materials: polymer gels. *Advanced Materials*, **10**, 827–837.

Otsu, N. 1979. A threshold selection method from gray-level histograms. *IEEE Transactions on Systems Man and Cybernetics*, **9**, 62–66.

Pan, I.C., Tang, M., & Chen, Y.-P. 2000. Densities and viscosities of binary liquid mixtures of vynil acetate, diethyl oxalate, and dibutyl phtalate with normal alkanols at 303.15 K. *Journal of Chemical Engineering Data*, **45**, 1012–1015.

Pekala, R.W., & Schaefer, D.W. 1993. Structure of organic aerogels. 1. Morphology and scaling. *Macromolecules*, **26**, 5487–5491.

Perin, L., Faivre, A., Calas-Etienne, S., & Woignier, T. 2004. Nanostructural damage associated with isostatic compression of silica aerogels. *Journal of Non-Crystalline Solids*, **333**, 68–73.

Pirard, R., Blacher, S., Brouers, F., & Pirard, J.-P. 1995. Interpretation of mercury porosimetry applied to aerogels. *Journal of Material Research*, **10**, 2114–2119.

Quintanilla, J., Reidy, R.F., Gorman, B.P., & Mueller, D.W. 2003. Gaussian random field models of aerogels. *Journal of Applied Physics*, **93**, 4584–4589.

Raman, V.I., & Palmese, G.R. 2005. Nanoporous thermosetting polymers. *Langmuir*, **21**, 1539–1546.

Richards, E.G. 1980. *An Introduction to the Physical Properties of Large Molecules in Solution*. New York: Cambridge University Press.

Rigacci, A., Einarsrud, M.-A., Nilsen, E., Pirard, R., Erhburger-Dolle, F., & Chevalier, B. 2004. Improvement of the silica aerogel strengthening process for scaling up the monolithic tile production. *Journal of Non-Crystalline Solids*, **350**, 196–201.

Roberts, A.P., & Garboczi, E.J. 2000. Elastic properties of model porous ceramics. *Journal of the American Ceramic Society*, **83**, 3041–3048.

Rouquerol, J., Avnir, D., Fairbridge, C.W., Everett, D.H., Haynes, J.H., Pernicone, N., Ramsay, J.D.F., Sing, K.S.W, & Unger, K.K. 1994. Recommendations for the characterization of porous solid. *Pure and Applied Chemistry*, **66**, 1739–1758.

Russ, J.C. 2002. *The Image Processing Handbook*. 4th edn. Boca Raton: CRC Press.

Russ, J.C., & Dehoff, R.T. 1999. *Practical Stereology*. 2nd edn. New York: Plenum Press.

Sacco, L., Lambert, S., Pirard, J.-P., & Noels, A. 2004. Synthesis of pyrazolypyridine derivatives bearing a tethered alkoxysilyl group. *Synthesis*, **5**, 663–665.

Sacco, L., Lambert, S., Pirard, J.-P., & Noels, A. 2005. Olefin cyclopropanation and insertion into OH bonds mediated by copper(I) and palladium(II) covalently anchored to silica xerogels. *Journal of Catalysis*, **232**, 51–59.

Schaefer, D.W., & Keefer, K.D. 1984. Fractal geometry of silica condensation polymers. *Physical Review Letters*, **53**, 1383–1386.

Schaefer, D.W., Bunker, B.C., & Wilcoxon, J.P. 1989. Fractals and phase separation. *Proceedings of the Royal Society London A*, **423**, 35–53.

Schaefer, D.W., Pekala, R.W., & Beaucage, G. 1995. Origin of porosity in resorcinol-formaldehyde aerogels. *Journal of Non-Crystalline Solids*, **186**, 159–167.

Schaefer, D.W., Beaucage, G., Loy, D.A., Shea, K.J., & Lin, J.S. 2004. Structure of arylene-bridged polysilsesquioxane xerogels and aerogels. *Chemistry of Materials*, **16**, 1402–1410.

Scherer, G.W. 1992. Bending of gel beams: method for characterizing elastic properties and permeability. *Journal of Non-Crystalline Solids*, **142**, 18–35.

Scherer, G.W. 1994a. Hydraulic radius and mesh size of gels. *Journal of Sol-Gel Science and Technology*, **1**, 285–291.

Scherer, G.W. 1994b. Relaxation of a viscoelastic gel bar: I. theory. *Journal of Sol-Gel Science and Technology*, **1**, 169–175.

Scherer, G.W. 1994c. Relaxation of a viscoelastic gel bar: II. Silica Gel. *Journal of Sol-Gel Science and Technology*, **2**, 199–204.

Scherer, G.W. 1995. Viscosity and permeability of silica gels. *Faraday Discussions*, **101**, 225–234.

Scherer, G.W. 1996. Influence of viscoelasticity and permeability on the stress response of silica gel. *Langmuir*, **12**, 1109–1116.

Scherer, G.W. 1997. Effect of drying on properties of silica gel. *Journal of Non-Crystalline Solids*, **215**, 155–168.

Scherer, G.W., Smith, D.M, Qiu, X., & Anderson, J.M. 1995. Compression of aerogels. *Journal of Non-Crystalline Solids*, **186**, 316–320.

Scherer, G.W., Alviso, C., Pekala, R., & Gross, J. 1996. Permeability and structure of resorcinol-formaldehyde gels. *Materials Research Society Symposium Proceedings*, **431**, 497–503.

Scherer, G.W., Smith, D.M., & Stein, S. 1997. Deformation of aerogels during characterization. *Journal of Non-Crystalline Solids*, **186**, 309–315.

Schmidt, M., & Schwertfeger, F. 1998. Application for silica aerogel products. *Journal of Non-Crystalline Solids*, **225**, 364–368.

Schmidt, P.W. 1991. Small-angle scattering studies of disordered, porous and fractal systems. *Journal of Applied Crystallography*, **24**, 414–435.

Schmidt, P.W. 1995. Some Fundamental Concepts and Techniques Useful in Small-Angle Scattering Studies of Disordered Solids. *Page 1 of:* Brumberger, H. (ed), *Modern Aspects of Small Angle Scattering*. Dordrecht: Kluwer Academic Publishers.

Sefcik, J., & McCormick, A. V. 1997. Kinetic and thermodynamic issues in the early stages of sol-gel processes using silicon alkoxides. *Catalysis Today*, **35**, 205–223.

Serra, J. 1982. *Image Analysis and Mathematical Morphology*. Vol. 1. London: Academic Press.

Siggia, E.D. 1979. Late stages of spinodal decomposition in binary mixtures. *Physical Review A*, **20**, 595–605.

Siouffi, A.-M. 2003. Silica gel-based monoliths prepared by the sol-gel method: facts and figures. *Journal of Chromatography A*, **1000**, 801–818.

Smith, D.M., Scherer, G.W., & Anderson, J.M. 1995. Shrinkage during drying of silica gel. *Journal of Non-Crystalline Solids*, **188**, 191–206.

Soille, P. 1999. *Morphological Image Analysis, Principles and Application*. Berlin: Springer.

Stanley, H.E. 1971. *Introduction to Phase Transitions and Critical Phenomena.* Clarendon Press.

Stöber, W., Fink, A., & Bohm, E. 1962. Controlled growth of monodisperse silica spheres in the micron size range. *Journal of Colloid and Interface Science*, **26**, 62–69.

Tanaka, H. 1996. Universality of viscoelastic phase separation in dynamically asymmetric fluid mixtures. *Physical Review Letters*, **76**, 787–790.

Tanaka, H. 2000. Viscoelastic phase separation. *Journal of Physics: Condensed Matter*, **12**, 207–264.

Tanaka, T. 1981. Gels. *Scientific American*, January, 124–138.

Tanaka, T., Swislow, G., & Ohmine, I. 1979. Phase separation and gelation in gelatin gels. *Physical Review Letters*, **42**, 1556–1559.

Toebes, M.L., Dillen, J.A. Van, & deJong, K.P. 2001. Synthesis of supported palladium catalysts. *Journal of Molecular Catalysis A: Chemical*, **173**, 75–98.

Ulibarri, T., Beaucage, G., Schaefer, D., Olivier, B.J., & Assink, R.A. 1992. Molecular weight dependence of domain structure in silica-siloxane molecular composites. *Materials Research Society Symposium Proceedings*, **274**, 85–90.

VanBlaaderen, A., & Vrij, A. 1993. Synthesis and Characterization of monodisperse colloidal organo-silica spheres. *Journal of Colloid and Interface Science*, **156**, 1–18.

VandenPoel, G., Goossens, S., Goderis, B., & Groeninckx, G. 2005. Reaction induced phase separation in semicrystalline thermoplastic/epoxy resin blends. *Polymer*, **46**, 10758–10771.

Viscek, T. 1992. *Fractal Growth Phenomena.* 2nd edn. Singapore: World Scientific.

Vollet, D.R., Donatti, D.A., & Ibanez-Ruiz, A. 2001. A SAXS study of kinetics of aggregation of TEOS-derived sonogels at different temperatures. *Journal of Non-Crystalline Solids*, **288**, 81–87.

Vonk, C.G. 1973. Investigation of non-ideal two-phase polymer structures by small-angle X-ray scattering. *Journal of Applied Crystallography*, **6**, 81–86.

Weyland, M., & Midgley, P.A. 2004. Electron tomography. *Materials Today*, **7**(december), 32–40.

Yang, H., Zhang, H., Moldenaers, P., & Mewis, J. 1998. Rheo-optical investigation of immiscible polymer blends. *Polymer*, **39**, 5731–5737.

Ziese, U., deJong, K.P., & Koster, A.J. 2004. Electron tomography: a tool for 3D structural probing of heterogeneous catalysts at the nanometer scale. *Applied Catalysis A*, **260**, 71–74.